

https://doi.org/10.1093/petrology/egad055 Advance access publication date 1 August 2023 Original Manuscript

## Reappraising Crystallization Kinetics with Overgrowth Chronometry: an in Situ Study of Olivine Growth Velocities

Benoît Welsch 1,\*, François Faure 2 and Emily C. First 11

- <sup>1</sup>Geology Department, Macalester College, 1600 Grand Avenue, Saint Paul, Minnesota 55105-1899, USA.
- <sup>2</sup>CNRS, CRPG, UMR 7358, Université de Lorraine, 15 rue Notre Dame des Pauvres Vandoeuvre-Lès-Nancy, F-54501, France.

#### **Abstract**

We investigated the early stages of olivine crystal growth via in situ seeded experiments in a single plagioclase-hosted melt inclusion, using a heating stage microscope. Each experiment was subjected to a cooling ramp of  $7800^{\circ}\text{C}$ /h followed by an isothermal dwell at 19°C, 38°C, 57°C, 77°C, 96°C or 129°C of undercooling. The seeds (6–16  $\mu\text{m}$  in diameter Ø) grew into large crystals (Ø 80–169  $\mu\text{m}$ ) in 3 to 30 min through the symmetrical development of tabular, skeletal, and dendritic overgrowths as the undercooling of the system increased. Time-resolved image processing and incremental measurements of the overgrowth thicknesses indicate up to three stages of crystal growth: an acceleration stage, a linear (constant growth rate) stage, and a deceleration stage. At the isotherm, the growth velocities reach a stable maximum that in all experiments corresponds to the period of linear growth. The highest linear values are measured at the {101} interfaces, from 2.1 × 10<sup>-8</sup> m/s at 19°C of undercooling to 4.8 × 10<sup>-7</sup> m/s at 129°C of undercooling. Crystal growth is slower at other interfaces, in the ranges 1.9–7.6 × 10<sup>-8</sup> m/s and 4.5 × 10<sup>-9</sup> – 7.6 × 10<sup>-8</sup> m/s for the {100} and {001} forms, respectively. Growth in the < 010 > dimension appears limited to less than 2.4 × 10<sup>-8</sup> m/s at 129°C of undercooling. We constrain the uncertainty on these growth velocities, which includes the environmental conditions ( $\pm$  8.6°C on the nominal undercooling) and the measurements of crystal lengths (underestimated by <16% at most fast interfaces).

A systematic and comprehensive review of 19 pre-existing datasets indicates that our linear growth velocities are faster than most growth rates determined at comparable undercoolings. Growth rates determined as half crystal lengths divided by total time are intrinsically low estimates of the true maximum, linear growth velocities, because the total time includes periods of slower or nongrowth, and measured crystal dimensions are subject to projection foreshortening or truncation. These errors can lead to values that are several times to several orders of magnitude lower than the true maximum growth rates. This study completes and refines previously published data on the crystallization kinetics of olivine, highlighting the sensitivity of growth rates to specific environmental conditions and measurement methods. We emphasize the importance of symmetrical growth and true maximum growth velocities for interpreting olivine growth histories.

Key words: Growth rate; kinetics; linear growth; melt inclusion; symmetrical growth

#### INTRODUCTION

The rates at which minerals crystallize are key parameters in the construction of their crystal habit (Sunagawa, 1981) and the capture of elements of various affinities from the melt (Albarède & Bottinga, 1972). Growth rates may however show different behaviors: they can be constant over time (Kirkpatrick, 1975), increase or decrease as a function of the supersaturation and the chemical composition of the melt (Kirkpatrick et al., 1979), or fluctuate with other parameters such as grain size (Eberl et al., 2002) or population density (Hersum & Marsh, 2006). In practice, growth rates calculated as the advance speed of a crystal interface (standardized here in SI units [m/s]) can be determined from virtually any crystallization event as long as information on the crystal dimensions and the duration of crystal growth is made available. But because these two parameters can be difficult to constrain, the apparent growth rates reported can deviate substantially from the true growth rates (Sato et al., 1981). One additional problem for the determination of growth rates is the fact that the textural evolution of crystals is inherently complex: crystals show different prominent faces both as a function of their environment and their crystallization history (Sunagawa, 1957, 1981). Growth rates may hence vary drastically from one study to another, depending on the conditions of crystallization and the analytical methods adopted.

Those aspects are fundamental for a major rock-forming mineral such as olivine since growth rates are instrumental to reverse grain sizes into crystallization durations and timescales of magma cooling in terrestrial and extraterrestrial systems (e.g. Mangan, 1990; Usui et al., 2008; Vinet & Higgins, 2010, 2011; Di Muro et al., 2014; Bouvet de Maisonneuve et al., 2016). Today's models of olivine crystal growth use simple crystal geometries and single-value, crystal size-based growth rates partly because the textural and kinetical evolution of olivine growth forms has been historically approached indirectly through the examination of solid materials, either natural or synthetic, and only a few studies have monitored the crystal growth of

<sup>\*</sup>Corresponding author: bwelsch@macalester.edu

olivine directly with live, in situ techniques (Jambon et al., 1992; Schiano et al., 2006; Ni et al., 2014). To that end, we revisited the experimental set up of Clocchiatti & Massare (1985) using plagioclase-hosted melt inclusions to continuously record the incipient crystallization of olivine at various undercoolings, approach precision measurements of interface-specific growth rates, and characterize the modalities of its crystal growth from a basaltic melt. These methods benefit from a fundamental body of work on the crystallization dynamics of silicate melts (Clocchiatti, 1977a, 1977b; Clocchiatti et al., 1978), combining observational techniques on mineral hosted-melt inclusions (Sorby, 1858; Roedder, 1965, 1979, 1984) and developments in heating stage microscopy (Yermakov, 1950; Heyart, 1955; Barrabé & Deicha, 1956, 1957; Barrabé et al., 1957, 1959; Schmidt, 1959; Dolgov & Bazarov, 1965; Sobolev et al., 1980; Zapunnyy et al., 1988). One advantage of this technique is the ability to track directly the textural and temporal evolution of a single crystal under controlled conditions rather than using indirect markers (such as crystal chemical zoning, or solute loss from the fluid) or extrapolating variations in grain size of an entire population from one set of samples to another through post-mortem analysis. Our results allow us to identify and articulate several issues regarding the quantification and qualification of crystallization kinetics, reinterpret previous datasets, and address the meaning of growth rates in general, that is, how a crystal length relates to the time spent between the liquidus and the solidus.

#### **SAMPLE**

Our sample is a doubly polished 1.10  $\times$  1.21  $\times$  0.15 mm wafer from a 10  $\times$  21  $\times$  8 mm plagioclase macrocryst collected in the hyaloclastites of the 1978 Ardoukoba eruption at lake Assal, Djibouti (Allard, 1980; Bizouard et al., 1980; Weinbruch et al., 2003). These plagioclase crystals have been shown to contain abundant melt inclusions of various sizes (Ø 1–300  $\mu$ m). The melt inclusions are entirely glassy with an occasional shrinkage bubble and no daughter minerals, arguably a result of their quench in the hyaloclastite (Clocchiatti et al., 1978; Bizouard et al., 1980; Clocchiatti & Massare, 1985). These melt inclusions have a relatively homogeneous tholeiitic composition of  $49.3 \pm 1.7$  wt%  $SiO_2$ ,  $13.5 \pm 1.0$  wt%  $Al_2O_3$ ,  $8.2 \pm 1.2$  wt% MgO  $10.4 \pm 1.5$  wt% FeO<sub>t</sub>,  $12.4 \pm 1.6$  wt% CaO<sub>t</sub>  $2.5 \pm 0.3$  wt% Na<sub>2</sub>O<sub>t</sub>  $0.3 \pm 0.3$  wt%  $K_2O$ ,  $1.4 \pm 1.0$  wt%  $TiO_2$  (10 analyses in Clocchiatti & Massare, 1985; Jambon et al., 1992) with 0.06 wt% P<sub>2</sub>O<sub>5</sub>, 0.01 wt% Cl and 0.13 wt% S (Métrich & Clocchiatti, 1996),  $0.54\pm0.01$  wt%  $H_2O$ ,  $749\pm21$  ppm  $CO_2$ , and  $358\pm5$  ppm F (Appendix A5, Table A). The host plagioclase has a chemical composition of An<sub>82-86</sub>, and the other minerals that the melt can crystallize are olivine (Fo<sub>68-84</sub>), clinopyroxene (Wo<sub>36-45</sub> En<sub>41-46</sub> Fs<sub>09-22</sub>), and titanomagnetite (Usp<sub>37-43</sub>; Clocchiatti & Massare, 1985). The oxygen fugacity of the Ardoukoba lavas has been determined at  $10^{-9.15} - 10^{-10.15}$  atm (Allard et al., 1979), which corresponds to the fayalite-magnetite-quartz buffer or up to two log units lower (FMQ to FMQ-2) at standard basalt temperatures (Appendix A5).

#### **EXPERIMENTAL METHODS**

Crystallization experiments were performed in August 2018 with a Linkam TS1500 heating stage at Université de Lorraine - CRPG (Centre de Recherches Pétrograhiques et Géochimiques, France). Temperatures were determined via a type S thermocouple connected to a TMS94 monitor, with a manufacturer's accuracy

of ±1°C, and cross-calibrated against the melting points of Ag (961.8°C) and Au (1064°C). The uncertainty on the temperature was measured at  $\pm 2.5$  °C in the horizontal plane (gradient  $T_h \sim$ 2.5°C/mm) and at  $\pm 6.5$ °C in the vertical axis (gradient  $T_{\nu}$  ~ 84°C/mm), for a total temperature uncertainty at ±7°C using root sum squares. The melt inclusion selected and used as a micro-reactor for the experiments is referred as PC32, with (x, y, z) dimensions at 105  $\times$  203  $\times$  64  $\mu$ m. This melt inclusion was maintained at high temperatures (900°C -1200°C) for 2 days prior to this set of experiments, so the hydrogen dissolved in the fluid was lost to the outside via diffusion through the host crystal, and the silicate melt was therefore oxidized above FMQ-2 (Kornprobst et al., 1979; Roedder, 1979; Sobolev et al., 1983; Danyushevsky et al., 2002; Portnyagin et al., 2008; Chen et al., 2011; Gaetani et al., 2012; Bucholz et al., 2013, Appendix A5). The liquidus temperature of olivine was constrained at 1173 ± 5°C through multiple observations of olivine crystallization and resorption at different locations in the melt inclusion, and comparisons with MELTS simulations (Appendix A5, Fig. A; Ghiorso & Sack, 1995; Duan & Zhang, 2006; Gualda et al., 2012; Ghiorso & Gualda, 2015). For each experiment, a single olivine seed, or germ, was prepared in this melt inclusion by heating and partially dissolving olivine grains that formed above the solidus (Clocchiatti & Massare, 1985). We noted that the olivine seeds did not seem to form at the contact with the plagioclase walls or the main volatile bubble but rather at a distance from them in the central portion of the melt inclusion. Crystallographic indexing of individual olivine crystals was performed by close examination of crystal habits (Faure et al., 2003a, 2003b; Welsch et al., 2013; see Fig. 1a). Each seed was ellipsoidal in shape and elongated in the dimension  $L^{\{100\}}$ , the distance between the centers of the two opposite faces (100) and (100) (Fig. 1b; see Table 1 for crystallographic nomenclature and symbols). Each experiment started once the seed attained minimal dimensions in the vicinity of the olivine liquidus, with Feret diameters (i.e. the minimal and maximal caliper dimensions) in the ranges 6-16  $\mu m$  for the long dimension (L<sup>{101}</sup>) and 2–4  $\mu m$  for the small dimension (L<sup>{001}</sup>Table 2). A first Series [A] of six single step cooling experiments was performed at undercoolings  $(-\Delta T)$  of 19°C, 38°C, 57°C, 77°C, 96°C or 129°C ( $\pm$  8.6°C for 1 $\sigma$ , including the uncertainty on the liquidus), and maximum cooling rates of 130°C/min (i.e. 7800°C/h or  $\sim$  2.17°C/s). Each cooling ramp started within 2 s after digital entry of the targeted temperature. Once this temperature was reached (respectively 9, 14, 23, 32, 39, and 60 s later; Table 2), the sample was held at that temperature until the system melt inclusion + olivine approached immobility. A second Series [B] of three experiments were run as replicates at undercoolings of 38°C, 96°C and 129°C with cooling ramp durations of 14, 39 and 55 s, respectively, to explore any possible deviations.

#### ANALYTICAL METHODS

Snapshots of the melt inclusion's inside were captured automatically during the course of the experiments using a MOT-ICAM 3000 camera and the MOTIC Images Advanced 3.2 software at pre-selected time-intervals (1 to 600 s) suited to the magnitude of the growth rates observed. The raw images were obtained at  $1024 \times 768$  px and 240 dpi, and calibrated with a stage micrometer, for standard dimensions at  $\sim$ 344  $\times$  258  $\mu$ m. Measurement accuracy was estimated to be better than 2  $\mu$ m considering trade-offs between an image resolution of  $\sim$ 0.34  $\mu$ m/px and geometrical uncertainties including optical aberrations, blurred and

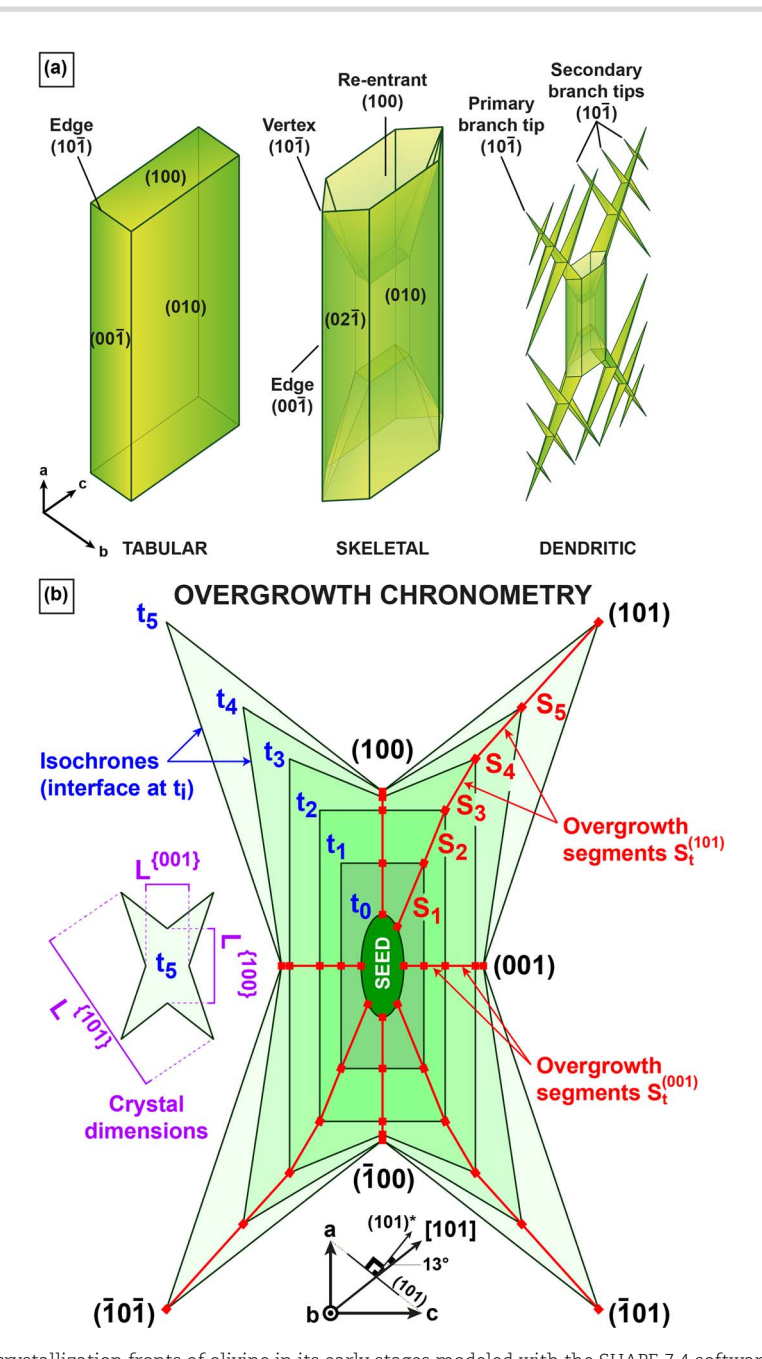


Figure 1. (a) Growth habits and crystallization fronts of olivine in its early stages modeled with the SHAPE 7.4 software (Dowty, 1980, 1987) for pure forsterite in the Phnm space group with cell parameters a: b: c at 4.756: 10.195: 5.981 Å (Donaldson, 1976; Deer et al., 1982; Faure et al., 2003b; Welsch et al., 2013) at an average shape ratio a: b:c of 6.7:1:2.7 based on previous datasets (Faure et al., 2003a; Faure & Schiano, 2004; Welsch et al., 2009; Colin et al., 2012) and our results presented below. The forms {100}, (010}, and {021} were placed at cartesian, central distances of 1, 0.15, 0.4, and 0.27, respectively. An interface can be a flat or re-entrant (i.e. hollow) face, an edge (line junction between two faces), a vertex (point at the intersection of several faces), or a dendrite tip. The tabular shape is made of six flat faces, including two {100}, two {010}, and two {001}. It is important to note that the forms {100} and {001} of tabular crystals are very narrow and difficult to observe properly; it is hence possible that these two forms are in fact edges at the junction of pairs of tiny forms {110} or (021), respectively. The skeletal shape is made of four flat faces (021), two flat faces (010), and two negative (i.e. re-entrant) faces {100}. The growth velocities reported hereafter correspond to those of the edges {001} that are at the intersection of adjacent faces (021). The dendritic shape is made of two flat forms (010) and four primary branches (101). Each secondary branch represents one additional front of crystallization (101). (b) Overgrowth chronometry as developed in this study (secondary branches are not represented). The method is based on the measurement of overgrowth segments  $S_t^{(hkl)}$  (or more accurately,  $S_t^{(hkl)}$ ) between the center points of a specific growing interface (hkl)for every pair of adjacent isochrones  $(t_i \text{ and } t_{i+1})$ , from  $t_0$  (representing the outer rims of the seed) to  $t_{final}$  (representing the outermost interfaces of the final crystal). The related growth velocities were not always associated directly to single crystallographic directions < uvw > considering that directions of growth fluctuate throughout crystal growth (see Analytical Methods and Figs 3 and 5). Furthermore, as a reviewer points out, the normal to an interface, e.g., (101) is not the [101] direction, and we designate the true interfacial normal as (101)\*. In pure forsterite, the (101)\* pole and the [101] direction meet at an angle of  $\sim$ 13° in the (010) plane due to the difference in length of cell dimensions a and c (full body diagonals crossing at 103 / 77°). As a consequence, the instantaneous growth velocity of a dendrite tip is noted as  $G_t^{(101)}$  (for the center of the interface) instead of  $G_t^{(101)}$  (the growth direction) and so on (see Figs 3 and 5; Table 2). Although subject to increased uncertainty, instantaneous growth velocities were calculated for each segment in Supplementary Material A using Equation [2], such that  $G_{[t_3,t_4]}^{(101)} = S_4/(t_4-t_3)$ .

Table 1: List of symbols and their meaning as used in this study

Symbols	Meaning
(hkl)	Crystallographic referent Plane or crystallographic interface (flat or re-entrant face, edge, vertex, or dendrite tip)
(hkl) {hkl}	Family of symmetrically equivalent interfaces (form)
[uvw]	Direction, vector
< uvw >	Family of symmetrically equivalent directions
(hkl)*	Pole (normal) to the plane or interface(hkl)
	<u>Distances</u>
$S_{\left[t_{i},t_{i+1}\right]}^{(hkl)}$	Overgrowth segment measured along the centerline of an interface (hkl) between two consecutive isochrones $t_i$ and $t_{i+1}$ ; sometimes simplified as $S_t^{(hkl)}$ or $S_t$
L <sub>linear</sub>	Portion of crystal half-length formed during a period of linear growth t <sub>linear</sub>
Lacc	Portion of crystal half-length formed during a period of acceleration $t_{acc}$
$L_{dec}$	Portion of crystal half-length formed during a period of deceleration $t_{ m dec}$
L <sup>(hkl)</sup>	Crystal half-length measured from the seed's rim (or the crystal's center when applicable) to the center of an interface (hkl)
L{hkl}	Full crystal length measured between two opposite interfaces {hkl} (e.g. full body diagonals)
Aprojected	Apparent full crystal length A (= $L^{(100)}$ ) in a 2D-projection
A <sub>true</sub>	Actual crystal length A (= $L^{\{100\}}$ )
	Time periods
t <sub>linear</sub>	Period of linear growth (growth rate is constant)
t <sub>acc</sub>	Period of acceleration (growth rate increases)
t <sub>dec</sub>	Period of deceleration (growth rate decreases)
t <sub>incub</sub>	Period of incubation (growth rate $= 0$ )
t <sub>eq</sub>	Equilibrium period (growth rate $\sim$ 0)
t <sub>total</sub>	Total duration of the crystallization event or experiment subliquidus (includes all periods t)
-(hbl)	<u>Kinetics</u>
$G_{[t_i,t_{i+1}]}^{(hkl)}$	Instantaneous growth velocity at the center of the interface (hkl) over a single segment $S_{[t_i,t_{i+1}]}^{(hkl)}$ ; sometimes simplified as $G_t^{(hkl)}$ or $G_t$
G <sub>mean</sub>	Mean growth rate
G <sub>linear</sub>	Linear (constant) growth rate
G <sub>max</sub>	Maximum growth rate allowed by the melt composition at a given undercooling
Gtrue	Perfect measure of a given growth rate
$G_{acc}$	Growth rate during the period of acceleration
$G_{dec}$	Growth rate during the period of deceleration
G <sub>incub</sub>	Growth rate during the period of incubation (= 0)
Geq	Growth rate during the equilibrium period ( $\sim$ 0)
G <sup>(hkl)</sup>	Growth velocity at the center of the interface (hkl)
$G^{\{hkl\}}$	Growth velocity representative of the form $\{hkl\}$
$\overline{a}_{acc}$	Mean positive acceleration
$\overline{a}_{dec}$	Mean negative acceleration (i.e. deceleration)

An interface refers to any type of crystal outer rim at the contact with the melt at an instant t. Ideally, crystal lengths and growth rates must be framed with spatial (i.e. crystallographic) and temporal referents whenever applicable. For instance, the linear growth rate  $G_{linear}$  of a given interface (hkl) is the linear growth velocity  $G_{linear}^{(hkl)}$  (see specific timeframes of linear growth in Figs 3–5 and Supplementary Material A).

out-of-focus crystal boundaries, and corrective alignments in the image stack. The optical aberrations are estimated to be minor given that vapor bubbles appear as quasi-circles under the microscope (>96% match with the perfect shape). Time accuracy is estimated to be better than 1 s considering time off due to shutter speed and digital image acquisition in between the automated trigger and the photomicrograph file timestamp. The outlines of olivine crystals were digitized at selected time intervals to produce isochrone (i.e. contour) maps of overgrowths at arbitrary time marks for each experiment. Eight to thirteen contours were selected for each crystal as a means of both visualizing and quantifying the textural evolution of olivine. In general, the distances between contours were between 0.3 and 20  $\mu m$  (i.e. at or above the image resolution) for initial time intervals in the range 10-200 s. The seed projection on the horizontal plane was used as a spatial

and crystallographic reference for the overgrowths. Here the plane of observation (i.e. the field of view looking down the microscope and focused on the melt inclusion) is used as the spatial reference framework. It corresponds to the horizontal plane (x, y), which is perpendicular with the vertical axis (z) that can be explored with the micrometric knob as the depth of field.

The crystallographic interfaces of interest are specified in Fig. 1a, and the method of overgrowth chronometry is summarized in Fig. 1b. It can be described as the measurement of crystal growth using time-resolved image processing. From microphotograph time series as given in Fig. 2, we built isochrone maps, measured overgrowth thicknesses and determined linear slopes as exhibited in Figs 3, 4 and 5. The thickness of overgrowths was measured from one isochrone to another, segment by segment, using the center of each interface (hkl), as it appears

Downloaded from https://academic.oup.com/petrology/article/64/8/egad055/7235055 by Macalester College user on 02 October 2023

 Table 2: Main parameters and results of the cooling experiments

	Experiment	$\begin{array}{c} \text{Nominal} \\ \text{Undercooling} \\ (-\Delta T_{\text{N}}) \end{array}$	Temperatures	atures	Duration of the cooling ramp	Period of linear growth (a) t <sub>linear</sub>	Olivine dimension $L^{\{001\}}\times L^{\{101\}}$	imension $\langle L^{\{101\}}  angle$	Crystal habit		Linear velocities (b) G <sub>linear</sub>	slocities near	
	#_	<u>ה</u>	[°C] T <sub>start</sub>	[°C] Tfinal	ဋ	[8]	[ $\mu m$ ] Seed	$[\mu \mathrm{m}]$ Final		[m/s] {101}	[m/s] {100}	[m/s] {001}	[m/s] {010}
Series [A]	[188]	19	1173	1154	6	401–1001	4 × 13	18 × 99	Tabular	$2.1 \times 10^{-8}$	$2.1 \times 10^{-8}$	$4.5 \times 10^{-9}$	1
	[173]	38	1155	1127	14	121-1201	3 × 6	$21 \times 80$	Skeletal	$^{(c)}3.1 \times 10^{-8}$	$^{(c)}1.9 \times 10^{-8}$	$6.5 \times 10^{-9}$	I
	[184]	57	1164	1135	23	40-402	$3 \times 12$	$31 \times 169$	Dendritic	$2.6 \times 10^{-7}$	$7.6 \times 10^{-8}$	$5.4 \times 10^{-8}$	I
	[186]	77	1164	1096	32	40-295	$2 \times 16$	$31 \times 126$	Dendritic	$3.4 \times 10^{-7}$	$5.3 \times 10^{-8}$	$4 \times 10^{-8}$	I
	[169]	96	1159	1077	39	40-240	3 × 9	$23 \times 159$	Dendritic	$4.1 \times 10^{-7}$	$4.5 \times 10^{-8}$	$7.6 \times 10^{-8}$	I
	[180]	129	1169	1044	09	60–210	8 <sub>(p)</sub>	(d)106	Dendritic	$4.8 \times 10^{-7}$	$3.9 \times 10^{-8}$	$3.7 \times 10^{-8}$	1
Series [B]	[171]	38	1164	1135	14	30–421	$4 \times 12$	$22 \times 97$	Skeletal	$^{(f)}5.7 \times 10^{-8}$	$2.3 \times 10^{-8}$	$1.1 \times 10^{-8}$	ı
(replicates)	[182]	96	1159	1077	39	45-285	$4 \times 13$	$14 \times 141$	Dendritic	$3 \times 10^{-7}$	$3.7 \times 10^{-8}$	$1.1 \times 10^{-8}$	ı
	[181]	129	1160	1044	55	60–210	$^{(e)}4 \times 9$	$^{(e)}18 \times 96$	Dendritic	$3 \times 10^{-7}$	I	1	$(g)2.4 \times 10^{-8}$

forms {hk!} from the linear regressions given in Figures 4 and 5 considering dimension foreshortening (Discussion § Effect of the crystal orientation). The olivine dimension L<sup>1001</sup>1 corresponds to the width of seeds and The nominal degree of undercooling ( $-\Delta T_N$ ) is the difference between the liquidus of olivine (determined at 1173 ± 5 °C for PC32 melt inclusion) and the temperature plateau of crystallization ( $T_{\rm final}$ ). Excepted for the replicate experiment [171] where chemical heterogeneities in the melt may have occurred around the seed, only the highest values of growth velocities were reported here for a set of symmetrically equivalent crystals along their c-axis between the opposite faces (001) and (001). The dimension L<sup>(101)</sup> refers to their longest body diagonal extending from one tip (lkl) to its direct opposite [i.e. (101) and (101), or (101) and  $(10\overline{1})$ ]. See also Fig.

a Maximum time intervals used for calculating the linear growth velocities. The periods vary for each extremity depending on whether they reached the deceleration stage or whether they came into contact with an must be larger for interfaces experiencing slow and discontinuous growth (such as 1001) and 1100) at high undercoolings) given that only a limited number of data points can be collected over a smaller thickness of overgrowths obstacle (here they correspond to the thickest overgrowths formed through linear growth; see Supplementary Material A). Note that the true periods of linear growth are longer. The uncertainty on Glinear  $\sim 5 \, \mu \mathrm{m}$ 

bLower bound values for the measured growth velocities. The upper bound can be estimated at +50% or less of the measured value to account for a potential dimension foreshortening at a misalignment of 60° or less with the projection plane. The misalignment with the plane (010) is likely to be inferior to 30° for the crystals in the experiments [188], [183], [169], [183], and [171].

"The plane (010) of this crystal is misaligned at 39° with the projection plane; dimension foreshortening and hence growth velocities at the {101} and {100} interfaces can be corrected with a +19% increase for a shape ratio a: b: c at 1:0.1:0.5 (Fig. 1; Discussion § Effect of the crystal orientation).

<sup>d</sup>The crystal dimensions in the experiment [180] at 129°C of undercooling are given as L<sup>[101]</sup> only.

The crystal dimensions in the replicate experiment [181] at 129°C of undercooling are given as  $L^{(1010)} \times L^{(101)}$ .

m/s. <sup>f</sup>This value corresponds to the growth of the extremity [100] growing near the center; the extremity [100] growing towards the plagioclase wall appear faster at 8.3 × 10<sup>-8</sup> <sup>8</sup>This value corresponds to the period of acceleration because growth in the dimension < 010 > was only significant during the cooling ramp.

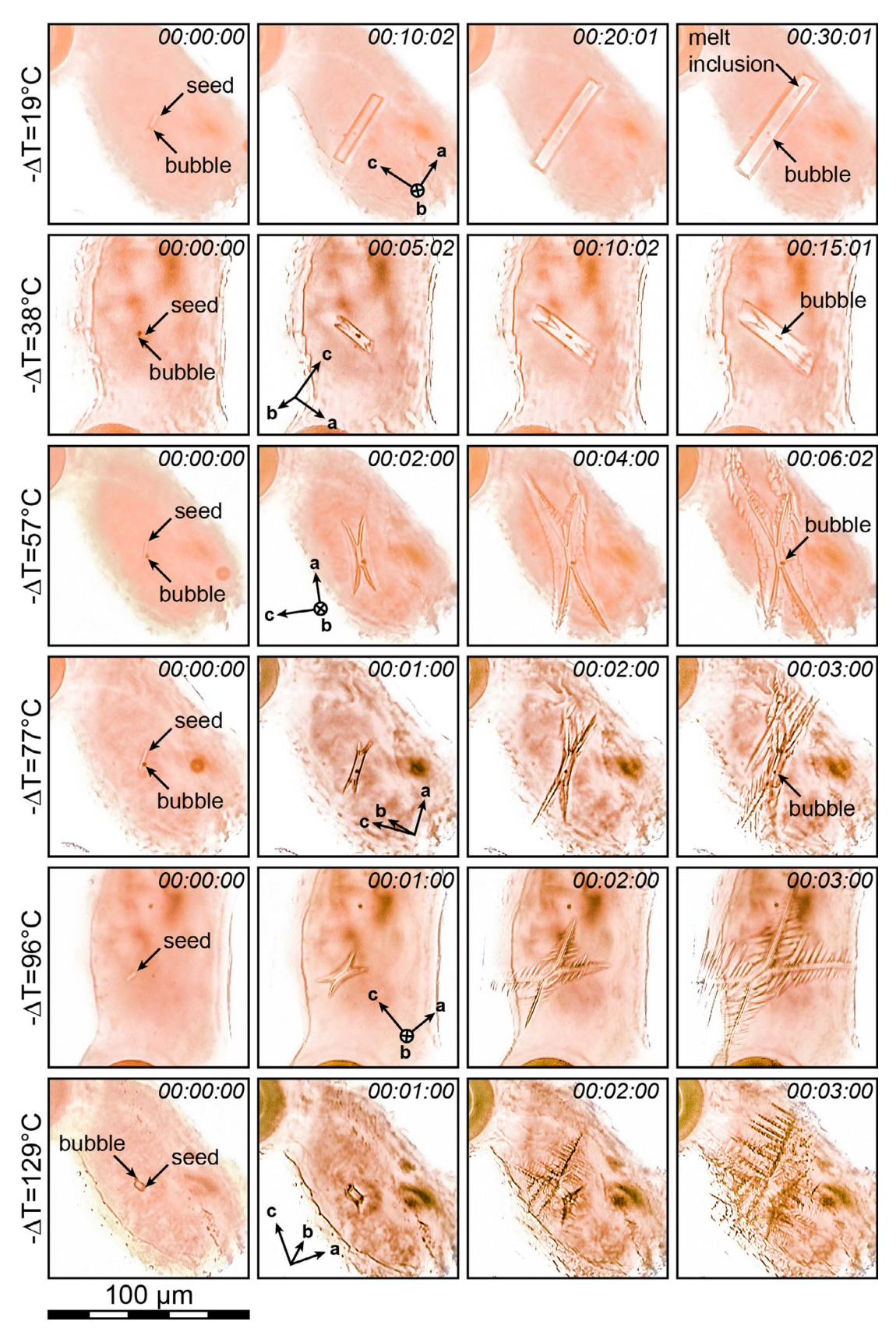


**Figure 2.** Time series of olivine crystal growth at  $-\Delta T = 19^{\circ}$ C, 38°C, 57°C, 77°C, 96°C, and 129°C inside PC32 melt inclusion with the Series [A] experiments. Each frame is 100  $\mu$ m wide. Time stamps are given as hour:minute:second, with 00:00:00 corresponding to the onset of the cooling ramp at T<sub>start</sub> and the contour of the seeds at t<sub>0</sub> (Table 2). Dark areas are other melt inclusions located below or above PC32 and seen out of focus through the transparency of the plagioclase host. Note that the plagioclase walls are overexposed to the light, and the actual interface with the melt on the horizontal plane is located beyond the contrast line. Crystallographic axes are given as first approximations.

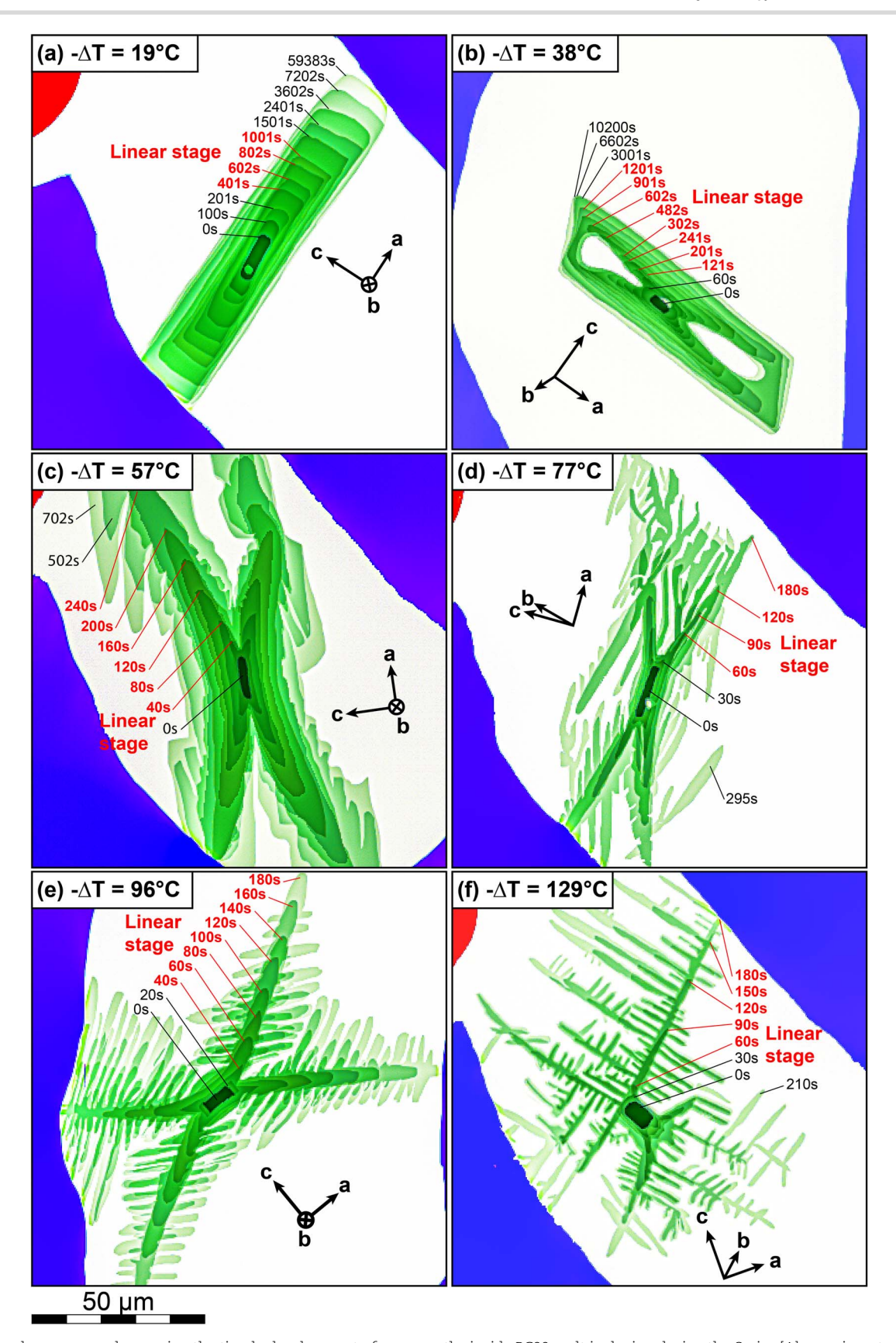


Figure 3. Isochrone maps showcasing the timely development of overgrowths inside PC32 melt inclusion during the Series [A] experiments. Each frame is ~120  $\mu$ m wide. Olivine in green (layered crystal shapes), basaltic melt in white (central background), vapor bubble in red (top left corner when visible), and host plagioclase in blue (corners/edges of images). Only the initial, pre-cooling contours of the vapor bubble and the plagioclase walls are represented here for clarity. Each isochrone corresponds to a growth step on the crystallization clock, with the elapsed time since the onset of the cooling ramp noted on the contour. The seeds correspond to the first contours in darkest green at t = 0 s, although their positions were corrected here for initial motion in the melt upon the first seconds of cooling. The gradual, lighter shades of green with later time marks show the progression of overgrowths. Crystallographic axes are given as first approximations.

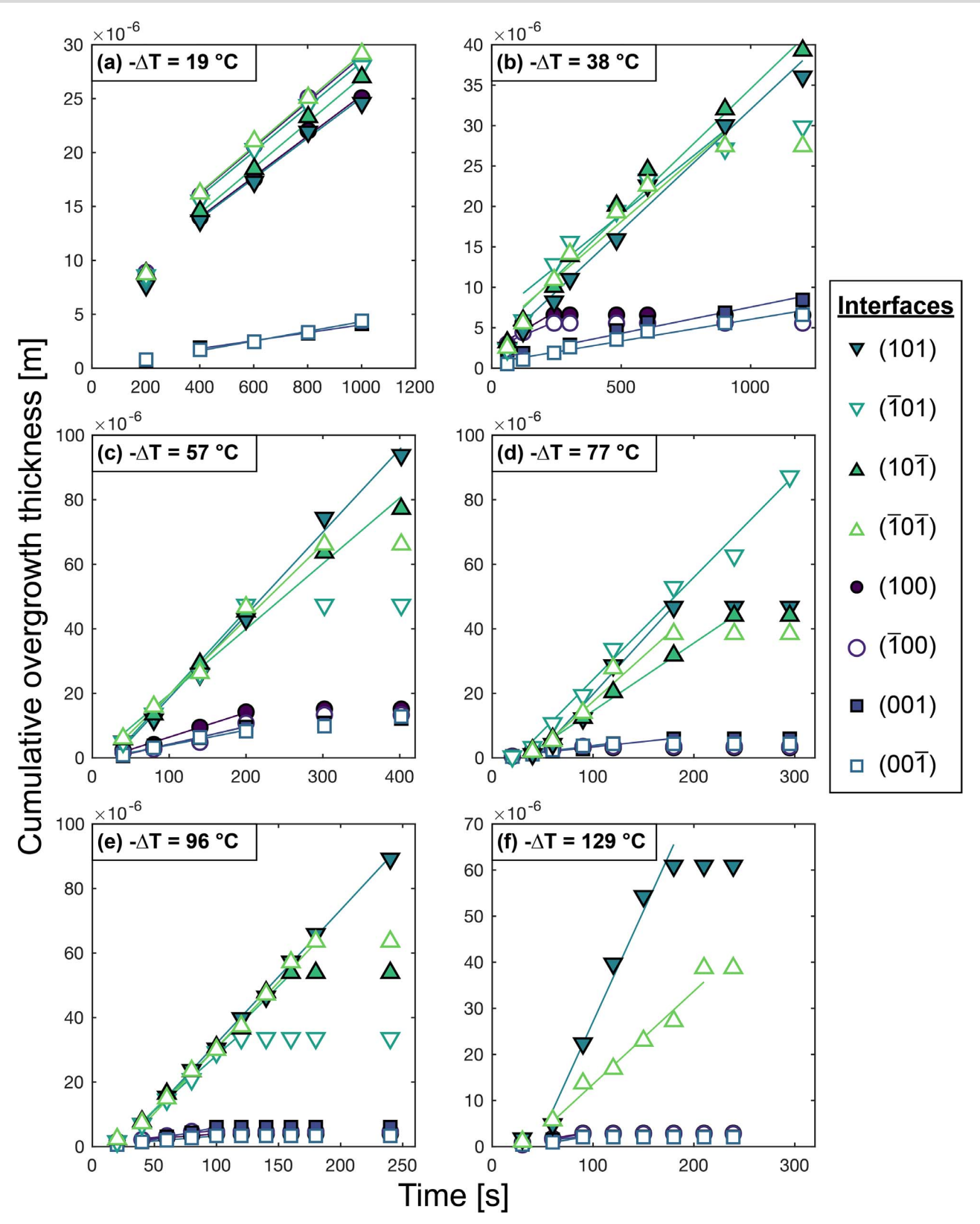


Figure 4. Cumulative thicknesses of olivine overgrowths measured at individual interfaces {hkl} versus elapsed time for the Series [A] experiments (i.e.  $\sum_{i}^{n} S_{t_{i}}^{(hk)}$  versus  $\sum_{i}^{n} t_{i}$ ). Periods of linear growth are identified with least squares fitting; they occur in between periods of more limited increase in the thickness at smaller slopes. Deviations in the slopes (which represent the linear growth velocities, Equation [1]) between symmetrically equivalent forms may be attributed to misalignment of the growth directions with the projection plane (see for instance (f) the crystal formed at 129°C of undercooling). The measurements for calculating the linear regressions are given in Supplementary Material A and the highest values of linear growth velocities (i.e. the slopes) are given in Table 2, with  $R^2 = 0.9-1$ . Determination of oliving growth velocities using least squares fitting is inappropriate at the beginning and at the end of the experiments, when the growth kinetics are unstable. For instance, the crystal in (a) has transiently high velocity (even higher than Glinear) due to growth in a heterogeneous melt at the onset of the experiment [188] at 19°C of undercooling (see Discussion § Acceleration stage). Uncertainty due to image resolution ( $\sim$ 0.3  $\mu$ m / px) is smaller than the symbol size, for all plots.

on the projection plane as a flat or re-entrant (i.e. hollow) face, an edge, a vertex, or a primary dendrite tip (Fig. 1a and b). These overgrowth segments are noted  $S_t^{(hkl)}$ , or more accurately  $S_{[t_i,t_{i+1}]}^{(hkl)}$ , with  $[t_i, t_{i+1}]$  the time interval from the isochrone  $t_i$  to the next  $t_{i+1}$  for a duration  $t_s = t_{i+1} - t_i$ . For each grown olivine crystal, we measured a sequence of overgrowth segments  $S_t^{(hkl)}$  at each observable interface: for a single crystal, this includes up to four sequences at the {101} interfaces, two at the {100}, two at the {001}, and two at the {010}. We then used those segments to calculate cumulative overgrowth thicknesses  $\sum S_t^{(hkl)}$  and identify different lengths pertinent to crystal development and crystallization kinetics. The quantitative data is given in Supplementary Material A, plotted in Figs 4 and 5, and summarized in Table 2. Because these segments do not always align perfectly along a straight direction of growth and may instead curve, the growth velocities refer to the leading front of crystallization (i.e. the center of each physical interface (hkl)) rather than mathematically resolving all segments into a unique, strict crystallographic direction [uvw] for each interface that would not reflect the physical growth of the crystal (Fig. 1b). Consecutive segments hence represent a temporal decomposition of the direction of growth for each interface (hkl). In addition to these segments, the full crystal dimensions L<sup>{hkl}</sup> were determined as the distances between the centers of two opposite {hkl} rims, as illustrated in Fig. 1b with the isochrone at  $t_5$  (see measurements in Table 2). We also refer to crystal half-lengths L(hkl) as the distances from either the rim of the seed (or the center of the crystal when applicable) to the rim of a given (hkl) interface.

Growth rates were determined as linear velocities  $G_{linear}^{(hkl)}$ using sequences of segments S<sub>t</sub><sup>(hkl)</sup> during which growth appears constant at the interface (see Equation [1] below), and as instantaneous velocities  $G_t^{(hkl)}$ using separate segments  $S_t^{(hkl)}$  (Equation [2]). Growth velocity refers to a growth rate that is specific to a single crystallographic interface (hkl) that progresses outwardly. Measuring 'growth velocity' is preferred here as a vector at a specific interface rather than an absolute speed because it eliminates the uncertainty on the number of faces considered and their crystallographic identity. A 'growth rate' may have a broader meaning for being either dimension- or mass-based, and it is often associated with assumptions about or simplifications of the crystal geometry, interfaces, and directions of growth. Linear growth implies that the advance speed of a given interface is nearconstant over time, as evidenced with a data plot in crystal halflength ( $L^{(hkl)}$  where  $L^{(hkl)} = \sum S_t^{(hkl)}$ ) versus time (t) space showing a positive linear correlation (Figs 4 and 5). The linear growth velocity  $G_{linear}$  is the slope of the line describing this correlation, calculated from the arithmetic means  $\bar{t}$  and  $\bar{L}$  of the n measurements of overgrowths L for a single interface (hkl) during a period t:

$$G_{linear} = \frac{\sum_{i=1}^{n} \ \left(t_{i} - \overline{t}\right) \left(L_{i} - \overline{L}\right)}{\sum_{i=1}^{n} \left(t_{i} - \overline{t}\right)^{2}} \text{ where } \overline{t} = \frac{\sum_{i=1}^{n} t_{i}}{n} \text{ and } \overline{L} = \frac{\sum_{i=1}^{n} L_{i}}{n}$$

$$\tag{1}$$

This method is well suited for time series analysis since the trend line must satisfy the smallest deviations in the ordinate values (i.e. crystal dimensions with the most uncertainty) at accurate abscissa values (i.e. time intervals with practically no uncertainty). This method is however not well suited to approach non-linear kinetics of crystal growth. Our overgrowth chronometry dataset allows the building of isochrone maps that are dense enough to construct the linear regressions, and track both from the graph and the olivine textures when and where significant deviations in the growth rates occur. Face-specific growth rates

were also determined for the shortest time intervals (i.e. between pairs of successive contours in the isochrone maps). These are the instantaneous growth velocities  $G_t$  for a given interface (hkl) over a given time period t such that:

$$G_t^{(hkl)} = \lim_{\Delta t \to 0} \frac{\Delta L^{(hkl)}}{\Delta t} = \frac{dL^{(hkl)}}{dt}$$
 (2)

where  $dL^{(hkl)}$  is the distance of movement forward of the crystal interface (hkl) in the time interval dt (i.e. between two given isochrones, usually successive). In principle, the time interval should be as close to zero as possible, but this parameter is limited by the uncertainty on the measured dimension. For instance, with an uncertainty of 1  $\mu$ m (i.e. approximately 3 px with our image resolution), the smallest time intervals related to the growth rates should be  $\geq 1$  s at  $10^{-6}$  m/s, 10 s at  $10^{-7}$  m/s, 100 s at  $10^{-8}$  m/s, and 1000 s at  $10^{-9} \text{ m/s}$ . Because the time intervals are very short in comparison with the total crystallization time, we can only assume that the increase in overgrowth thickness between two data points  $S_t^{(hkl)}$  is constant. This assumption is necessary to investigate short-termed crystallization fronts and small growth increments, although they are by definition less accurate than linear regressions using more than two data points (i.e. linear velocities  $G_{linear}$  over cumulative overgrowth thickness  $\sum S_t^{(hkl)}$ ).

As detailed in the Discussion, we provide estimations of the error on the determination of crystal dimensions and growth rates. These error estimates are expressed as:

%error = 
$$100 \times \frac{(X_{measured} - X_{true})}{X_{true}}$$
 (3)

with  $X_{measured}$  being the observed value and  $X_{true}$  being the true value. In practice, the true values can be recalculated with the following relationship:

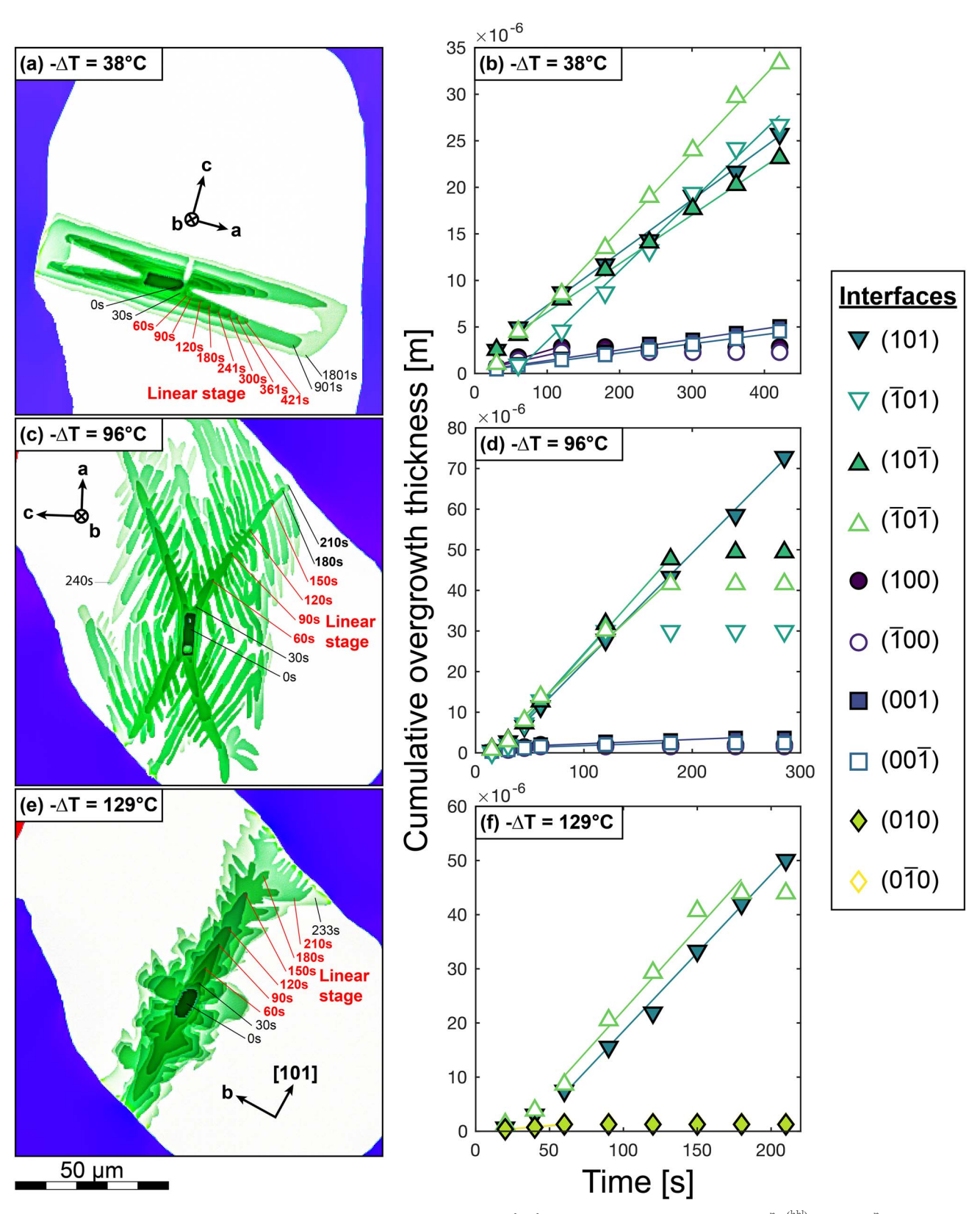
$$X_{true} = 100 \times \left[ \frac{X_{measured}}{\%error + 100} \right]$$
 (4)

#### RESULTS

The cooling experiments allowed observation of four simultaneous and interlinked processes inside the melt inclusion: inward growth of the plagioclase walls, expansion of the gas bubble, reduction of the melt fraction, and development of overgrowths on the olivine seeds (Fig. 2), as reported in Clocchiatti & Massare (1985) and Jambon et al. (1992). No other daughter minerals such as clinopyroxene or FeTi oxides were observed, and no new olivine crystals nucleated from the melt during the experimental runs. The results below refer to Series [A], with the replicates (Series [B]) addressed separately at the end of this Results section. Timeresolved measurements of overgrowth thicknesses onto the seeds are provided in Supplementary Material A. Selected images from the Series [A] of the olivine seeds's crystal growth are provided in Fig. 2, and the corresponding isochrone maps are given in Fig. 3. Measurements are reported in Fig. 4 for the Series [A] and in Fig. 5 for the Series [B] as cumulative thicknesses of overgrowths versus elapsed time. Isochrone maps for the Series [B] are also given in Fig. 5. Growth velocities  $G_{linear}^{(hkl)}$  were determined for the crystallographic interfaces (001), (100), (101) and (010) when applicable, as reported in Table 2.

#### Set period

In all experiments (except the one [A] at 96°C of undercooling), the seed was initially in contact with a single small bubble ( $\emptyset \le 3 \mu m$ ), which remained attached and became trapped and buried under



 $\textbf{Figure 5.} \ \ \text{Isochrone maps and cumulative thicknesses at individual interfaces } \left\{ \textit{hkl} \right\} \ \text{versus elapsed time graphs (i.e. } \sum_{i}^{n} S_{t_{i}}^{(\textit{hkl})} \ \text{versus } \sum_{i}^{n} t_{i}) \ \text{for the three}$ experimental replicates of the Series [B] at 38°C, 96°C and 129°C of undercooling. Note that the crystal morphologies and growth velocities are comparable to those observed in Figures 3 and 4. Discrepancies in crystal geometries and growth velocities may be attributed to variations in crystal orientations with respect to the plane of observation, and to local factors such as the position of the seed inside the melt inclusion. Crystallographic axes are given as first approximations.

the overgrowths (Fig. 2). All the olivine seeds showed very little changes in size and shape during the first instants of cooling and it is only after  $\sim$ 10 s that the overgrowths were noticeable and measurable (with a thickness > 1  $\mu$ m). The seeds were mobile during that short period of time (t < 10 s), then remained in their last position throughout the rest of their crystal growth. The large vapor bubble remained immobile during the entire course of the runs, which is another evidence that there was little to no convection in the melt after the first seconds of cooling.

#### Crystal orientation

Most of the olivine crystals grew exposing their interfaces (h0l) (Figs 2 and 3). The recognizable habits of crystals formed at 19°C, 57°C and 96°C of undercooling suggest that their (010) planes are close to alignment with the plane of observation. The crystal formed at 77°C of undercooling has a similar orientation but is visibly dipping more significantly in the direction  $[00\overline{1}]$ . The olivine crystal formed at 38°C of undercooling is tilted around the c-axis (39° pitch inclination with the horizontal plane; see Discussion § Effect of the crystal orientation) with a second inclination (roll) around the [101] direction. The crystal in the experiment at 129°C of undercooling shows a more complex orientation that allows some observation of growth in the < 010 > dimension that is not visible in the other experiments.

#### Extent of crystallization

Although the crystals started growing during the cooling ramps, most of their growth occurred after they reached the set temperature. At the isotherm, the overgrowths continued to expand until reaching opposite sides of the melt inclusion, usually in the horizontal plane, resulting in single crystals of the size and texture of microlites and microphenocrysts found in natural magmas (Table 2). The crystal formed at 38°C of undercooling grew enough in the vertical dimension that its long < 100 > extremities reached both the front and back walls of the melt inclusion (Figs 2 and 3b). In all runs, the crystals did not change position even after touching the walls of the melt inclusion and growing against them.

#### Textural evolution

The progression of overgrowths is both outlined and timed by the crystal contours in the isochrone maps (Fig. 3). These isochrones are essentially concentric around each seed, with wider spacings in the directions < 100 > or < 101 > than in the directions < 001 > at all undercoolings investigated. The resulting crystals appear elongated in the < 100 > direction at low and moderate undercoolings (19°C and 38°C) and elongated in the < 101 > direction at high undercoolings (57°C, 77°C, 96°C and 129°C). The tilted crystals in the experiments at 38°C and 129°C of undercooling show that their dimension L<sup>{010}</sup> is very small, which is consistent with previous documentation of the flat habit of olivine during its early stages of growth (Donaldson, 1976; Faure et al., 2003a; Faure & Schiano, 2004; Colin et al., 2012). Although the outer rims of the seeds were rounded at the start of the experiments, the first overgrowths were immediately faceted, with the common forms {100}, {010}, and {001} (Fig. 1). The shape of crystals varied from tabular at low undercooling (19°C), to skeletal at moderate undercooling (38°C) and to dendritic at high undercooling (57°C, 77°C, 96°C and 129°C; Fig. 2), in good agreement with the model of Faure et al. (2003a).

#### Tabular habit

The crystal formed at 19°C of undercooling shows the simple shape described in Faure et al. (2003a) with the flat face ( $0\overline{1}0$ )

facing the microscope lens (Figs 1, 2 and 3a). The tabular shape of overgrowths was sustained throughout the entire duration of this experiment (16.5 h), with no embayment (i.e. no re-entrant face), branch, or appearance or disappearance of any of the primary forms {hkl}. One single melt inclusion can be observed on one end of the crystal length (Fig. 2), but its formation was too subtle to be recorded live and in-focus. There is no symmetrical equivalent of this melt inclusion on the other end of the crystal, which marks a difference with the closed hopper morphology, as discussed in the next paragraph.

#### Skeletal habit

The crystal formed at 38°C of undercooling displays a true closed hopper morphology with hollow forms {100} that were sealed simultaneously into symmetrical melt inclusions (Figs 1, 2 and 3b; Faure & Schiano, 2004; Welsch et al., 2009; Colin et al., 2012). The crystal first developed tabular overgrowths {100} and {001}, then the center of the forms {100} ceased growing before the 60 s mark. As crystal growth was sustained at the interfaces (001) and at the vertices {101}, an embayment of melt formed at the center of forms {100} on both ends of the crystal. It is important to note that the forms {010} are still present at that stage of crystal embayment, although these forms are so thin than they appear transparent (only the trace of the rim  $(0\overline{1}0)$  can be observed in the frames of Fig. 3b). Growth in the directions < 1vw > started fading after the 1201 s mark, and a cap formed atop the embayments, by slower growth of {110} and {101} forms, which achieved trapping of the two symmetrical melt inclusions before 3001 s.

#### Dendritic habit

The four seeds brought to high undercoolings (57°C, 77°C, 96°C and 129°C) exhibit overgrowths that match the classic swallowtail morphology consisting of a chain of parallel skeletal units (Figs 1, 2 and 3c-f; Donaldson, 1976; Faure et al., 2003a, 2003b). The overgrowths were tabular in the first 10 s of cooling then transitioned to a skeletal morphology through the arrested growth of the forms (100). The true dendritic habit appeared after 70 s with the development of primary branches {101} and the emergence of secondary branches {101}.

#### Linear growth

All the crystals show some isochrones with evenly spaced time intervals (Fig. 3), indicating periods of constant growth at different forms {hkl}. Accordingly, plots of the measurements in the Fig. 4 show that the cumulative thickness of overgrowths increases linearly with the elapsed time, with correlation coefficients  $R^2 \ge$ 0.9. Excepted for the experiment at 19°C of undercooling (see Fig. 4 and Discussion § Acceleration stage), the value of growth rate for which the crystallization is linear at a given interface also corresponds to the maximum velocity attained by this interface during the isothermal period (Fig. 4, Supplementary Material A). Over the set of experiments, the maximum linear velocity of the interfaces  $G_{linear}^{(hkl)}$  reaches higher values when the undercooling increases (Table 2). The {101} edges, vertices and tips of the primary branches grow from  $2.1 \times 10^{-8}$  m/s at  $19^{\circ}$ C of undercooling to  $4.8 \times 10^{-7}$  m/s at 129°C of undercooling. The velocity of the {001} forms is comparatively slower, from  $4.5 \times 10^{-9}$  m/s at  $19^{\circ}$ C of undercooling to 7.6  $\times$  10<sup>-8</sup> m/s at 96°C of undercooling. The {100} forms have intermediate velocities, from  $2.1 \times 10^{-8}$  m/s at  $19^{\circ}$ C of undercooling to 7.6  $\times$  10<sup>-8</sup> m/s at 57°C of undercooling. The velocities of the {001} and {100} forms are somewhat less accurate, because the increments in overgrowth thickness are small and close to the spatial resolution of the images. The isochrone maps

in Fig. 3 also show that the crystal lengths formed through linear growth increase with the undercooling.

#### Non-linear growth

The data plot of cumulative thickness of overgrowths over elapsed time (Fig. 4) show that crystal growth deviates from linear for two specific time periods of the experiments: at the onset of the experiments when the first overgrowths appear on the seed, and at the end of the experiments when the crystal approaches its maximum size, whether due to decreasing thermodynamic driving force (experiments at 19°C and 38°C of undercooling) or by reaching an obstacle in the melt (either the melt inclusion's walls, or a vapor bubble, experiments at 57°C, 77°C, 96°C and 129°C of undercooling; Figs 2-4). The kinetics of nonlinear growth can be tracked with instantaneous growth velocities  $G_t^{(hkl)}$ , although with higher uncertainty due to fewer data points and measurements of growth increments at the limit of the spatial resolution.

#### Symmetrical growth

The contours in the isochrone maps show that opposite sets of forms {100}, {001}, and {101} have rotational and planar symmetries that continue over a large portion of their crystal growth (Figs 2 and 3). This indicates that the development of symmetrically equivalent faces is simultaneous, and that there is no significant delay between their respective growth. Symmetrical growth is also evidenced with the dual formation of embayments and melt inclusions in skeletal and dendritic crystals, which occur at equidistance from the seed's center (Figs 2 and 3). The data plots of the cumulative thickness versus elapsed time (Fig. 4) demonstrate that symmetrically equivalent forms also have similar linear growth velocities  $G_{linear}^{(hkl)}$  (line slopes in Fig. 4). The isochrone maps also indicate that symmetrical growth occurs whether or not the crystallization kinetics are linear. The crystals with the largest misalignments with the projection plane show the largest dispersion in their growth velocities between symmetrically equivalent interfaces (crystals at 38°C, 77°C, and 129°C of undercooling; Fig. 4). On the other hand, similar growth velocities can be observed between symmetrically equivalent interfaces in crystals with their (010) plane close to alignment with the projection plane (19°C, 57°C, and 96°C of undercooling; Fig. 4).

#### Experimental replicates

In Series [B], three experiments were repeated at undercoolings of 38°C, 96°C, and 129°C, with the difference that the seeds crystallized with a different crystallographic orientation with respect to the projection plane, and in another location of the melt inclusion. In all three replicates, the crystals developed habits that are similar to those observed for their Series [A] counterparts (Fig. 5a, c and e). The skeletal crystal at 38°C of undercooling is also a closed hopper, but it shows a clear asymmetry: it has a long extremity [100] due to free growth in the melt, and a shorter extremity [100] due to encountering a physical impediment after it came into contact with the plagioclase wall. The crystal at 96°C of undercooling is dendritic (swallowtail) and is essentially identical to the one formed during the Series [A] experiment, albeit with slight misalignment of its (010) plane with the projection plane. The crystal at 129°C is also dendritic but has a more compact (needle) shape that contrasts with the branch shape of the crystal formed in the first experiment. This difference is attributed to the crystal orientation, such that the needle shape corresponds to a sideways view of the swallowtail morphology, in a composite plane type (h1l), with limited growth

in the < 010 >dimension, as observed in previous studies (Donaldson, 1976; Faure et al., 2003a, 2003b). The linear velocities  $G_{linear}^{(hkl)}$ are mostly the same order of magnitude as those observed in Series [A] (Figs 4 and 5b, d and f). At 38°C of undercooling, the skeletal vertices {101} show fast velocities when growing towards the plagioclase walls (7.5–8.3  $\times$  10<sup>-8</sup> m/s), and slower velocities when growing towards the center of the melt inclusion (5.2-5.7  $\times$  10<sup>-8</sup> m/s; Table 2). Both these velocities are faster than the ones observed in the Series [A] experiment (in the range 2.6-3.1  $\times$  10<sup>-8</sup> m/s or 2.9–3.7  $\times$  10<sup>-8</sup> m/s after correction for a 10% to 16% negative error; see Discussion § Effect of the crystal orientation). At 96°C of undercooling, the linear velocities of the four dendrite tips {101} are similar (2.5-3  $\times$  10<sup>-7</sup> m/s) and relatively close to those formed in the first experiment (3.4–4.1  $\times$  10<sup>-7</sup> m/s). At 129°C of undercooling, the linear velocities of the dendrite tips {101} are consistent both with each other and with those measured in Series [A]  $(2.9-3 \times 10^{-7} \text{ m/s versus } 2-4.8 \times 10^{-7} \text{ m/s, respectively}).$ Finally, the {010} interfaces, which are not visible in any other runs, are observable at 129°C of undercooling and display one of the lowest linear velocities in the dataset, at  $2.42 \times 10^{-8}$  m/s (Fig. 5).

#### DISCUSSION

#### **Experimental limitations**

The significance of our results is defined not only by the collection and interpretation of data itself, but also by the balance of inherent benefits and limitations of the experimental set up. To that end, aspects intrinsic to cooling, seeding, interactions with other phases, compositional variations and diffusion in the melt, and thermal gradients, are detailed in the Appendix A. Consistent with the studies of Clocchiatti & Massare (1985) and Jambon et al. (1992), our results suggest that this specific experimental set up is reproducible, reversible, and reliable for precision measurements, within certain bounds. The experimental replicates show that crystals experiencing similar cooling conditions have comparable crystal habits and growth velocities inside the same melt inclusion (Figs 2-5; Table 2). Any small discrepancies in growth velocities are attributable to at least two parameters: (1) differences in crystal orientations with respect to the plane of observation, and (2) differences in crystal location within the melt inclusion, which implies variations in the local thermochemical conditions that are difficult to assess more specifically (inherent uncertainty at  $\pm 7$ °C). Abrupt changes in liquidus temperature or internal pressure were minimized across the experiments since the same melt inclusion was used for all runs, and that melt inclusion had already lost most of its hydrogen prior to these experiments (§ Experimental Methods & Appendix A). The fact that olivine overgrowths formed at constant speed over protracted periods of time (Figs 3 - 5) suggests that thermodynamic variations were not significant and/or counterbalanced each other at the timescale of our experiments. Thus, hysteresis was effectively limited over the course of the experiments.

#### Three stages of crystal growth

The experiments show that the growth velocities increase with undercooling, from  $-\Delta T = 19^{\circ}$ C to  $-\Delta T = 129^{\circ}$ C, which is consistent with previous measurements (Jambon et al., 1992) and classic theories of crystal growth (Kirkpatrick, 1975; Sunagawa, 1981). Our overgrowth chronometry (Figs 2-5) identifies three stages of crystallization: a first stage at low but increasing growth velocities, a second stage at maximum and constant growth velocities, and a third stage at declining to null growth velocities (Fig. 6).

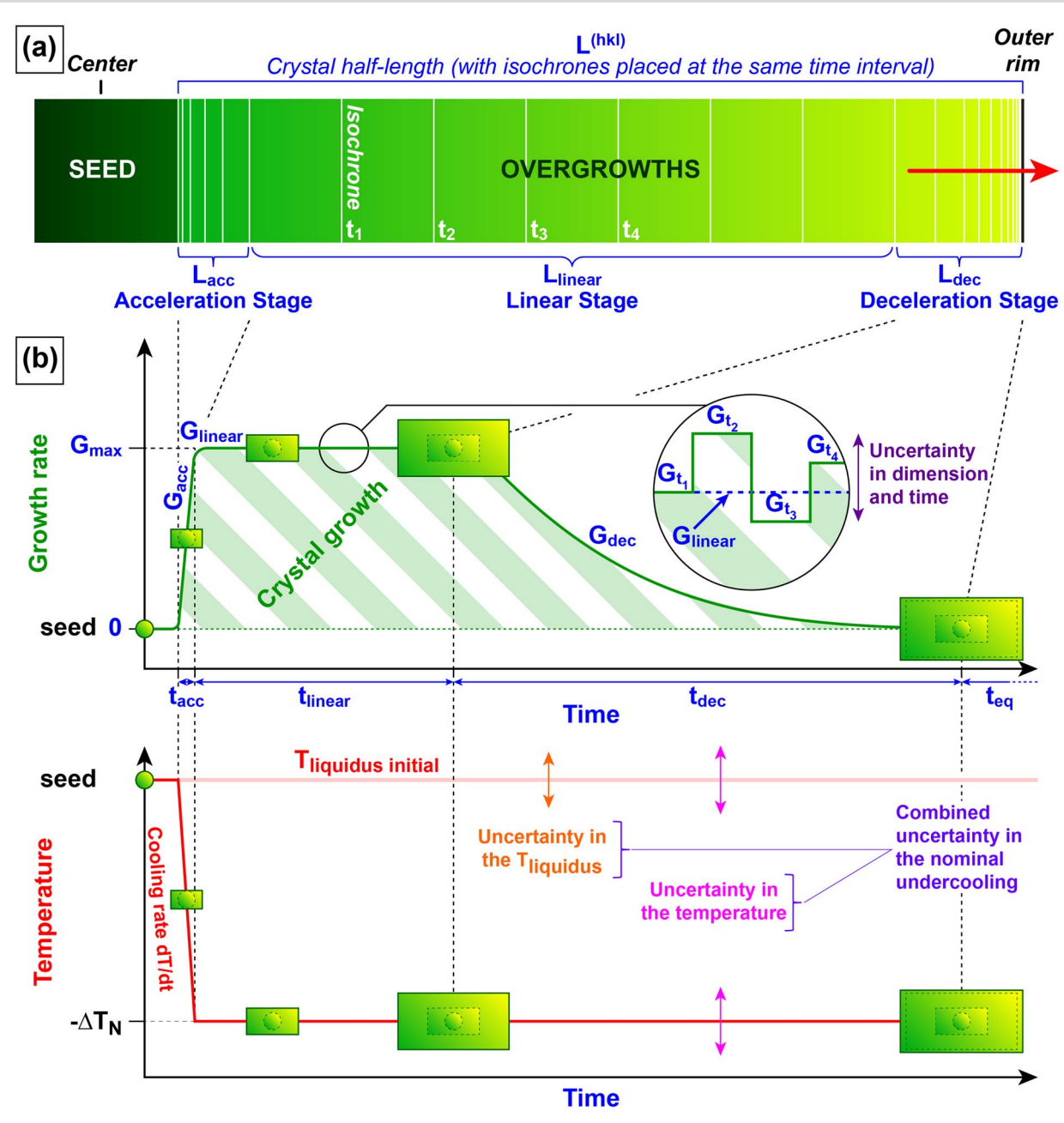


Figure 6. Simplified sketch of the crystallization behavior of olivine. (a) Idealized profile of overgrowth chronometry and stratigraphy for a seed experiencing a single-step cooling performed at fast rates, with isochrones (white lines parallel to the seed surface) placed at a regular time interval on one half-length of the crystal. This shows that a crystal length may consist of different segments formed at different kinetics. (b) Related olivine crystal growth in the growth velocity (hkl) versus time, and the temperature versus time spaces. The entire growth process for a continuously advancing interface (hkl) (such as (101); see Figs 1-5) corresponds to the area shaded with wide hatches (light green and white) that is above null growth rates. Olivine crystallization includes (1) a first stage of acceleration of which the duration and the growth rates are controlled by the cooling rate dT/dt (Gacc increases over the period tacc, observed in the experiments at 38°C, 57°C, 77°C, 96°C and 129°C of undercooling), (2) a stage of linear growth during which the growth rate is steady-state ( $G_{linear}$  constant over the period  $t_{linear}$ , observable in all experiments), (3) a stage of deceleration with a progressive decrease in the growth rate of several orders of magnitude ( $G_{dec}$  decreases over the period  $t_{dec}$ , observed in the experiments at 19°C and 38°C of undercooling), until reaching (4) a state of quasi-immobility marking the final equilibrium with the melt and the end of the crystal growth (Geq = 0 at teq). Note that the linear growth rates show no significant acceleration or deceleration provided that the variations observed between the linear velocities  $G_{linear}^{(hkl)}$  and the instantaneous velocities  $G_{t}^{(hkl)}$  can be attributed to measurement uncertainties that are exacerbated at short time intervals and small overgrowth increments (illustrated here with isochrones  $t_1$ ,  $t_2$ ,  $t_3$  and  $t_4$  as an example). In fact, a plot of the instantaneous growth velocities  $G_{i}^{(hkl)}$  given in the Supplementary Material A will show important dispersion because the errors on the measurements (image resolution and time window) are more pronounced at the smaller scale and the individual level. Note also that the growth velocities  $G_{acc}$  and  $G_{dec}$  are not single values (see Discussion § Effect of a period of slower or non-growth, and Equation [10]).

#### Acceleration stage

For most of our experiments, direct measurements of growth during this first stage run up against the resolution of microscope

imaging. We can, however, turn to abundant indirect evidence to show that overgrowths develop at an accelerating pace, consistent with the fact that the growth velocities increase directly with

the undercooling, from 19°C to 129°C (Table 2). An increase in the growth velocities is also consistent with the fact the final olivine crystals contain habits formed at lower undercoolings and lower growth velocities, as the seeds cross several domains of morphological stability (Fig. 1). The encapsulation of morphologies follows the classic sequence tabular > skeletal > dendritic (Faure et al., 2003a), such that the crystals formed at moderate undercooling (38°C) record the first two shapes (tabular + skeletal), and the crystals formed at high undercoolings (57°C, 77°C, 96°C and 129°C) record all three shapes (tabular + skeletal + dendritic), similar to Matryoshka dolls (Figs 1, 3 and 5). The fact that tabular overgrowths always formed first and the skeletal and dendritic overgrowths never grew directly on the seeds indicates that the change in growth morphology and growth kinetics are both controlled by the undercooling. Additionally, the fact that crystal growth started within seconds of initiating the cooling ramp indicates that the seeds' response to the abrupt thermodynamic variation is immediate, with no significant delay in the development of overgrowths. This suggests that the duration of this acceleration stage is equivalent to the duration of the ramp. The stages of acceleration would hence last 14, 23, 32, 39 and 60 s (Table 2), which is that much time for the system to reach the temperature plateaus at  $-\Delta T = 38^{\circ}$ C, 57°C, 77°C, 96°C, and 129°C, respectively. The only exception appears to be the experiment performed at 19°C of undercooling where the highest growth velocities were observed in the first ~200 s of cooling, prior to linear growth. This is presumably because the seed crystallized near the liquidus and shortly after the germ's partial dissolution, i.e. from a melt enriched in olivine components.

#### Linear stage

During this second stage, the growth velocities reach a stable maximum that is a function of the nominal degree of undercooling (Table 2). This observation is true only for the forms that can grow at the current undercooling. At 19°C, each form {hkl} expands at constant rates, but at 38°C, the forms {100} ceases to grow, and at 57°C and beyond, the shape of the forms {001} and {021} evolves until they stop growing. The {010} forms are observed in only one experiment (Series [B],  $-\Delta T = 129^{\circ}$ C), in which they are the slowest-growing faces (Fig. 5e, f). The {101} interfaces may be the only ones that grow continuously at all undercoolings: their growth velocities increase first as edges and vertices in the tabular and skeletal crystals, then as branches in the dendritic crystals (Figs 1, 3, and 5). Growth velocity plateaus indicate that the conditions of: crystallization at the interface are unperturbed over that period of time. The fact that the highest growth velocities  $G_{max}^{(hkl)}$  attained during each experiment correspond to the linear growth velocities  $G_{linear}^{(h\bar{k}l)}$  (Table 2; Figs 4–5) implies that any other value of growth rate that is observed at the same interface will be necessary lower and related to either the acceleration and/or the deceleration stage.

#### Deceleration stage

The third stage happens when the growth velocities cease to be linear and start fading. The decrease in the growth velocities after the linear stage may be the result of a depletion of the melt in olivine components that was too pronounced to sustain linear growth, as the liquidus and the related undercooling decrease with differentiation, as suggested in Jambon et al. (1992). This is best characterized with the long experimental runs at 19°C and 38°C of undercooling as the crystals were small enough to keep growing after the linear stage over a protracted period of time. From 1001 to 59383 s (16.7 min to 16.5 h) in the experiment at

19°C of undercooling, the instantaneous growth velocities  $G_t^{(hkl)}$ decreased of one to two orders of magnitude (from  $1.3 \times 10^{-8}$ to 8.8  $\times$  10<sup>-11</sup> m/s for the {101} forms, from 1.3  $\times$  10<sup>-8</sup> to 1.0  $\times$  10<sup>-10</sup> m/s for the {100} forms, and from 3.6  $\times$  10<sup>-9</sup> to 2.5  $\times$  $10^{-10}$  m/s for the {001} forms; Supplementary Material A). The final velocities at  $10^{-10} - 10^{-11}$  m/s are consistent with the growth rates determined at very low undercoolings (e.g.  $-\Delta T < 1^{\circ}C$ ; Park & Hanson, 1999; Cabane et al., 2005; Schiano et al., 2006). However, our experiments show that the crystals formed at higher undercoolings reached both sides of the melt inclusion through linear growth (Figs 3 and 5), which indicates that their final size would have exceeded that of the melt inclusion if their crystal growth was entirely free. This suggests that the drop in the growth velocities was not a consequence of a depletion of the melt in olivine components, but rather of the constriction of the crystals in directions of most efficient growth.

#### Implications for growth rate determination

To effectively place this new work within the body of literature on olivine growth rates, we must explore the relationships and limitations between the mean growth rates  $G_{mean}$  estimated by indirect methods and the linear growth rates  $G_{linear}$  measured by direct methods. Below, we conduct a rigorous analysis of the effects of various methods in terms of over- or under-estimation of true growth rates.

#### Effect of a period of slower or non-growth

There is relatively minimal information on the timing and fashion of olivine crystal growth in the literature. This is because observing and measuring accurate growth rates at magmatic temperatures is a challenging task with conventional techniques. The vessels traditionally used for dynamic experiments (e.g. vertical tube furnaces) do not grant access to live, in situ observations, thus relying on the total time between initial and final states of matter as the single temporal constraint (Fig. 7). Thus, it is difficult to determine when nucleation occurred, how the crystal formed, and whether crystal growth was still an active process at the time of the quench. When the process of crystal growth is not directly observed, the mean growth rate  $G_{mean}$  is routinely calculated as the half-length of the crystal divided by the time spent under the liquidus:

$$G_{mean} = \frac{L^{\{hkl\}}}{2 \times t_{total}} \tag{5}$$

where L<sup>{hkl}</sup> is the entire crystal dimension measured from the center of one interface {hkl} to its opposite (Fig. 1b), and ttotal the total duration. There are three main problems with this calculation. First, the measured dimension must correspond to a length L<sup>{hkl}</sup> formed along a true direction of growth. In fact, a crystal length may result of the combination of different faces growing laterally. Second, using the half-length of the crystal implies that the process of crystal growth is perfectly symmetrical from start to finish, from the crystal center to the two opposite interfaces  $\{hkl\}$ , such that  $L^{\{hkl\}} = 2 \times L^{(hkl)}$ . Third, the growth rate is calculated as a single value, which implies that the advance speed in the measured direction is constant over the time considered. This type of calculation is hence only correct for a crystal length that formed entirely through linear and symmetrical growth. Conversely, this equation is: not appropriate to describe an advance speed that is fluctuating over time.

In practice, the total time considered can include one or several period(s) of slower or non-growth, for example incubation prior to nucleation, and stages of acceleration or deceleration (Fig. 6). The

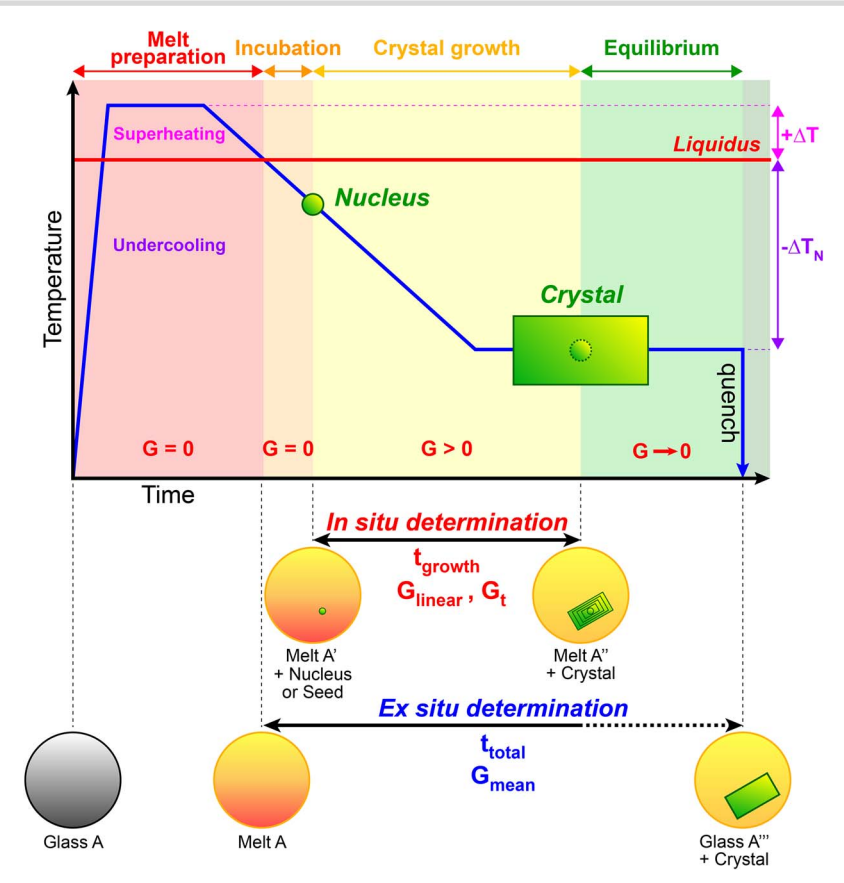


Figure 7. Sketch of the different stages occurring during a dynamic crystallization experiment aiming at determining the growth rates of a given mineral using either a direct, in situ approach, or an indirect, ex situ approach. Differences in time windows of observation may introduce errors in the calculated growth rates (see text for details). The final undercooling is noted  $-\Delta T_N$  as nominal only. "G" indicates the value of growth rates for each stage (see Table 1).

mean growth rate of a given interface, measured from the center of the crystal outward, represents a weighted average of each of these periods p of crystal growth such that:

$$G_{mean} = \sum_{p=1}^{n} \frac{G_{true,p} \times t_{p}}{t_{total}}$$
 (6)

In the general case of single-step cooling (Fig. 7), a typical estimation of the mean growth rate ( $G_{mean}$ ) would lead to an average of up to five different time periods: an incubation period at  $G_{incub} = 0$ , an acceleration period at  $G_{acc}$ , a period of linear growth at  $G_{linear}$ (that corresponds in our experiments to the maximum value such that  $G_{linear} = G_{max}$ ; Fig. 6), a deceleration period at  $G_{dec}$ , and an equilibrium period at  $G_{eq}$  tending to zero. For a given interface (hkl), the mean growth rate can be expressed as:

$$G_{mean} = \frac{G_{incub} \times t_{incub} + G_{acc} \times t_{acc} + G_{linear} \times t_{linear} + G_{dec} \times t_{dec} + G_{eq} \times t_{eq}}{t_{incub} + t_{acc} + t_{linear} + t_{dec} + t_{eq}}$$
(7

Equation [7] is the expansion of Equation [6], using an approximation of a constant, average growth rate for periods of nonlinear growth. Any period of time that precedes or follows a crystallization event must be subtracted from the total time in the calculations, including the incubation period and the equilibrium period, but also any period of time spent above the liquidus, such as the period of superheating, where the growth rates are by definition null. The nucleation delay of olivine has been

constrained at 6 to 60 min (Donaldson, 1979), and it can also be calculated at 3 to 29 min using the data provided in Sossi and O'Neill (2016; see Appendix B14), although it is strongly affected by several parameters such as the cooling rate, the undercooling, and the superheating (Donaldson, 1979; First et al., 2020). Depending on how crystallization proceeds, the incubation period may be shortened if heterogeneous nucleation occurs, or there may be no incubation period at all if the nucleation is bypassed with the use of seeds in the case of our experiments. There may not be a deceleration period and an equilibrium period if the crystallization was stopped by a foreign object in the melt or by quench before the end of the projected period of linear growth. The acceleration period may or may not be discernible on the experimental scale but it is required to bring the system from no crystal growth to the maximum growth rate. Together with the period of linear growth, these growth periods make the construction of the crystal possible. We stress however that this is the simplest case of crystallization, and linear growth may not happen if the P, T, X conditions in the environment vary, e.g. such as during an event of magma decompression, convection or mixing.

There are several implications for the use of the total subliquidus run time in the calculation of a  $G_{mean}$  as a proxy of  $G_{linear}$ . First, this type of calculation is prone to lead to underestimations in Glinear, due to the inclusion of periods of slower and/or nongrowth (Fig. 8). In general, the discrepancy between Glinear and G<sub>mean</sub> increases proportionally whenever a period of slower or non-growth is included in the calculation. For instance, the mean growth rate  $G_{mean}$  will be up to 10% lower than the maximum,

linear growth rate Glinear if 10% of the total time is comprised of period(s) of non-growth.

Both the incubation period and the acceleration period depend on the cooling rate (Donaldson, 1979); both nucleation and crystal growth can happen either during the cooling ramp, or after reaching the dwell temperature. Assuming that acceleration is at all times positive and that deceleration is at all times negative, the growth rates  $G_{acc}$  and  $G_{dec}$  for the periods of acceleration and deceleration can be described using a mean acceleration ( $\overline{a}_{acc}$  and  $\overline{a}_{dec}$ , in m/s<sup>2</sup>) as:

$$\overline{a} = \frac{\Delta G}{\Delta t} \tag{8}$$

$$\overline{a}_{acc} = \frac{G_{linear} - G_{incub}}{t_{linear}^{i} - t_{incub}^{f}} \text{ and } \overline{a}_{dec} = \frac{G_{eq} - G_{linear}}{t_{eq}^{i} - t_{linear}^{f}}$$
(9)

and using a true acceleration function with boundary conditions  $G_{incub} = G_{eq} = 0$  as:

$$G_{acc} = \int_{t_{i_{moral}}^i}^{t_{i_{inear}}^i} a(t)_{acc} dt \text{ and } G_{dec} = \int_{t_{i_{moral}}^i}^{t_{eq}^i} a(t)_{dec} dt$$
 (10)

where  $t_{incub}$ ,  $t_{linear}$ , and  $t_{eq}$  are the initial (i) or final (f) time stamps of each period. In a scenario of a single step-cooling, the three periods  $t_{acc}$ ,  $t_{linear}$ , and  $t_{decc}$  constitute the time sequence during which a crystal will form through the exhaustion of the supersaturation in the melt. Because those considerations have been rarely considered in the geoscience literature [if only by subtracting the incubation period from the total run time, e.g. Sirbescu et al., 2017, Rusiecka et al., 2020 and Devineau et al., 2020], we stress that these three periods should be constrained to the best extent possible when determining growth rates. Based on our experiments, the three periods of crystal growth can be evidenced from the seeds with the addition of (1) a first thin layer of olivine formed at accelerating growth rates, (2) a second thick layer built at the maximum, linear growth rate, and (3) a third thin layer formed at decelerating growth rates (Figs 3, 5 and 6). The mean growth rate for an interface {hkl} of a crystal formed during a one-step cooling could be thus constrained to:

$$G_{mean} = \frac{L_{acc} + L_{linear} + L_{dec}}{t_{acc} + t_{linear} + t_{dec}}$$
(11)

This Equation [11] still yields  $G_{mean} < G_{linear}$ , due to the inclusion of acceleration and deceleration periods, but Equation [11] returns a value closer to G<sub>linear</sub> than does Equation [7], which includes periods of non-growth (i.e. with no related crystal segment). Therefore, even if the overall time of crystal growth is better constrained (by subtracting the periods of non-growth, i.e. incubation and equilibrium, from the total time), the mean growth rate estimated using a half-length L(hkl) still represents an average over time between each layer of crystal formed at different growth rates, such that:

$$G_{mean} = \frac{1}{n} \sum_{p=1}^{n} \frac{L_p^{(hkl)}}{t_p}$$
 (12)

where n is the number of growth periods considered. If periods of acceleration and/or deceleration are part of the crystal's growth history (a reasonable assumption for almost all crystals) then this approach leads to underestimations of the maximum growth rate. Including a period of slower growth at an average rate that is at least five time slower than the period of maximum growth ( $G_{low} \leq 0.2 \times G_{linear}$ ) will produce a negative error on Glinear that is approximately the same as that of the error generated by a period of non-growth of equal duration (i.e. t<sub>incub</sub>, t<sub>eq</sub>; Fig. 8).

All these considerations indicate that the maximum, linear growth rate Glinear of a given crystallization event is a difficult parameter to assess accurately as long as the period of linear growth t<sub>linear</sub> is not isolated properly from the other periods of slower or non-growth  $(t_{incub}, t_{acc}, t_{dec}, t_{eq})$ . In our experiments, the period of linear growth can be isolated from the periods of slower or non-growth with a plot of cumulative overgrowth thickness versus elapsed time (Figs 4 and 5). Ideally, the periods of slower and non-growth should always be subtracted from the total time, so the remaining duration is closer to the actual period of construction of each half-length of the crystal. However, it is important to consider that the incubation period t<sub>incub</sub> will have a large effect on the total growth rate  $G_{mean}$  only for crystallization periods of short duration, when the incubation and the growth periods are of the same order of duration. Its effect on the total growth rate  $G_{mean}$  will be less and less prominent as the total time increases. In this case, the total growth rate  $G_{mean}$  can approach the maximum, linear growth rate Glinear if the acceleration is rapid, the crystal growth is linear through the rest of the considered duration, and it has not started to decelerate at the time of the quench. On the other hand, the equilibrium period teg can become a large source of error on  $G_{linear}$ . This can happen when the crystallization has not been stopped (e.g. by sample quench, either in the lab or by natural eruption) before the deceleration in the growth rate. In theory, a crystal can stay in equilibrium for an infinite period of time as long as the conditions P, T, X are invariant, and by using such a large period of time during which crystal growth is very slow or non-existent, the calculated Gmean will appear very low and far below the true value of  $G_{linear}$ . These cryptic time periods are likely to create larger growth rate errors for plutonic rocks than for volcanic rocks, but they must be considered and addressed to the best extent possible in both cases.

#### Effect of the crystal orientation

Because growth rates are a function of crystal length, their accuracy depends on the accuracy of the crystal dimension measurement (L), given the hypothesis that:

$$G_{linear} = \frac{L_{linear}^{(hkl)}}{t_{linear}} \tag{13}$$

with  $L_{linear}^{(hkl)}$  being the crystal half-length formed entirely by linear growth over a period of linear growth  $t_{linear}$  (Fig. 6a). In turn, this accuracy on the crystal dimension depends on the orientation of the crystal with respect to the plane of observation. In our experiments, the field of view in the microscope is essentially an orthographic projection (e.g. Levoy et al., 2006). The absence of significant perspective transformation towards a vanishing point is evidenced with the experiment at 38°C of undercooling, where the crystal does not show any significant narrowing of its width L<sup>(001)</sup> as the focal length increases (i.e. the extremity touching the bottom of the melt inclusion is as wide as the one against the top in Figs 2 and 3). Thus, in these experiments our view of each crystal is essentially an orthogonal, 2D-projection onto the focal plane. A crystal dimension will appear unchanged (i.e. the measured L is the true L) when it is perfectly parallel to the projection plane. The growth velocity measurement is ideal when the surface of the crystallographic interface of interest is

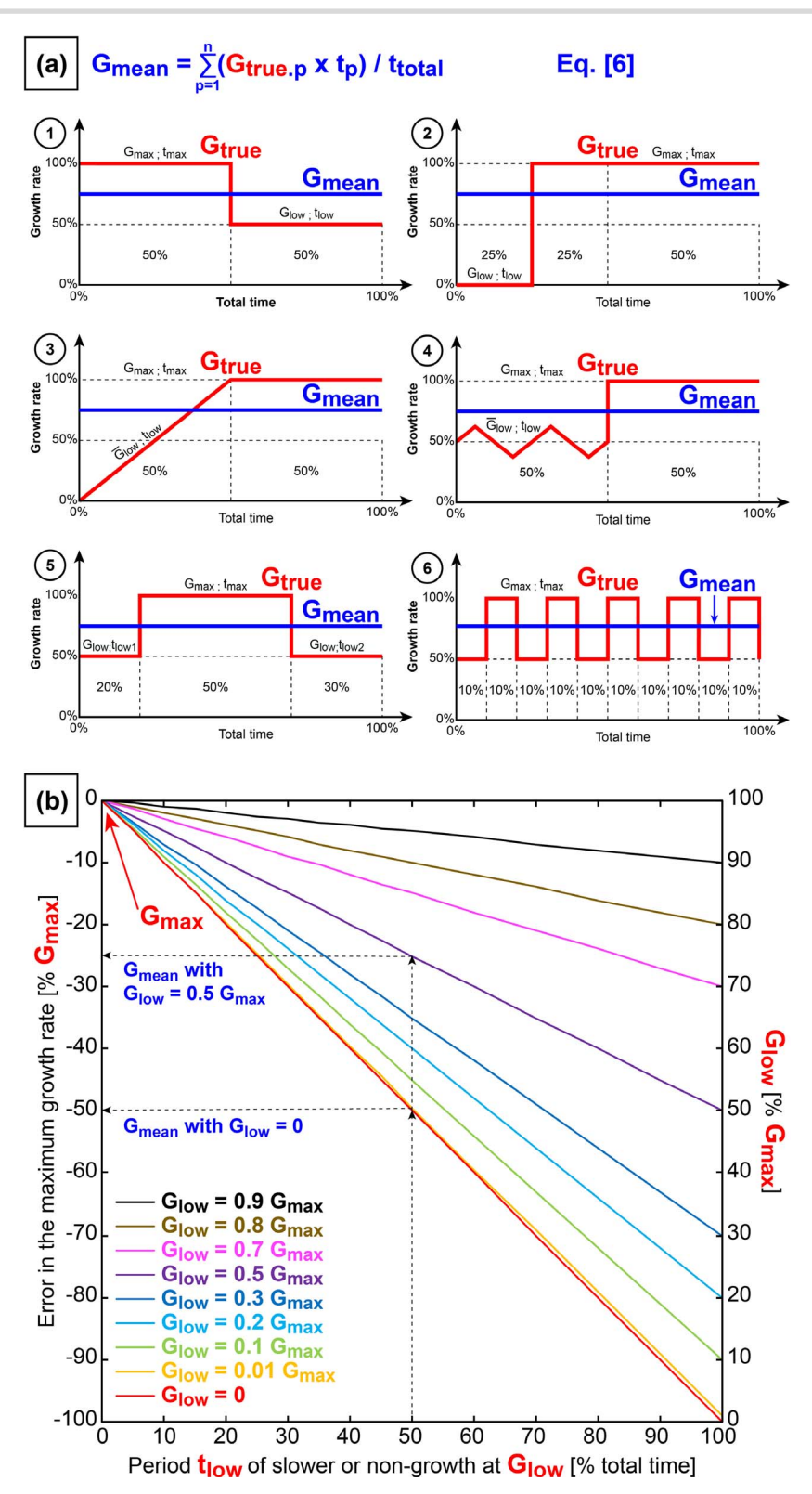


Figure 8. (a) Hypothetical kinetic patterns of crystal growth (G<sub>true</sub>, the connected line segments spanning various growth rates, in red) that would lead to the same mean value of growth rate ( $G_{mean}$ , the continuous horizontal line in each panel, in blue) by average of the kinetic variations weighted by time. This illustrates how growth rates can be misevaluated during routine analysis, and how information can be compressed and lost when using a time window that encompasses changing growth rates. (b) First approximation error in the maximum growth rate calculated as the mean growth rate over total time for a crystallization event that includes time intervals set at two different growth rates, one at a linear, maximum growth rate (here  $G_{linear} = G_{max}$ ) and one at slower growth rate (either  $G_{low} = 0.01 \times G_{max}$  to  $0.9 \times G_{max}$ , or  $G_{low} = 0$ ) using Equation [6]. For instance, an incubation period  $(G_{low} = 0)$  making up 50% of the total time (the remaining 50% being crystallization at  $G_{max}$ ) induces an error of 50% in the average growth rate  $(G_{mean} = 0.5 \times G_{max})$ . A period of slow growth at  $G_{low} = 0.5 G_{max}$  also at 50% of the total time would lead to an error of 25% on the maximum growth rate, so that  $G_{mean} = 0.75 \times G_{max}$ , as illustrated in (a). Any growth rate that is at least two orders of magnitude lower than the maximum growth rate  $(G_{low} \le 0.01 \times G_{max})$  leads to negative errors on the true maximum growth rate that are similar to those induced by null growth rates.

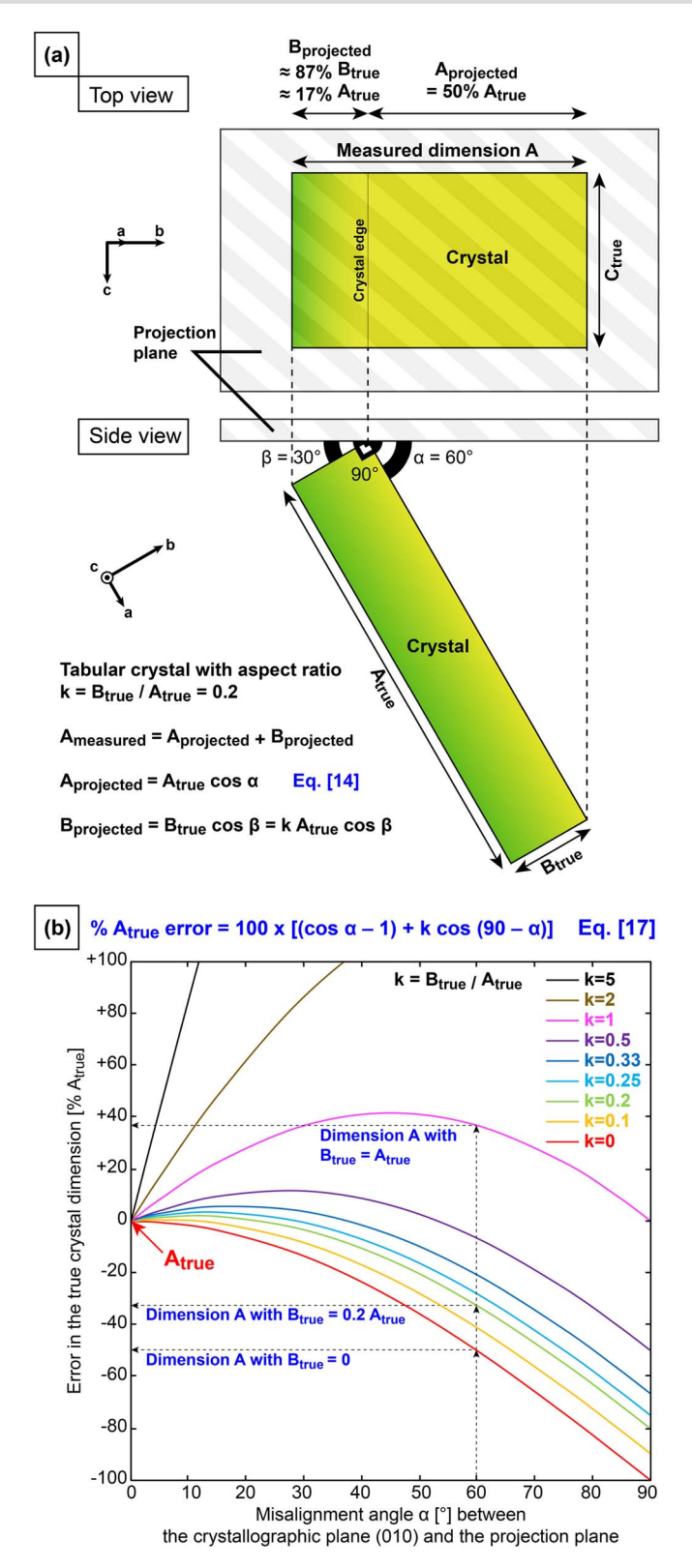


Figure 9. (a) Sketch of the projection of a tabular crystal of dimensions  $A_{true} \times B_{true} \times C_{true}$  and inclined at an angle  $\alpha$  with the projection plane (misalignment of the (010) plane by rotation around the c-axis, with the example here at  $\alpha = 60^{\circ}$ , and a shape ratio  $A_{true}$ :  $B_{true}$  at 1:0.2), showing discrepancies between true crystal dimensions and their 2D-projections. The projected crystal shows a blending of the two dimensions A and B over the crystal edge when measuring the dimension A. (b) First approximation error in the measurement of the crystal dimension  $A_{true}$  using Equation [17]. For a crystal with no thickness ( $A_{true}$ :  $B_{true} = 1:0$ ) and titled of 60 ° with respect with the projection plane, the dimension A has a projected length reduced by 50% in comparison with the true dimension. For a crystal of aspect ratio  $A_{true}$ :  $B_{true} = 1:0.2$  (similar to tabular olivine in some cases) and also titled by 60° with respect with the projection plane, the error in the dimension A is partially mitigated at ~67% (50% + 17%, i.e. a negative error of  $\sim$ 33%) due to the blending of the dimension B in the field of view ( $B_{projected} = 87\%B_{true} = 17\%A_{true}$ ). Note that the error on the dimension A becomes positive (i.e.  $A_{true} < A_{measured} = A_{projected} + B_{projected}$ ) when the crystal becomes stubbier (e.g.  $A_{true} : B_{true} = 1 : 0.25$  and beyond; see the upper four curves in purple, pink, brown, and black) and as the dimension B starts dominating the field of view at moderate and high inclination angles.

normal to the projection plane (i.e. when the direction of growth is perfectly parallel to the projection plane). For example, this is why we can track the growth of olivine forms {101}, {001} and {100}, but not forms {021} and {110}, when (010) is parallel to the plane of observation. On the other hand, a dimension will be increasingly foreshortened when it is dipping away from the projection plane. The extent of foreshortening between a true crystal dimension and its projection can be approached as a simple geometry problem (Fig. 9a). Using a tabular (orthorhombic) crystal of dimensions  $A_{true} \times B_{true} \times C_{true}$  tilted at an angle  $\alpha$  with the projection plane (given here in degrees [°], by rotation of the (010) plane around the c-axis), the relation between the dimension Atrue and its counterpart Aprojected is:

$$A_{projected} = A_{true} \times \cos \alpha \tag{14}$$

Hence the absolute error on Atrue can be calculated as:

$$A_{true} \ error = A_{projected} - A_{true} = A_{true} \times (\cos \alpha - 1)$$
 (15)

And the relative (%) error on Atrue is:

$$%A_{true} error = 100 \times (\cos \alpha - 1)$$
 (16)

Considering a simplified crystal with no B dimension (i.e. no thickness), % $A_{true}$  error ranges from 0% at  $\alpha = 0^{\circ}$  to 100% at  $\alpha = 90^{\circ}$ . In reality, a crystal has  $B_{true} > 0$  and will have a smaller negative error because the dimension B enters the field of view and blends in with dimension A as the crystal's edge goes out of focus (Fig. 9a). In this case, the measured dimension A actually represents a composite dimension A<sub>projected</sub> +B<sub>projected</sub> with a percent error on Atrue of:

$$A_{true} error = 100 \times [(\cos \alpha - 1) + k \times \cos (90 - \alpha)]$$
 (17)

with  $k = \frac{B_{true}}{A_{true}}$ , the aspect ratio of the true dimension B (thickness) over the true dimension A (length). The modeling given in Fig. 9b suggests that, for a crystal with thickness approaching zero, a tilt smaller than 26° will produce a negative error of 10% or less on the measured dimension A ( $A_{projected} = 0.9 \times A_{true}$  when k = 0 and  $\alpha = 26^{\circ}$ ). This error is reduced in thicker crystals, because  $B_{projected}$ contributes to the total measurement, and the 10% negative error mark occurs at higher angles (A $_{projected} = 0.9 \times A_{true}$  at  $\alpha = 37^{\circ}$  when k = 0.2, or at  $\alpha = 49^{\circ}$  when k = 0.5). This simple modeling suggests that foreshortening of the A dimension is partially mitigated for any k between 0 and 0.25, i.e. when the length A dimension is at least four time as long as the thickness B dimension. This is the case for the early stages of olivine growth as shown in Figs 1-3 and 5. Above that threshold ( $k \ge 0.25$ , i.e. in thicker crystals) the error on Atrue due to projection of a dipping crystal is fully compensated or even rendered positive at high dipping angles. This is the corner case in which a dimension can be overestimated and lead to growth rates ostensibly faster than the true growth rates. This artifact occurs because the total dimension  $A_{projected}$  + B<sub>projected</sub> appears as two opposite fronts of crystallization distancing themselves within the projection plane, but in reality their displacements are orthogonal to each other in 3D. High dipping angles ( $\alpha > 45^{\circ}$ ) will cause depth dimensions to become plane dimensions (i.e. B<sub>projected</sub> will gets closer to alignment with the horizontal plane and dominate the field of view over Aprojected), and

the measured dimension will be hence more representative of B<sub>true</sub> than Atrue. In such case, the error on the dimension is in essence an issue in the crystallographic indexing for the dimension rather than in the measurement itself.

In summary, when measuring randomly oriented crystals with strong shape anisotropy (such as olivine with  $A_{true} > C_{true} > B_{true}$ ; Figs 1-3 and 5), the long dimension A will tend to be underestimated. This is because their blending with the shortest dimension B (k < 0.25) will not be enough to compensate their foreshortening. When the tilt is only moderate ( $\alpha \leq 15^{\circ}$ ), as it appears to be the case for the crystals formed at 19°C, 57°C and 96°C of undercooling (Figs 2-3), the error on the long dimensions A and  $L^{\{101\}}$  is small (-4% or less). On the other hand, the measurements of the shortest dimension B of a crystal will likely lead to some overestimations as the other long dimensions will blend in the projection (k = 0.5 in Fig. 9b). An intermediate dimension C may however lead to both cases: depending on the tilt, C can be underestimated if it is blending with a shorter dimension B (with  $B_{true}/C_{true}$  < 0.25) or overestimated if it is blending with a longer dimension A (with  $C_{true}/A_{true} \ge 0.25$ ).

Another implication of the blending of a depth dimension on one side of the crystal is that this half-length of the crystal will appear longer than the other one, obfuscating symmetrical growth. This effect can be however deconvolved in skeletal and dendritic olivine crystals given that their center is usually framed with symmetrical embayments or melt inclusions. The above modeling is based on a simple geometry to allow first approximations on the deviations from the true dimensions, and these errors will vary to some extent with the crystal geometry and the type of interface that is measured (flat or re-entrant face, edge, vertex, or dendrite tip; Fig. 1).

Assessing crystal dipping angle. Our observations suggest that a correction factor should be applied to every crystal dimension measured with a microscope in order to approach their true values. Corrections factors can be estimated from simple modeling of the projected dimensions (Fig. 9b), provided that the dipping angle is known. The dipping angle can be estimated through the aspect ratio of the crystal from predictions of the crystal morphology through the atomic structure of the mineral (Bravais, 1848; Friedel, 1911; Donnay & Harker, 1937) and the attachment energy of building units (Hartman & Perdok, 1955a, 1955b, 1955c), but using such approach can generate additional uncertainties and erroneous corrections on the crystal geometries given that crystals can develop various aspect ratios depending on their growth environment (e.g. Lewis et al., 2015). Another method would be to constrain the dipping angle  $\alpha$  (i.e. the pitch) by measuring the optical depth between two focal points, reporting the focal depth for the shallow front part of the crystal, and the focal depth for the back part of the crystal. The vertical depth is calculated as the difference of z-focus on the fine adjustment knob after calibration with another object of known thickness (Brattgård, 1954; Galbraith, 1955; Harris, 1985). The crystal may have a second angle of rotation (i.e. the roll), which can be corrected by using the longest diagonal on the projection plane to rebuild a rectangular shape with 90° corners. Although these optical depths were not measured during our experiments, we can qualitatively assess the dipping angle of the crystals thanks to the depth of focus. If a crystal is parallel to the plane of observation its entire shape will be observed in-focus (crystals appearing entirely sharp at 19°C, 57°C, and 96°C of undercooling; Fig. 2). If the crystal is dipping, parts of its shape will be out of focus (crystals appearing partially blurry at 38°C, 77°C, and 129°C of undercooling (Fig. 2).

Implications for measured dimensions. In our experiments, misalignments with the projection plane are also identified when symmetrically equivalent interfaces show significant growth velocity dispersion, as shown in crystals at 38°C, 77°C, and 129°C of undercooling (Figs 2–4). The dimensions L<sub>linear</sub> (and so the growth rates  $G_{linear}$ ) can be underestimated when the crystals do not have their faces perfectly aligned with the projection plane. We estimate that our measurements capture ~71% to 100% of the true values of crystal dimensions, given that most of the crystals have shapes that are visibly close to alignment with the projection plane (Fig. 2) and that the measurements of one of our most tilted crystals in the experiment at 38°C of undercooling (Figs 2 and 3b) represents 84% to 90% of the true dimension, i.e. a negative error of 10%–16% on the true value, or a correction factor of +11%–19% on the measured value (Equations [3] and [4]). Because this crystal touches both the front and the back walls of the melt inclusion, the error can be determined using Pythagoras's theorem in a right triangle with the measured values of 80  $\mu m$  for the dimension  $L^{\{100\}}$  and 64  $\mu$ m for the depth z of the melt inclusion, the tilt being calculated as  $\alpha = \arctan(64/80) = 39^{\circ}$ , and the related negative error on the true dimension being 10%-16% assuming an aspect ratio k in the range 0.1-0.2 (Figs 1 and 9). In other words, the raw measurement represents 84% to 90% of the true growth velocity considering a dipping angle of 39 ° with the projection plane and a crystal thickness  $L^{\{010\}}$  that is 5 to 10 times smaller than the length L<sup>{100}</sup>. This corresponds to corrected values of 89–95  $\mu$ m for the dimension  $L^{\{100\}}$  (using Equation [4] and a correction factor at +11% to +19% on the raw measurement at 80  $\mu$ m), which compares well with the length  $L^{\{100\}}$  (97  $\mu$ m) in the Series [B] replicate experiment (Fig. 5a; Table 2). Similarly, we note that the crystal formed during experiment [180] and its replicate [181] may have dendrite tips growing at high angles to the projection plane given that their orientations do not allow observation of perfect swallowtail shapes (Figs 3f and 5e), and that their apparent linear growth velocities  $G_{linear}^{(101)}$  are relatively low and scattered (Table 2, Supplementary Material A).

If the tilt is between 0 and 30°, measurements performed on 2D crystal projections will have an error between -13% and +12% if  $k \le 0.5$ , and between -13% and -3% if  $k \le 0.2$  (Fig. 9b). In general, the negative error will be less than 50% for dimensions that are misaligned with the plane of observation at  $\alpha \leq 60^{\circ}$ , and prior to any error reduction due to blending with shorter dimensions. In other words, in heating stage experiments, the advance speeds of interfaces observed through the lens usually account for more than half of the true growth velocities ( $\geq 0.5 \times G_{true}$ ), and are typically much closer than that to  $G_{true}$ .

We emphasize that the modeling given in Fig. 9 offers a first approximation of the error on a crystal dimension measured on the 2D-projection of an entire crystal of simple geometry. It is not directly applicable to crystals in thin sections since their dimensions are often truncated due to cutting and polishing, leading to larger negative errors on the measurements. This loss of information can be particularly problematic in the case of BSE images (i.e. a 2D-shape with virtually no thickness) and photomicrographs of thin sections (i.e. 30  $\mu m$ thick slices of millimetric phenocrysts), especially when the sections are off center of the crystals (Armienti, 2008). In our study and that of Jambon et al. (1992), crystal growth velocities are closer to Gtrue and are less variable because the images are 2D projections of complete 3D objects (each crystal is entirely circumscribed within the melt inclusion) rather than truncated grains; this is another key advantage of heating stage experiments.

#### Comparisons with a key previous dataset

Ardoukoba plagioclase crystals from the same sample set were used in a seminal crystal growth study by Jambon et al. (1992). Given the parallels between this study and our own, we delve into some important distinctions and corrections, detailed below.

#### Errata and corrections

Jambon et al. (1992) measured optically growth rates in the range of 8  $\times$  10<sup>-11</sup> to 6  $\times$  10<sup>-7</sup> m/s using a similar experimental set up as ours, at unspecified cooling rates and undercoolings of 15°C, 30°C, 35°C, 71°C, 100°C, and 150°C in six separate melt inclusions. The raw data are not published, but growth rates can be retrieved from reconstructions of their Fig. 4 (grain size versus run time) as provided in the Supplementary Material B5. Although not stated explicitly in the paper, it is clear from these reconstructions that the reported growth rates assume symmetrical growth by using half-slopes. We also note two errata in their Table 2. First, the order of magnitude of growth rates should be given as  $10^{-9}$  m/s instead of 10-8 m/s to match both the results given in their Fig. 4 and the range of growth rates given in-text. Second, the headers " $V_{Ol}$ " and " $\overline{V}_{Ol}$ " in the table caption should be swapped to reflect appropriately the growth rates given in their Fig. 4, with  $V_{\text{Ol}}$ referring to the optical measurements, and  $\overline{V}_{Ol}$  and  $\overline{V}_{Pl}$  referring to the mass-balance calculations. One evidence for this is the fact that the fourth column with multiple entries of growth rates for each undercooling can only correspond to multiple optical measurements of a single crystal at different times; on the other hand, the sixth column with one single value of growth rate for each undercooling must correspond to growth rates determined by mass-balance calculations since only one growth rate can be determined from one chemical composition of residual melt. We emphasize that the values of growth rates given in-text at  $8 \times 10^{-11}$  to  $6 \times 10^{-7}$  m/s correspond to the values obtained by optical measurements, and not those estimated by mass-balance calculations.

Our reconstruction of the Jambon et al. (1992) dataset shows slopes and linear growth rates similar to those in their original dataset, for four of the six experiments (at 15°C, 30°C, 100°C, and 150°C of undercooling; Fig. 10, see also Supplementary Material B5). The reconstructions for the other two experiments (at 35°C and 71°C of undercooling) show a growth rate dispersion of one order of magnitude between our determinations and theirs. We suggest that their growth rates are artificially lower because their linear regressions include the acceleration and deceleration periods, rather than only the periods at linear, maximum growth. Based on our reconstructions, their maximum linear growth rates should be  $\sim 2.6 \times 10^{-8}$  m/s for 35°C of undercooling, and  $\sim 1.7 \times 10^{-8}$  $10^{-7}$  m/s for 71°C (instead of 2.4 ×  $10^{-9}$  m/s and 2.8 ×  $10^{-8}$  m/s, respectively; Fig. 10, Supplementary Material B5). Given that both of our studies used a similar experimental set up, it is likely that their growth rates are subject to the same uncertainties regarding the measurement of crystal dimensions, i.e. that the adjusted growth rates should capture more than 50% of the true velocities for tilt angle  $\alpha < 60^{\circ}$ .

#### Limitations to mass-balance calculations

The growth rates estimated in Jambon et al. (1992) by massbalance calculations using the residual glass composition are not as accurate as optical measurements, and most of them are lower (their Table 2; Fig. 10). The discrepancy is relatively small at low undercoolings (with the growth rates being 46% faster and 11% slower at 15°C and 30°C than the ones measured

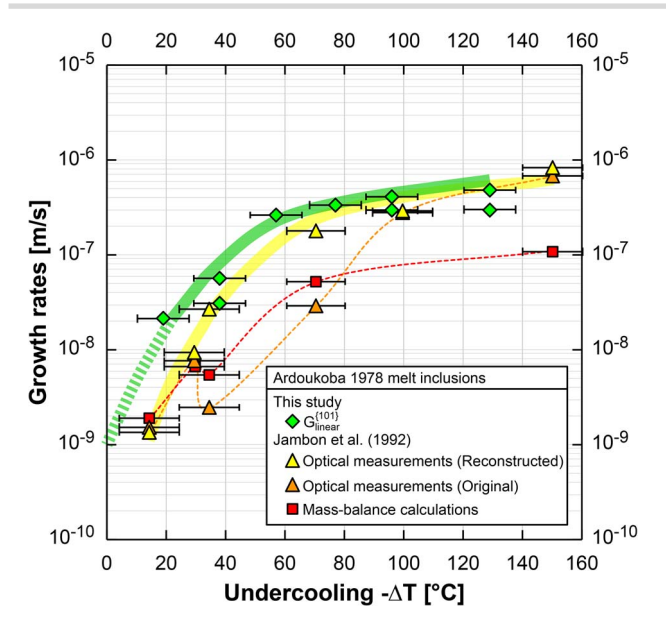


Figure 10. Log of olivine growth rates versus undercooling for heating stage experiments with plagioclase-hosted melt inclusions from the Ardoukoba 1978 eruption, including this study and that of Jambon et al. (1992). The values obtained by optical measurements in Jambon et al. (1992) were reconstructed from their figure 4 (grain size versus elapsed time) and adjusted for the stages of linear, maximum growth (see Supplementary Material B5 for details). These reconstructions suggest that their original growth rates determined at 15°C, 30°C, 100°C and 150°C are correct. We recommend, however, using our adjusted values for the growth rates measured optically at 35°C and 71°C of undercooling. The curves of growth rates fitting our dataset (upper curve, green, dashed at low undercooling) and that of Jambon et al. (1992) (lower curve, yellow) are preliminary outlines drawn by hand. The two datasets show essentially the same profile shape, just offset by ~12°C of undercooling or less, presumably due to uncertainties on the liquidus (1173 $\pm$ 5°C for our dataset and  $1180 \pm 2$ °C for theirs) and the run temperatures ( $\pm$  7°C and  $\pm$  10°C, respectively).

optically, respectively) but large at moderate and high undercoolings (79%, 70%, and 83% slower at 35°C, 71°C, and 150°C, respectively). There are various limitations inherent to massbalance calculations, beyond the analytical uncertainties on the chemical compositions, and problems related to the time window considered (Discussion § Effect of a period of slower or nongrowth). In theory, reasonable values of component loss can be calculated from time-constrained analyses of the glass's chemical composition, assuming that the melt is homogeneous at the time of its solidification. This assumption breaks down during rapid growth as boundary layers form around the crystals, resulting in a chemically heterogeneous melt. These boundary layers induce spatial and compositional bias in the results, tending to an underestimation of the component loss. This could be part of the reason why Jambon et al. (1992) obtained lower values of growth rates at moderate and high undercoolings, i.e. when the kinetics of crystal growth exceed the capability of the melt to re-homogenize in a timely fashion (Fig. 10). A second limitation is that the growth rates are determined by converting the loss of mineral components into a crystal of simplified geometry, such as a sphere, which is not easily equated to the complex, changing crystal habits of a mineral like olivine. The equivalence between spherical, isotropic growth and true anisotropic growth is not straightforward. The calculated growth rates likely correspond to intermediate values between the fastest interfaces and the slowest interfaces of the true crystal habit. This could be a second explanation for the larger discrepancies observed at moderate and high undercoolings in Jambon et al. (1992) as crystal shape anisotropies increase with the undercooling (Figs 1-3 and 5; Table 2). The true solution must be however more complex given that the crystal shape of olivine also changes with time (Figs 1-5). A third limiting characteristic of the mass balance model is that it virtualizes the component loss as growth of a single crystal, that is, considering only bulk crystallization and ignoring interactions between multiple growing crystals. Fortunately, Jambon et al. (1992) used only one seed (except in their experiment at 30°C of undercooling, where two crystals can be seen in their Fig. 3). This prevented potential deviations in component loss that would result from the combined interaction of crystals with their environment. The above arguments suggest that mass-balance calculations in general are underestimates of the true maximum growth velocities in the fast-growth directions, i.e. those typically

#### Differences between the two datasets

There are three notable differences between Jambon et al. (1992)'s

First, their study includes sketches of their olivine crystals but no time-referenced microphotographs, which does not allow verification that the crystals experienced symmetrical growth. In fact, Jambon et al. (1992) report in their Fig. 4 the increase in the grain size of whole olivine crystals and not their halflengths. Thus, the measurements assume perfect symmetrical growth, and that the reported growth rates represent averages between opposite interfaces. Because asymmetrical growth can and does occur (as observed in our replicate experiment at 38°C of undercooling; Fig. 5), their measurements bear this additional uncertainty. Although the absence of photomicrographs prevents attribution of the reported growth rates to specific forms {hkl}, it is likely that the highest growth rates measured at moderate and high undercoolings (35°C, 71°C, 100°C and 150°C) correspond to the propagation of the {101} vertices and primary branches, because no other parts of the crystal grow to that extent at those undercoolings (Figs 2, 3, and 5). In our case, this type of information is provided in the time series and the isochrone maps (Figs 2, 3, and 5) in order to visualize the crystallization patterns and contextualize the growth rates.

Second, the melt inclusions used in Jambon et al. (1992) are around 50–70  $\mu$ m in diameter, which is significantly smaller than the one used in our study, up to 204  $\mu$ m (Figs 2 and 3). This indicates that the period of linear growth is shorter in their experiments and that boundary conditions may have played a role sooner than in ours. Their measurements, which assume symmetrical growth, would not reflect this complexity, which is addressed in our study by measuring the advance of each interface separately. Another consequence of melt inclusion size is the fact that bigger melt inclusions are less affected by the crystallization of the seed, as they retain essentially their original chemical composition and inherent liquidus temperature at the start of the experiments.

Third, Jambon et al. (1992) determined the olivine liquidus to be  $1180 \pm 2$ °C for all of their six melt inclusions, while it is estimated at 1173 ± 5°C in our single melt inclusion. This difference of up to 14°C could explain why their growth rates measured optically are slightly slower than ours for a given undercooling (Fig. 10). If the lower liquidus temperature from our study is more accurate, the true undercoolings from Jambon et al. (1992) would be smaller than their stated values. The two datasets show however reasonable consistency given that the two curves of growth rates show a similar profile after corrections (green and yellow curves in Fig. 10 for the highest values measured at a given undercooling, presumably as tabular (100), and skeletal and dendritic (101) in Jambon et al. (1992); Supplementary Material B5). And both sets of olivine growth rates would match within uncertainties in Figs 10 and 11 if the same liquidus temperature was applied to calculate the undercoolings, i.e. similar growth rates are observed at the same temperature across the two studies using different melt inclusions and different heating stage microscopes by different users. This difference in liquidus temperature illustrates the difficulty in estimating optically the liquidus temperature, as the kinetics of crystallization and dissolution are very sluggish in its vicinity. There are, however, other contributing factors to consider in addition to seed location and the level of dehydration and oxidation of the melt inclusion (see § Experimental Methods and Appendix A5). For instance, the fact that their melt inclusions are smaller makes their liquidus temperature slightly more sensitive to the preparation of seeds. Jambon et al. (1992) also used a different melt inclusion for each experiment in order to perform the mass-balance calculations from post-mortem analyses. In general, using different melt inclusions can introduce a compositional bias that has effects on the growth rates, but this is unlikely to be a major issue in their experiments, given that the chemical composition of melt inclusions in these samples is relatively homogenous (Clocchiatti & Massare, 1985). These small differences in chemical composition may however lead to slight differences in liquidus temperatures from one melt inclusion to another.

#### Approaching the curve of true maximum growth velocities

In addition to Jambon et al. (1992)'s results, we examined how our new data fits with, and in many cases invites reinterpretation of, previous datasets. This extensive review is detailed in Appendix B. A case-by-case approach was necessary to assess the different growth rates. We recognize that minor editorial oversights are commonplace in scientific publications, and are typically not detrimental to the key points of the work; however, given the extensive use of the data from the articles in question, we must also draw attention to certain errata, miscalculations, and limitations, as discussed above for the study by Jambon et al. (1992). Based on the available information and raw data, we present corrections for some of these datasets in Fig. 11, Appendix B, and Supplementary Materials B - B19.

Examining all the available datasets allows us to draw a more accurate profile of olivine growth velocities in the olivine growth rate versus undercooling space (Fig. 11). Here a distinction can be made between growth rate measurements (provided by direct methods that use continuous observations of crystal growth to constrain  $G_{linear}$ ) and growth rate estimations (provided by indirect methods that reconstruct crystal growth with discontinuous observations to constrain  $G_{mean}$ ), as discussed in Richardson et al. (2002). Most of the highest values of growth rates reported at a given undercooling were measured with direct methods, while many of the lower values were estimated with indirect methods. A curve of maximum growth rates can be drawn between the values measured by Schiano et al. (2006) at low undercoolings  $(-\Delta T = 0.45-3.35$ °C) and those measured in our study at higher undercoolings ( $-\Delta T = 19^{\circ}C-129^{\circ}C$ ). Bridging these two datasets is supported by the fact that the melt inclusions used in Schiano et al. (2006) are relatively close in terms of chemical composition and temperature ranges to our melt inclusion (8.68-10.16 wt% MgO and 1134°C–1196°C versus  $8.2\pm1.2$  wt% MgO and 1036°C– 1146°C, respectively). The results of Jambon et al. (1992) also

fit if we recalculate their undercoolings using our liquidus determination (Discussion § Comparisons with a key previous dataset). Not only would their growth rates overlap with our values, but their growth rate of  $1.30 \times 10^{-9}$  m/s measured at 15°C of undercooling would also match that measured by Schiano et al. (2006) at 1.46°C of undercooling in Reunion melt inclusions (Supplementary Material B11). To that effect, we propose in Fig. 11 a preliminary profile of the curve of the true maximum growth velocities of olivine crystallizing from ~8 wt% MgO basaltic melt from ~0°C to 150°C of undercooling.

#### Significance of growth rates Pitfalls of growth rate determination

Our review of existing datasets (Appendix B) indicates that determinations of olivine growth rates have been limited both due to the methods used and how rigorously those methods have been applied (such as reported time reading and image scale). Growth rates are rarely determined as growth velocities, i.e. the values obtained do not relate directly to the advance speed of a crystal interface. This is the case for the measurements of unspecified growth directions, as well as for mass-balance calculations, kinetical partitioning and diffusion modeling. This is a concern given that olivine shows pronounced shape anisotropy during crystal growth, and several of its forms have their development discontinuous at moderate and high undercoolings (Figs 1 - 5). In the absence of textural information, growth rates cannot be unequivocally attributed to a specific interface. In some cases, the identity of crystallographic interfaces may be deduced from the provided textural data (e.g. Jambon et al., 1992), while in some others the reported growth rates approach true growth velocities [e.g. Schiano et al., 2006 in which only the dipping angle is unknown].

Another common problem occurs when symmetrical growth is assumed but not verified. Measuring the growth of two interfaces (rim-to-rim) instead of one (center-to-rim) can result in an overestimation of the growth rate by a factor two. Symmetrical growth can be deduced on an individual basis from the textural data provided in previous studies (e.g. Kirkpatrick et al., 1981; Jambon et al., 1992; Faure et al., 2007; Ni et al., 2014; Sossi & O'Neill, 2016). It is however important to note that symmetrical growth does not apply to the migration of melt inclusions (Schiano et al., 2006) and the displacement of large olivine fronts (Laumonier et al., 2019), since thermal gradients force crystal growth to be essentially unidirectional (Donaldson, 1977; Faure et al., 2006). There are at least three other cases that can lead to overestimation of growth rates for the measured direction: (1) when measuring the short dimensions  $L^{\{010\}}$  and in some cases the intermediate dimensions L{001} of olivine crystals, which may appear artificially longer in a 2D-projection due to blending with longer dimensions; (2) when constraining variable growth rates, such as those occurring during a period of acceleration or deceleration; (3) when measuring small growth increments that are near or under the image resolution. In contrast, measurements of the longer crystal dimensions (the most common approach) will usually result in underestimates of the true growth rate (as crystals are rarely perfectly aligned with the plane of observation and their dimensions are therefore foreshortened or even truncated in the case of thin sections; Discussion § Effect of the crystal orientation; Fig. 9).

The most problematic assumption of growth rates is that crystals are constructed entirely in a linear fashion over the full duration considered. However, tangible evidence of linear growth is sparse (Jambon et al., 1992; Park & Hanson, 1999; Cabane et al., 2005; Schiano et al., 2006; Ni et al., 2014; this study). The values

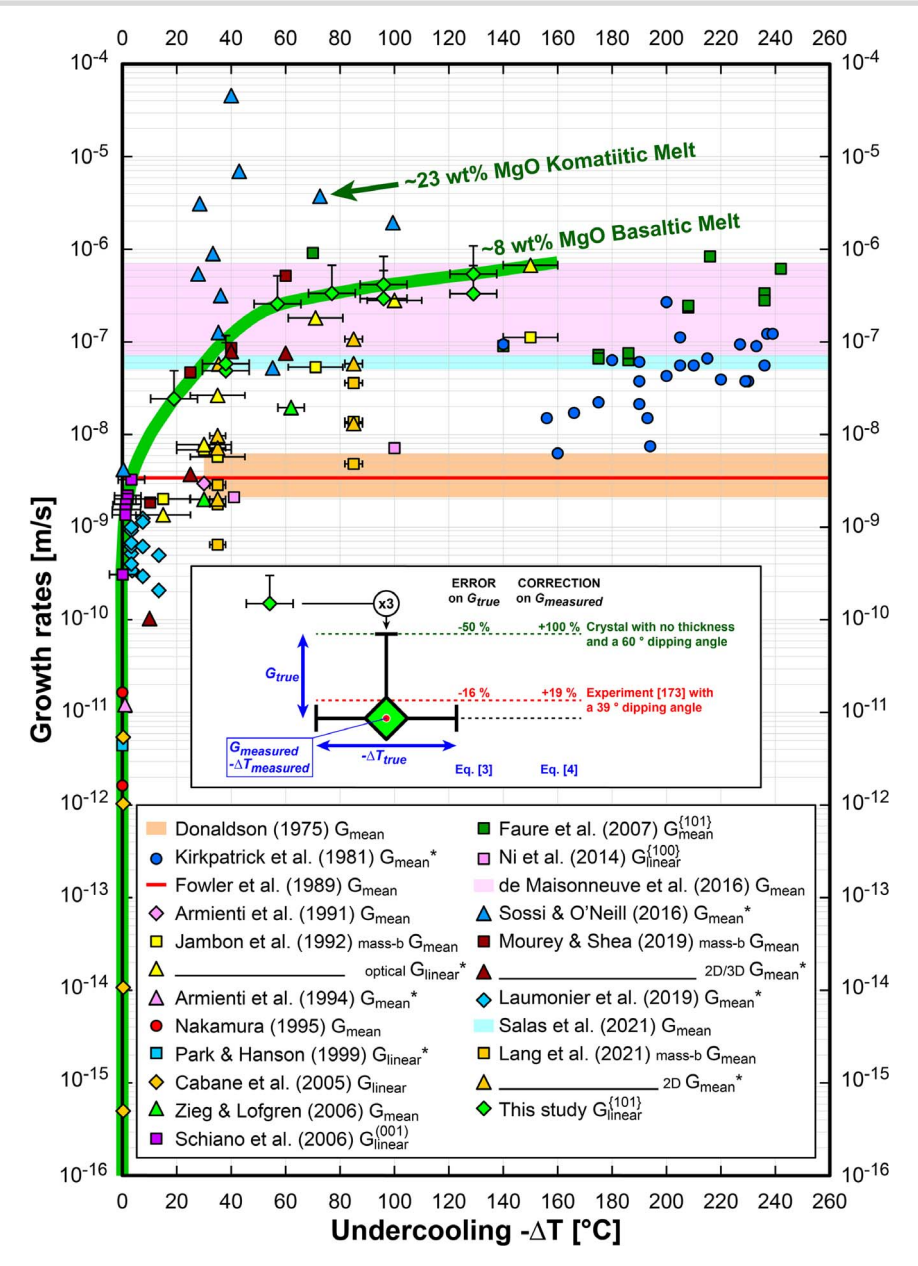


Figure 11. Log of olivine growth rates versus undercooling for 20 datasets. Star (\*) indicates that the values were reconstructed and/or adjusted as detailed in Appendix B and the Supplementary Material B. Most of the data displayed here can be considered lower bounds of the true maximum growth rates at the given undercooling. For our own data, we have included growth rate uncertainty estimates. Because there are very few ways to overestimate growth rate uncertainty, the bar extends from the measured data point upwards only. In our study, most of the true maximum growth velocities  $G_{true}^{(101)}$  were estimated to be  $\leq$ 19% higher than the measured values of linear growth velocities  $G_{linear}^{(101)}$  based on the projection foreshortening of the longest crystal lengths formed by the protrusions {101} (Discussion § Effect of the crystal orientation). Based on projections for experiment [173] the uncertainty of our measurements is smaller or equivalent to the symbol size. The generous upper bound of growth rate uncertainty displayed is 2x (100% of) the measured value. The shaded areas reference, in order of increasing growth rate, an orange rectangle for Donaldson (1975), a red line for Fowler et al. (1989), a blue rectangle for Salas et al. (2021), and a pink rectangle for Bouvet de Maisonneuve et al. (2016). Temperature uncertainties (1σ) are given at 10°C in Jambon et al. (1992), 5°C in Zieg & Lofgren (2006) and Schiano et al. (2006), 3°C in Lang et al. (2021), and 8.6°C in our study. An undercooling of 0.1°C was applied to the estimations given in Nakamura (1995) and Park & Hanson (1999), and of 0.3°C to the results given in Cabane et al. (2005) to account for the crystallization of olivine at conditions near equilibrium. The differences in techniques and methods imply that the uncertainty in the growth rates varies from one study to another. Our preliminary curve of growth velocities (in green, labeled "~8 wt.% MgO Basaltic Melt") is consistent with the dataset of Jambon et al. (1992) after corrections and considering uncertainty on the true liquidus temperature. Both datasets connect smoothly with the measurements of Schiano et al. (2006) at very low undercoolings. Taken together, these three datasets approximate the true maximum growth velocities of olivine in low-MgO basaltic melts (~8 wt% MgO, ~1100-1200°C).

given therein likely approach the true maximum growth velocities of olivine at the given undercoolings such that  $G_{linear} = G_{max} \approx$ Gtrue at tlinear (Fig. 8). In contrast, the occurrence of a period of linear growth is less clear in the other datasets examined here, as these values correspond to mean growth rates  $G_{mean}$ . And because crystallization kinetics vary with time, determining mean growth rates as a linear value, when they are actually varying over time, will lead to underestimates of the true maximum growth velocities (Figs 7–8). In essence, crystal growth is made of short periods at maxima and longer periods at minima. Strong kinetic variations can be presumed in natural crystals given that olivine growth rates span over 10 orders of magnitude (Fig. 11). This challenges the general determination of growth rates as weighted averages, because incorporating periods of growth that are slower than the maximum by at least 2 orders of magnitude has a comparable effect to incorporating periods of zero growth (Fig. 8).

It is hence likely that most of the previous datasets represent lower bounds of the true maximum growth velocities. The differences in melt chemistry, crystallization conditions, and experimental and analytical methods from one study to another make the uncertainty in the growth rates extremely variable from one dataset to another (Fig. 11). This indicates that high quality measurements are needed to quantify properly the crystallization kinetics of olivine, and this is only possible when the different variables are well constrained.

#### Importance of the liquidus and the temperature accuracy

The significance of growth rates does not lie entirely on the accuracy of time and length measurements; it also depends on the accurate reading of the environmental conditions. In our experiments, we estimated the uncertainty on the undercooling to be ±8.6°C, which may lead to some misevaluations. This is because the range of growth velocities can increase several times over a temperature range of 20°C (i.e. roughly  $2\sigma$ ), especially in the first ~50°C of undercooling, where the increase in growth velocity is steep (Fig. 11). Given that the uncertainty on the liquidus and the ambient temperature of crystallization has seldom been documented in the literature, this is another limit to the pertinence of reported growth rates. In the case of indirect growth rate determinations that provide little to no information on these parameters (such CSD studies, and diffusion and/or chemical modeling), a range of undercoolings may be estimated from the crystal habit (Appendix B) based on results of dynamic crystallization experiments (Donaldson, 1976; Faure et al., 2003a; Figs 1–3 and 5).

#### Importance of the cooling rate

The extremely fast cooling rate of 7800°C/h used in our experiments has shown that olivine suffers no significant delay when adjusting to new environmental conditions (Figs 2 and 3). We emphasize that the cooling rate plays a critical role since it controls how fast the undercooling, hence the supersaturation, increases in the melt, and how they drive the crystallization kinetics. For the fast interfaces such as {101} a given cooling ramp will guide crystallization along the curve of maximum velocities in the growth rate versus undercooling space (Figs 10-11). In general, fast cooling rates limit crystallization at low undercoolings, which allows buildup of high levels of supersaturation in the melt, yielding high growth velocities at high undercoolings. In contrast, low cooling rates will tend to lower the growth velocities. This is because the supersaturation does not increase rapidly and is instead consumed by melt crystallization and differentiation as the system sojourns at low undercoolings over a protracted period of time. Low cooling rates will hence keep growth rates under the curve of maximum growth velocities in spite of large (nominal) undercoolings. This may explain in part why some of the previous experiments performed at low or moderate cooling rates have found relatively low growth rates. Unless crystal growth is limited early by the cooling rate and/or local factors (such as physical obstacles), the growth rates at each interface on a given crystal will vary with time from G = 0 up to  $G_{max}^{(hkl)}$  and ultimately down to G = 0 again. While our fast cooling rates may be faster than the ones that occur in many natural systems, they approach the values of growth velocities that occur shortly after nucleation at

a temperature plateau, and before the melt chemistry changes in a significant manner. Such high cooling rates allow the seeds to approach a state that is close to a nucleation event at a given undercooling, where the amount of olivine is minimal and the supersaturation in the melt is at its highest at the onset of crystal growth (Appendix A1). In these conditions, the seeds can grow at the target undercooling almost as if they had formed spontaneously from the melt.

#### Applications of growth rates

The growth velocities measured in this study are among the fastest reported for similar undercoolings (Fig. 11). The fact that many of the previous values are lower than ours may be a consequence of the general difficulty in characterizing crystallization kinetics when many variables are at play. In theory, growth velocities must be primarily controlled by the chemical composition of the melt, and higher values would occur in low viscosity, high temperature, MgO-rich melts, as inferred by previous results (Donaldson, 1979; Faure et al., 2007; Sossi & O'Neill, 2016; Fig. 11). This is because the chemical composition of the melt sets the liquidus, and hence the ranges of temperature, viscosity, and diffusion rates at which the mineral can crystallize. Melts with similar chemical compositions should have overlapping curves of maximum growth velocities in the growth rates versus undercooling space. And melts with different chemical compositions should appear as distinct curves but with a similar shape, such that high temperature komatiite Mg-rich olivine would crystallize faster than low temperature tholeiite Mg-poor olivine at the same undercooling. The second most important parameter is the supersaturation in the melt, which is driven by the undercooling (Figs 10-11). Any uncertainty in growth rates translates to the applications of those rates. And because of the variable uncertainty inherent to each dataset, it is not yet possible to determine quantitatively the effect of the melt composition on olivine growth velocities.

Given that our experiments were performed in a tholeiitic melt at low to moderate temperatures (1044–1173  $\pm$  7°C; Table 2), the conservative approach would be to consider that our growth velocities are appropriate only for melts of similar chemical composition over a similar range of temperatures. We stress that any value of growth rate is highly contextual since they are influenced by many local factors, and most of these factors will tend to lower the growth rates (Appendix A). Our experiments allowed elimination or minimization of several of these factors (e.g. by isolating the low to null growth rates that occur during periods of acceleration, deceleration, and near-equilibrium) in order to approach precision measurements of the true maximum growth velocities of olivine. These true maximum growth velocities are not only critical to assess the true potential of olivine to crystallize from a given melt, but also to provide minimum timescales of magma crystallization. Here, our results provide additional evidence that olivine crystallizing from a basaltic melt can reach the grain sizes of microcrysts (< 100  $\mu$ m), mesocrysts (100–500  $\mu$ m) and macrocrysts (500  $\mu$ m – 10 mm; Welsch et al., 2009; Zellmer, 2021) within 30 minutes at moderate and low undercoolings, and within a few minutes at high undercoolings, as long as maximum, linear growth is maintained (Fig. 2). Additionally, our results indicate that olivine can reach these high growth velocities at slightly lower undercoolings than previously estimated (Fig. 11).

#### **Implications**

Growth rate accuracy is critical in many ways because it affects our understanding of crystal growth morphology, how we interpret rates and patterns of element uptake in a crystal, the moving boundary conditions for diffusion modeling, our general understanding of magmatic process timescales, and more. Misevaluation of growth rates will hence propagate into each of these areas of petrogenetic interest. Time-averaged growth rates encompass all variations in growth rate, thereby reducing the meaningful complexity of an ever-changing system ( $-\Delta T$ , impingement, convection, fO<sub>2</sub>, liquid evolution, etc.) to a single average value.

In the case of crystallization timescales of magmas, CSD studies have long used specific ranges of olivine growth rates assuming long residence times as periods of individual crystal growth (e.g. 100 days in Jerram et al., 2003, up to 14.5 years in Mangan, 1990). These mean growth rates are projected to be  $\sim 10^{-12}$  m/s for a broad range of rock compositions (Marsh, 1988; Resmini & Marsh, 1995),  $\sim$ 6 × 10<sup>-12</sup> m/s for komatiites of Canada, Australia, Finland, and Zimbabwe (Jerram et al., 2003),  $3.9-5.3 \times 10^{-11}$  m/s for lunar meteorites (Day & Taylor, 2007), and  $1.5-2.7 \times 10^{-10}$  m/s,  $10^{-11}$  m/s, and  $5.4 \times 10^{-10}$  –  $5 \times 10^{-12}$  m/s for various shergottites (Lentz & McSween, 2005; Usui et al., 2008; Ennis & McSween, 2014). These extremely low values of growth rates are inconsistent with the textures and chemical zoning of rapid crystal growth that have been documented in a wide range of terrestrial and extraterrestrial olivine-bearing rocks (Milman-Barris et al., 2008; Welsch et al., 2013, 2014; First & Hammer, 2016; Salas et al., 2021). However, these low growth rates overlap with the results of Nakamura (1995), Park & Hanson (1999) and Cabane et al. (2005), which suggests that they could correspond to crystallization processes occurring at extremely low cooling rates and/or extremely small undercoolings. They could be consistent with the late stages of deceleration and re-equilibration, after the crystals have built most of their final grain size at fast rates. If so, the drop in growth rates would be of several orders of magnitude between the early stages of olivine crystallization ( $10^{-9} - 10^{-6}$  m/s) and the later stages ( $10^{-16} - 10^{-10}$  m/s; Fig. 11; Supplementary Material B). Put together in a simple scenario of a hot, fresh, MgO-rich magma transported into the cold parts of a magma reservoir (e.g. Welsch et al., 2013), fast cooling rates (> 47°C/h in a simple system, Faure et al., 2003a) prevent nucleation at low undercoolings. Nuclei appearing later at higher undercoolings can then reach the maximum growth velocities allowed by the melt composition. As the crystals grow and gradually deplete the melt in olivine components, both the supersaturation and the growth velocities decrease. Crystals in close proximity also interact with each other, which limits their mutual development. A consequence is that a given crystal can experience all the range of growth rates over the course of its life, but spread over different amounts of time. Another implication is that, for a given crystallization event, a crystal can attain large dimensions that are close to the final state within its first instants of crystal growth. In the hypothesis that multiple nucleation events occur within a reservoir over a short period of time, magma can produce thick crystal mushes at very fast rates as long as each individual germ can quickly claim its space in the melt through crystal growth (Figs 2-5). On the other hand, the lower growth rates developed later during protracted periods of time may account for a smaller portion of the final dimensions of crystals. If many olivine-bearing rocks follow such a model, then our experiments show how critical it is to consider both maximum growth velocities and growth rate variations when determining the timescale of magma crystallization.

#### CONCLUSIONS

Our in situ study of olivine crystal growth from a basaltic melt reveals several fundamental aspects of crystallization kinetics:

- 1) Growth rates are highly contextual. They increase with the undercooling but they are also limited by the melt composition, the cooling rate and a multitude of local factors.
- 2) Up to three stages of crystal growth can occur during a single-step cooling: a first stage at accelerating growth rates, a second stage at maximum, linear growth rate, and a third stage at declining growth rates.
- 3) The stage at a maximum, linear growth rate needs to be isolated from other periods of slower or non-growth for proper measurements. In many cases, its true duration is overestimated.
- 4) A long crystal dimension is foreshortened in a 2D projection when it is not perfectly aligned with the plane of observation. Additional deviations from the true crystal dimension can occur when the crystal is truncated through thin section preparation and polishing. In many cases, the true dimensions of crystals are underestimated.
- 5) Because of (3) and (4), growth rates calculated as crystal half-lengths divided by crystallization duration are usually underestimations of the true maximum growth velocities. As a consequence, the calculated values should generally be considered as lower bounds.
- 6) The uncertainty on the growth rates must be addressed in conjunction with the methods used. The distinction between the measurement of a linear growth rate with a direct method, and the estimation of a mean growth rate with an indirect method is critical. The difference between a growth rate and a growth velocity, i.e. how the value relates to a specific interface, matters, especially when the mineral shows strong shape and growth anisotropies.
- 7) Using a heating stage microscope at maximum cooling rates of 7800°C/h eliminated several variables and assumptions on the timing and fashion of crystal growth, and approached precision measurements of the true maximum growth velocities of specific olivine interfaces {hkl}. We found that the method is primarily limited by the uncertainty on the liquidus and the run temperatures, and to a lesser extent, by the orientation of crystals with respect to the projection plane. Although our experimental set up tracked olivine crystallization kinetics up close, the growth velocities during the acceleration and the deceleration stages remain difficult to quantify accurately. In general, the speed of an interface measured with our technique accounts for more than half of the true growth velocity as long as the crystal is reasonably aligned with the plane of observation ( $\alpha \leq 60^{\circ}$ ). The linear, maximum growth velocities  $G_{linear}^{(hkl)}$  measured here at 2.1  $\times$  $10^{-8} - 4.8 \times 10^{-7}$  m/s,  $1.9 - 7.6 \times 10^{-8}$  m/s,  $4.5 \times 10^{-9} - 7.6$  $\times$  10<sup>-8</sup> m/s, and less than 2.4  $\times$  10<sup>-8</sup> m/s, for the interfaces {101}, {100}, {001}, and {010} respectively, at undercoolings ranging from 19°C to 129°C, may account for the early stages of crystallization of olivine microlites, microphenocrysts and phenocrysts in low MgO basaltic melts.

#### ACKNOWLEDGMENTS

We are grateful to Roberto Clocchiatti and Dominique Massare for their mentoring with the heating stage microscope, to Pierre Schiano and Nicole Métrich for their help with the samples, to Brian Monteleone for the SIMS analyses at Woods Hole Oceanographic Institution (WHOI), to Joe Bosenberg and Danny Anderson for the microprobe analyses at Brown University, and to Eric Dowty for his help with the SHAPE software. We thank Malcolm Rutherford, Yan Liang, and Stephen Parman at Brown University,

and Megan Holycross and Esteban Gazel at Cornell University, for their support. This manuscript was improved thanks to the careful examination provided by two anonymous reviewers, editor Takashi Mikouchi, and executive editor Georg Zellmer.

#### SUPPLEMENTARY DATA

Supplementary data are available at Journal of Petrology online.

#### CONFLICT OF INTEREST

The authors declare no conflicts of interest.

#### **FUNDING**

BW was sponsored by National Science Foundation (NSF) through awards #1650416 and #1902278. FF was supported by the TelluS Program of CNRS/INSU and by the Programme National de Planétologie: PNP-INSU. ECF is grateful to support from the Heising-Simons foundation via a 51 Pegasi b Fellowship. This is CRPG contribution No. 2844.

#### References

- Albarède, F. & Bottinga, Y. (1972). Kinetic disequilibrium in trace element partitioning between phenocrysts and host lava. Geochimica et Cosmochimica Acta 36, 141-156. https://doi. org/10.1016/0016-7037(72)90003-8.
- Allard, P. (1980). Caractéristiques géochimiques des volatils émis par l'éruption volcanique de novembre 1978 dans le rift d'Asal. Bulletin de la Société Géologique de France S7-XXII, 825-830. https:// doi.org/10.2113/gssgfbull.S7-XXII.6.825.
- Allard, P., Tazieff, H. & Dajlevic, D. (1979). Observations of seafloor spreading in Afar during the November 1978 fissure eruption. Nature 279(5708), 30-33. https://doi.org/10.1038/279030a0.
- Armienti, P. (2008). Decryption of igneous rock textures: crystal size distribution tools. Reviews in Mineralogy and Geochemistry 69(1), 623-649. https://doi.org/10.2138/rmg.2008.69.16.
- Armienti, P., Innocenti, F., Pareschi, M. T., Pompilio, M. & Rocchi, S. (1991). Crystal population density in not stationary volcanic systems: estimate of olivine growth rate in basalts of Lanzarote (Canary Islands). Mineralogy and Petrology 44(3-4), 181-196. https://doi.org/10.1007/BF01166962.
- Armienti, P., Pareschi, M. T., Innocenti, F. & Pompilio, M. (1994). Effects of magma storage and ascent on the kinetics of crystal growth. Contributions to Mineralogy and Petrology 115(4), 402-414. https:// doi.org/10.1007/BF00320974.
- Barrabé, L. & Deicha, G. (1956). Expériences de fusion et de cristallisation magmatique Sur des reliquats vitreux des quartz dihexaédriques de la Guadeloupe. Bulletin de la Societe Française de Mineralogie et de Cristallographie 79(1-3), 146-155. https://doi.org/10.3406/ bulmi.1956.5055.
- Barrabé, L. & Deicha, G. (1957). Réanimation des magmas et interprétation de quelques particularités de leurs éléments de première consolidation. Bulletin de la Société Géologique de France S6-VII, 159-169. https://doi.org/10.2113/gssgfbull.S6-VII.1-3.159.
- Barrabé, L., Collomb, P. & Deicha, G. (1957). Utilisation des sphères polies dans les recherches sur les reliquats magmatiques. Bulletin de la Societe Française de Mineralogie et de Cristallographie 80(10-12), 450-452. https://doi.org/10.3406/bulmi.1957.5195.
- Barrabé, L., Collomb, P. & Deicha, G. (1959). Libération éruptive de magma réanimé sous le microscope de chauffe. Bulletin de la Societe Francaise de Mineralogie et de Cristallographie 82(4–6), 163–165. https://doi.org/10.3406/bulmi.1959.5323.

- Bizouard, H., Clocchiatti, R. & Marinelli, G. (1980). Les tholéites à olivine à mégacristaux de bytownite du rift d'Asal (Rép. de Djibouti). Quelques suggestions pour un module génétique. Bulletin de la Société Géologique de France S7-XXII, 845-850. https://doi. org/10.2113/gssgfbull.S7-XXII.6.845.
- Bouvet de Maisonneuve, C., Costa, F., Huber, C., Vonlanthen, P., Bachmann, O. & Dungan, M. A. (2016). How do olivines record magmatic events? Insights from major and trace element zoning. Contributions to Mineralogy and Petrology 171(6), 1-20. https://doi. org/10.1007/s00410-016-1264-6.
- Brattgård, S.-O. (1954). Microscopical determinations of the thickness of histological sections. Journal of the Royal Microscopical Society 74(2), 113-122. https://doi.org/10.1111/j.1365-2818.1954. tb02009.x.
- Bravais, A. (1848). Sur les propriétés géométriques des assemblages de points régulièrement distribués dans l'espace. Comptes Rendus de l'Académie des Sciences 27. 601–604.
- Bucholz, C. E., Gaetani, G. A., Behn, M. D. & Shimizu, N. (2013). Post-entrapment modification of volatiles and oxygen fugacity in olivine-hosted melt inclusions. Earth and Planetary Science Letters 374, 145-155. https://doi.org/10.1016/j.epsl.2013.05.033.
- Cabane, H., Laporte, D. & Provost, A. (2005). An experimental study of Ostwald ripening of olivine and plagioclase in silicate melts: implications for the growth and size of crystals in magmas. Contributions to Mineralogy and Petrology 150(1), 37–53. https://doi. org/10.1007/s00410-005-0002-2.
- Chen, Y., Provost, A., Schiano, P. & Cluzel, N. (2011). The rate of water loss from olivine-hosted melt inclusions. Contributions to Mineralogy and Petrology 162(3), 625-636. https://doi.org/10.1007/ s00410-011-0616-5.
- Clocchiatti, R. (1977a). Les inclusions vitreuses des phénocristaux d'olivine et de chromite d'un «basalte picritique» de la ride médio-Atlantique: témoins de la contamination mécanique d'un basalte à olivine. Comptes rendus de l'Académie des Sciences, série D
- Clocchiatti, R. (1977b). Les silicates bloqués dans les cristaux d'olivine, de plagioclase et de pyroxène, prises d'essai du magma: application à un basalte à affinité tholéïtique de la ride océanique émergée d'Asal (T.F.a.I.). Comptes rendus de l'Académie des Sciences, série D 284, 2203.
- Clocchiatti, R. & Massare, D. (1985). Experimental crystal growth in glass inclusions: the possibilities and limits of the method. Contributions to Mineralogy and Petrology 89(2-3), 193-204. https:// doi.org/10.1007/BF00379453.
- Clocchiatti, R., Havette Ledebt, A., Weiss, J. & Wilhelm, S. (1978). Les bytownites du Rift d'Asal. Première partie : étude des verres basaltiques inclus dans les mégacristaux: nouvelle approche pour la connaissance de certains processus pétrogénétiques. Bulletin de Minéralogie 101(1), 66-76.
- Colin, A., Faure, F. & Burnard, P. (2012). Timescales of convection in magma chambers below the mid-Atlantic ridge from melt inclusions investigations. Contributions to Mineralogy and Petrology 164(4), 677-691. https://doi.org/10.1007/ s00410-012-0764-2.
- Danyushevsky, L. V., McNeill, A. W. & Sobolev, A. V. (2002). Experimental and petrological studies of melt inclusions in phenocrysts from mantle-derived magmas: an overview of techniques, advantages and complications. Chemical Geology 183(1), 5-24. https:// doi.org/10.1016/S0009-2541(01)00369-2.
- Day, J. M. D. & Taylor, L. A. (2007). On the structure of mare basalt lava flows from textural analysis of the LaPaz Icefield and Northwest Africa 032 lunar meteorites. Meteoritics and Planetary Science 42(1), 3-17. https://doi.org/10.1111/j.1945-5100.2007.tb00213.x.

- Deer, W. A., Howie, R. A. & Zussman, J. (1982) Rock Forming Minerals, 2nd edn. Orthosilicates, 1A. London: Geological Society.
- Devineau, K., Champallier, R. & Pichavant, M. (2020). Dynamic crystallization of a haplogranitic melt: application to pegmatites. Journal of Petrology 61(5). https://doi.org/10.1093/petrology/ egaa054.
- Di Muro, A., Métrich, N., Vergani, D., Rosi, M., Armienti, P., Fougeroux, T., Deloule, E., Arienzo, I. & Civetta, L. (2014). The shallow plumbing system of piton de la Fournaise volcano (La Réunion island, Indian Ocean) revealed by the major 2007 caldera-forming eruption. Journal of Petrology **55**(7), 1287–1315. https://doi.org/10.1093/ petrology/egu025.
- Dolgov, Y. A. & Bazarov, L. S. (1965) A chamber for investigating inclusions of mineral-forming solutions and melts at high temperatures. In: Mineralogicheskaya Termometriya i Barometriya, Vol. 2. Moscow: Nauka Press, pp.64-69.
- Donaldson, C. H. (1975). Calculated diffusion coefficients and the growth rate of olivine in a basalt magma. Lithos 8(2), 163-174. https://doi.org/10.1016/0024-4937(75)90023-7.
- Donaldson, C. H. (1976). An experimental investigation of olivine morphology. Contributions to Mineralogy and Petrology 57(2), 187-213. https://doi.org/10.1007/BF00405225.
- Donaldson, C. H. (1977). Laboratory duplication of comb layering in the Rhum pluton. Mineralogical Magazine 41 (September), 323-336. https://doi.org/10.1180/minmag.1977.041.319.03.
- Donaldson, C. H. (1979). An experimental investigation of the delay in nucleation of olivine in mafic magmas. Contributions to Mineralogy and Petrology 69(1), 21-32. https://doi.org/10.1007/ BF00375191.
- Donnay, J. D. H. & Harker, D. (1937). A new law of crystal morphology extending the Law of Bravais. American Mineralogist 22(5), 446-467.
- Dowty, E. (1980). Computing and drawing crystal shapes. American Mineralogist 65(5-6), 465-471.
- Dowty, E. (1987) SHAPE Copyright 1994, Shape Software 521 Hidden Valley Road, Kingsport, TN 37663 USA; http://www. shapesoftware.com.
- Duan, Z. & Zhang, Z. (2006). Equation of state of the H2O, CO2, and H2O-CO2 systems up to 10 GPa and 2573.15K: molecular dynamics simulations with ab initio potential surface. Geochimica et Cosmochimica Acta 70(9), 2311-2324. https://doi.org/10.1016/j. gca.2006.02.009.
- Eberl, D. D., Kile, D. E. & Drits, V. A. (2002). On geological interpretations of crystal size distributions: constant vs. proportionate growth. American Mineralogist 87(8-9), 1235-1241. https://doi. org/10.2138/am-2002-8-923.
- Ennis, M. E. & McSween, H. Y. J. (2014). Crystallization kinetics of olivine-phyric shergottites. Meteoritics & Planetary Science 49(8), 1440-1455. https://doi.org/10.1111/maps.12349.
- Faure, F. & Schiano, P. (2004). Crystal morphologies in pillow basalts: implications for mid-ocean ridge processes. Earth and Planetary Science Letters 220(3-4), 331-344. https://doi.org/10.1016/ S0012-821X(04)00057-3.
- Faure, F., Trolliard, G., Nicollet, C. & Montel, J.-M. (2003a). A developmental model of olivine morphology as a function of the cooling rate and the degree of undercooling. Contributions to Mineralogy and Petrology 145(2), 251-263. https://doi.org/10.1007/ s00410-003-0449-y.
- Faure, F., Trolliard, G. & Soulestin, B. (2003b). TEM investigation of forsterite dendrites. American Mineralogist 88(8-9), 1241-1250. https://doi.org/10.2138/am-2003-8-907.
- Faure, F., Arndt, N. & Libourel, G. (2006). Formation of spinifex texture in komatiites: an experimental study. Journal of Petrology 47(8), 1591-1610. https://doi.org/10.1093/petrology/egl021.

- Faure, F., Schiano, P., Trolliard, G., Nicollet, C. & Soulestin, B. (2007). Textural evolution of polyhedral olivine experiencing rapid cooling rates. Contributions to Mineralogy and Petrology 153(4), 405–416. https://doi.org/10.1007/s00410-006-0154-8.
- First, E. & Hammer, J. (2016). Igneous cooling history of olivine-phyric shergottite Yamato 980459 constrained by dynamic crystallization experiments. Meteoritics & Planetary Science 51, 1233–1255. https://doi.org/10.1111/maps.12659.
- First, E. C., Leonhardi, T. C. & Hammer, J. E. (2020). Effects of superheating magnitude on olivine growth. Contributions to Mineralogy and Petrology 175(2), 13. https://doi.org/10.1007/ s00410-019-1638-7.
- Fowler, A. D., Stanley, H. E. & Daccord, G. (1989). Disequilibrium silicate mineral textures: fractal and non-fractal features. Nature 341(6238), 134-138. https://doi.org/10.1038/341134a0.
- Friedel, G. (1911) Leçons de cristallographie. Paris: A. Hermann, p.310. Gaetani, G. A., O'Leary, J. A., Shimizu, N., Bucholz, C. E. & Newville, M. (2012). Rapid reequilibration of H<sub>2</sub>O and oxygen fugacity in olivine-hosted melt inclusions. Geology 40(10), 915-918. https:// doi.org/10.1130/G32992.1.
- Galbraith, W. (1955). The optical measurement of depth. Quarterly Journal of Microscopical Science (London) s3-96(35), 285-288. https:// doi.org/10.1242/jcs.s3-96.35.285.
- Ghiorso, M. S. & Gualda, G. A. R. (2015). An H<sub>2</sub>O-CO<sub>2</sub> mixed fluid saturation model compatible with rhyolite-MELTS. Contributions to Mineralogy and Petrology 169(53), 1–30. https://doi.org/10.1007/ s00410-015-1141-8.
- Ghiorso, M. S. & Sack, R. O. (1995). Chemical mass transfer in magmatic processes IV. A revised and internally consistent thermodynamic model for the interpolation and extrapolation of liquidsolid equilibria in magmatic systems at elevated temperatures and pressures. Contributions to Mineralogy and Petrology 119(2), 197-212. https://doi.org/10.1007/BF00307281.
- Gualda, G. A. R., Ghiorso, M. S., Lemons, R. V. & Carley, T. L. (2012). Rhyolite-MELTS: a modified calibration of MELTS optimized for silica-rich, fluid-bearing magmatic systems. Journal of Petrology 53(5), 875-890. https://doi.org/10.1093/petrology/egr080.
- Harris, R. M. (1985). Light microscopic depth measurements of thick sections. Journal of Neuroscience Methods 14(2), 97-100. https://doi. org/10.1016/0165-0270(85)90120-7.
- Hartman, P. & Perdok, W. G. (1955a). On the relations between structure and morphology of crystals. I. Acta Crystallographica 8(I), 49-52. https://doi.org/10.1107/S0365110X55000121.
- Hartman, P. & Perdok, W. G. (1955b). On the relations between structure and morphology of crystals. II. Acta Crystallographica 8(II), 521-524. https://doi.org/10.1107/S0365110X55001679.
- Hartman, P. & Perdok, W. G. (1955c). On the relations between structure and morphology of crystals. III. Acta Crystallographica 8(III), 525-529. https://doi.org/10.1107/S0365110X55001680.
- Hersum, T. G. & Marsh, B. D. (2006). Igneous microstructures from kinetic models of crystallization. Journal of Volcanology and Geothermal Research 154(1), 34-47. https://doi.org/10.1016/j. jvolgeores.2005.09.018.
- Heyart, H. (1955). Bulletin de la Société française de Minéralogie et de Cristallographie, 76(LVII).
- Jambon, A., Lussiez, P., Clocchiatti, R., Weisz, J. & Hernandez, J. (1992). Olivine growth rates in a tholeiitic basalt: an experimental study of melt inclusions in plagioclase. Chemical Geology 96, 277-287. https://doi.org/10.1016/0009-2541(92)90059-E.
- Jerram, D. A., Cheadle, M. J. & Philpotts, A. R. (2003). Quantifying the building blocks of igneous rocks: are clustered crystal frameworks the foundation? Journal of Petrology 44(11), 2033-2051. https://doi.org/10.1093/petrology/egg069.

- Kirkpatrick, R. J. (1975). Crystal growth from the melt: a review. American Mineralogist 60, 798-814.
- Kirkpatrick, R. J., Klein, L., Uhlmann, D. R. & Hays, J. F. (1979). Rates and processes of crystal growth in the system anorthite-albite. Journal of Geophysical Research 84(B7), 3671-3676. https://doi.org/10.1029/ JB084iB07p03671.
- Kirkpatrick, R. J., Kuo, L.-C. & Melchior, J. (1981). Crystal growth in incongruently-melting compositions: programmed cooling experiments with diopside. American Mineralogist 60, 223-241.
- Kornprobst, J., Boivin, P. & Bachèlery, P. (1979). L'alimentation des éruptions récentes du piton de la Fournaise (Ile de la Réunion, Océan Indien): Degré d'évolution et niveau de ségrégation des laves émises. Comptes Rendus de l'Académie des Sciences 288D(29), 1691-1694.
- Lang, S., Mollo, S., France, L., Misiti, V. & Nazzari, M. (2021). Kinetic partitioning of major-minor cations between olivine and Hawaiian tholeiitic basalt under variable undercooling and cooling rate conditions. Chemical Geology 584, 120485. https://doi.org/10.1016/ j.chemgeo.2021.120485.
- Laumonier, M., Laporte, D., Faure, F., Provost, A., Schiano, P. & Ito, K. (2019). An experimental study of dissolution and precipitation of forsterite in a thermal gradient: implications for cellular growth of olivine phenocrysts in basalt and melt inclusion formation. Contributions to Mineralogy and Petrology 174(11), 94. https://doi. org/10.1007/s00410-019-1627-x.
- Lentz, R. C. F. & McSween, H. Y. J. (2005). A textural examination of the Yamato 980459 and Los Angeles shergottites using crystal size distribution analysis. Antarctic Meteorite Research **18**, 66-82.
- Levoy, M., Ng, R., Adams, A., Footer, M. & Horowitz, M. (2006). Light field microscopy. ACM Transactions on Graphics 25(3), 924-934. https://doi.org/10.1145/1141911.1141976.
- Lewis, A., Seckler, M., Kramer, H., and van Rosmalen, G. (2015) Industrial Crystallization: Fundamentals and Applications. Cambridge University Press, Cambridge, https://doi.org/10.1017/ CBO9781107280427.
- Mangan, M. T. (1990). Crystal size distribution systematics and the determination of magma storage times: the 1959 eruption of Kilauea volcano, Hawaii. Journal of Volcanology and Geothermal Research 44(3), 295-302. https://doi.org/10.1016/0377-0273(90
- Marsh, B. D. (1988). Crystal size distributions (CSD) in rocks and the kinetics and dynamics of crystallization I. theory. Contributions to Mineralogy and Petrology 99, 277-291. https://doi.org/10.1007/
- Métrich, N. & Clocchiatti, R. (1996). Sulfur abundance and its speciation in oxidized alkaline melts. Geochimica et Cosmochimica Acta 60(21), 4151-4160. https://doi.org/10.1016/S0016-7037(96 )00229-3.
- Milman-Barris, M., Beckett, J., Baker, M., Hofmann, A., Morgan, Z., Crowley, M., Vielzeuf, D. & Stolper, E. (2008). Zoning of phosphorus in igneous olivine. Contributions to Mineralogy and Petrology 155(6), 739-765. https://doi.org/10.1007/s00410-007-0268-7.
- Mourey, A. J. & Shea, T. (2019). Forming olivine phenocrysts in basalt: a 3D characterization of growth rates in laboratory experiments. Frontiers in Earth Science 7, 1-16. https://doi.org/10.3389/ feart.2019.00300.
- Nakamura, M. (1995). Residence time and crystallization history of nickeliferous olivine phenocrysts from the northern Yatsugatake volcanoes, Central Japan: application of a growth and diffusion model in the system Mg-Fe-Ni. Journal of Volcanology and Geothermal Research 66(1), 81-100. https://doi.org/10.1016/0377-0273(94 )00054-K.

- Ni, H., Keppler, H., Walte, N., Schiavi, F., Chen, Y., Masotta, M. & Li, Z. (2014). In situ observation of crystal growth in a basalt melt and the development of crystal size distribution in igneous rocks. Contributions to Mineralogy and Petrology 167(5), 1–13. https://doi. org/10.1007/s00410-014-1003-9.
- Park, Y. & Hanson, B. (1999). Experimental investigation of Ostwaldripening rates of forsterite in the haplobasaltic system. Journal of Volcanology and Geothermal Research 90(1), 103-113. https://doi. org/10.1016/S0377-0273(99)00023-2.
- Portnyagin, M., Almeev, R., Matveev, S. & Holtz, F. (2008). Experimental evidence for rapid water exchange between melt inclusions in olivine and host magma. Earth and Planetary Science Letters 272(3-4), 541-552. https://doi.org/10.1016/j.epsl.2008.05.020.
- Resmini, R. G. & Marsh, B. D. (1995). Steady-state volcanism, paleoeffusion rates, and magma system volume inferred from plagioclase crystal size distributions in mafic lavas: Dome Mountain, Nevada. Journal of Volcanology and Geothermal Research 68(4), 273-296. https://doi.org/10.1016/0377-0273(95)00003-5.
- Richardson, J.F., Harker, J.H., and Backhurst, J.R. (2002) Chapter 15: Crystallisation. In J.F. Richardson, J.H. Harker, and J.R. Backhurst, Eds. Chemical Engineering (5th edn.), pp. 827-900. Butterworth-Heinemann, Oxford, https://doi.org/10.1016/ B978-0-08-049064-9.50026-6.
- Roedder, E. (1965). Liquid CO2 inclusions in olivine-bearing nodules and phenocrysts from basalts. American Mineralogist 50,
- Roedder, E. (1979). Origin and significance of magmatic inclusions. Bulletin de Minéralogie 102, 487-510. https://doi.org/10.3406/ bulmi.1979.7299.
- Roedder, E. (1984) Fluid inclusions. 644 p. Mineralogical Society of America, Washington, DC, https://doi.org/10.1515/9781501508271.
- Rusiecka, M. K., Bilodeau, M. & Baker, D. R. (2020). Quantification of nucleation delay in magmatic systems: experimental and theoretical approach. Contributions to Mineralogy and Petrology 175(5), 47. https://doi.org/10.1007/s00410-020-01682-4.
- Salas, P., Ruprecht, P., Hernández, L. & Rabbia, O. (2021). Outof-sequence skeletal growth causing oscillatory zoning in arc olivines. Nature Communications 12(1), 4069. https://doi. org/10.1038/s41467-021-24275-6.
- Sato, K., Kazuhiro, K. & Sunagawa, I. (1981). Measurements of nucleation rates and real growth rates of plagioclase. Journal of the Japanese Association of Mineralogists, Petrologists and Economic Geologists 76, 294-307. https://doi.org/10.2465/ganko1941.76.294.
- Schiano, P., Provost, A., Clocchiatti, R. & Faure, F. (2006). Transcrystalline melt migration and Earth's mantle. Science 314(5801), 970-974. https://doi.org/10.1126/science.1132485.
- Schmidt, M. B. (1959). On the history, development, and application of the warm stage. Journal of the Royal Microscopical Society 79(2), 119-124. https://doi.org/10.1111/j.1365-2818.1959.tb04460.x.
- Sirbescu, M.-L. C., Schmidt, C., Veksler, I. V., Whittington, A. G. & Wilke, M. (2017). Experimental crystallization of undercooled felsic liquids: generation of pegmatitic texture. Journal of Petrology 58(3), 539-568. https://doi.org/10.1093/petrology/egx027.
- Sobolev, A. V., Dmitriev, L. V., Barsukov, V. L., Nevsorov, V. N. & Slutskii, A. B. (1980). The formation conditions of the high-magnesium olivines from the monomineralic fraction of Luna 24 regolith. Proceedings of the 11th Lunar Science Conference 1, 105–116.
- Sobolev, A., Clocchiatti, R. & Dhamelincourt, P. (1983). Les variations de la température, de la composition du magma et l'estimation de la pression partielle d'eau pendant la cristallisation de l'olivine dans les océanites du Piton de la Fournaise (Réunion, éruption de 1966). Comptes Rendus de l'Académie des Sciences II(296), 275-280.

- Sorby, H. C. (1858). On the microscopical, structure of crystals, indicating the origin of minerals and rocks. Geological Society of London Quarterly Journal 14(1–2), 453–500. https://doi.org/10.1144/GSL.JGS.1858.014.01-02.44.
- Sossi, P. A. & O'Neill, H. S. C. (2016). Liquidus temperatures of komatiites and the effect of cooling rate on element partitioning between olivine and komatiitic melt. Contributions to Mineralogy and Petrology 171(5), 49. https://doi.org/10.1007/ s00410-016-1260-x.
- Sunagawa, I. (1957). Variation in crystal habit of pyrite. *Geological Survey of Japan* **175**, 42p. + 10 pl. p.
- Sunagawa, I. (1981). Characteristics of crystal growth in nature as seen from the morphology of mineral crystals. *Bulletin de Minéralogie* **104**, 81–87. https://doi.org/10.3406/bulmi.1981.7438.
- Usui, T., McSween, H. Y. & Floss, C. (2008). Petrogenesis of olivine-phyric shergottite Yamato 980459, revisited. Geochimica et Cosmochimica Acta 72(6), 1711–1730. https://doi.org/10.1016/j. gca.2008.01.011.
- Vinet, N. & Higgins, M. D. (2010). Magma solidification processes beneath Kilauea volcano, Hawaii: a quantitative textural and geochemical study of the 1969–1974 Mauna Ulu lavas. *Journal of Petrology* **51**(6), 1297–1332. https://doi.org/10.1093/petrology/egq020.
- Vinet, N. & Higgins, M. D. (2011). What can crystal size distributions and olivine compositions tell us about magma solidification processes inside Kilauea Iki lava lake, Hawaii? *Journal of Volcanology* and Geothermal Research 208(3), 136–162. https://doi.org/10.1016/j. jvolgeores.2011.09.006.

- Weinbruch, S., Styrsa, V. & M, ller, W.F. (2003). Exsolution and coarsening in iron-free clinopyroxene during isothermal annealing. Geochimica et Cosmochimica Acta 67(24), 5071–5082. https://doi.org/10.1016/S0016-7037(03)00205-9.
- Welsch, B., Faure, F., Bachèlery, P. & Famin, V. (2009). Microcrysts record transient convection at Piton de la Fournaise volcano (La Reunion hotspot). *Journal of Petrology* 50(12), 2287–2305. https://doi.org/10.1093/petrology/egp076.
- Welsch, B., Faure, F., Famin, V., Baronnet, A. & Bachèlery, P. (2013). Dendritic crystallization: a single process for all the textures of olivine in basalts? *Journal of Petrology* **54**(3), 539–574. https://doi.org/10.1093/petrology/egs077.
- Welsch, B., Hammer, J. E. & Hellebrand, E. (2014). Phosphorus reveals dendritic architecture of olivine. Geology 42(10), 867–870. https:// doi.org/10.1130/G35691.1.
- Yermakov, N. P. (1950) Issledovaniya mineraloobrazuyushchikh rastvorov. Moscow, USSR: Khar'kov Univ. Press, p.459.
- Zapunnyy, S. A., Sobolev, V. S., Bogdanov, A. A., Slutskiy, L. V., Dmitriyev, L. V. & Kunin, L. L. (1988). An apparatus for hightemperature optical research with controlled fugacity. *Geokhimiya* 7, 1044–1052.
- Zellmer, G. F. (2021). Gaining acuity on crystal terminology in volcanic rocks. Bulletin of Volcanology **83**(11), 78. https://doi.org/10.1007/s00445-021-01505-9.
- Zieg, M. J. & Lofgren, G. E. (2006). An experimental investigation of texture evolution during continuous cooling. *Journal of Volcanology and Geothermal Research* **154**(1–2), 74–88. https://doi.org/10.1016/j. jvolgeores.2005.09.020.

# REAPPRAISING CRYSTALLIZATION KINETICS WITH OVERGROWTH CHRONOMETRY: AN IN SITU STUDY OF OLIVINE GROWTH VELOCITIES

### **APPENDICES A & B**

Benoît Welsch<sup>a\*</sup>, François Faure<sup>b</sup> & Emily First<sup>a</sup>

<sup>a</sup>Macalester College, Geology Department, 1600 Grand Avenue, Saint Paul, Minnesota 55105-1899, USA.

<sup>b</sup>Université de Lorraine, CNRS, CRPG, UMR 7358, 15 rue Notre Dame des Pauvres Vandoeuvre-Lès-Nancy, F-54501, France.

<sup>\*</sup>corresponding author: <u>bwelsch@macalester.edu</u>

#### **APPENDIX A: EXPERIMENTAL LIMITATIONS**

#### A1. Effect of the cooling rate

The fast cooling rates used here serve two main functions: to allow seeds that were heated above the liquidus to quickly reach some undercooling and thereby survive dissolution, and to minimize crystallization in between the liquidus and final isotherm. In doing so, most of the initial supersaturation is preserved before reaching the target temperature and maximum growth velocities can be attained. These conditions hence approximate an initial state in the melt that is similar to that of a nucleation event, where the amount of olivine is minimal at the target undercooling, and where the supersaturation is at its highest.

#### A2. Effect of the seeds

Because our experiments were seeded, the results cannot provide direct information on the nucleation of olivine from a silicate melt. However, this approach is appropriate and even advantageous for studying crystal growth. Five key considerations are addressed below.

First, preparing the melt inclusion with a single seed bypasses the problem of nucleation delay, eliminating the uncertainty on both the number of germs formed from the melt and the timing of their appearance. In particular, melt superheating prior to cooling produces variations in the subsequent crystallization processes that are attributed to delayed nucleation (Donaldson, 1979; First et al., 2020). The fact that our experiments were seeded suggests that these variations were prevented, more so because the cooling ramps were initiated at the presumed liquidus temperature or below ( $T_{\text{start}} \leq 1173\,^{\circ}\text{C}$ ; Table 2). The presence of a single germ allows free crystal growth until reaching relatively large grain sizes, without the influence of other olivine grains. Any potential changes in growth rate or texture due to competitive crystallization between adjacent crystals are eliminated.

Second, using an olivine seed and rapid cooling prevents clinopyroxene, normally the liquidus phase with plagioclase, from crystallizing. The seeds were initially metastable, as they fluctuated between growing in the zone just underneath the liquidus or dissolving above it (Table 2). The seeds also experienced fast cooling rates at the beginning of the experiments, which left limited time for their crystal growth at low undercoolings. Similar to the processes described in Faure (2020) and Faure and Tissandier (2014), the crystallization of olivine was also metastable because the melt was not allowed to crystallize clinopyroxene (the second phase to crystallize after plagioclase and before olivine; Clocchiatti and Massare, 1985; Jambon et al., 1992), since clinopyroxene germs were eliminated and hence prevented to crystallize during the sample preparation.

Third, because the olivine seeds were directly formed inside the melt inclusion and were not added from the outside, the initial supersaturation of the melt was decreased to accomplish their crystallization. However, the size of the seeds is small (diameter  $\emptyset = 2 - 16 \mu m$ , Table 2) in comparison to that of the melt inclusion (105 x 203 x 64  $\mu m$ ) and that of the final crystals (80 – 160  $\mu m$  long, Figs 2 – 5, Table 2), which suggests that their crystallization causes only a trivial decrease in the olivine liquidus at the onset of the cooling ramp.

Fourth, the apparent lack of significant growth in the first 10 s of cooling is expected, since at our cooling ramp ( $\sim$ 2.2 °C/s), 10 s spans from the liquidus down to only 22 °C of undercooling, where growth rates are still relatively slow. With  $G_{linear} \leq 10^{-8}$  m/s, the  $\sim$ 0.1  $\mu$ m thick overgrowths that could form within 10 s of cooling are beneath the resolution of our images.

Fifth and finally, bypassing of the nucleation stage suggests that, in theory, seeded crystals should develop thicker overgrowths than unseeded crystals at the same conditions of crystallization, given that their period of crystal growth is longer (there is no lag in nucleation and crystal growth). This is however not the case since a seed has a larger surface energy than a nucleus, which can drain more quickly the undercooling at the interface. In the experiments

of Zieg and Lofgren (2006), the seeds only grow into small polyhedral grains and settled to the bottom of the charges while the crystals formed later and spontaneously from the melt are larger and skeletal. In the experiments of Faure et al. (2007), the seeds develop overgrowths that are similar in thickness and texture to the dendritic crystals formed spontaneously from the melt. In our experiments and Jambon et al. (1992)'s, there is also no evidence that the seeds influenced the crystal growth of olivine in a significant way. The overgrowths are comparatively much larger than the seeds they grew on: our final crystals are 14 to 80 µm in their smallest dimensions while their seeds were 2 to 16  $\mu$ m (Figs 2 – 5). Our crystals follow the same morphological breakdown (tabular > skeletal > dendritic) as crystals formed in unseeded experiments at similar undercoolings (Donaldson, 1976; Faure et al., 2003a). Their specific habits are also similar to those formed spontaneously from the melt, in spite of the morphological differences between the seeds (stubby at 38 and 129 °C of undercooling, and elongated at 19, 57, 77 and 96 °C; Fig. 2). These observations suggest that the surface energy penalty imposed by our small seeds was similar to that for a nucleus formed spontaneously from the melt. This is reinforced by the fact that the driving force exerted in our experiments is relatively high ( $-\Delta T \ge 19$  °C), which forces a relatively large amount of material to be deposited over a single, small germ. For comparison, other processes of crystal growth were observed using seeds of similar grain sizes at very low undercoolings (Cabane et al., 2005; Park and Hanson, 1999).

#### A3. Effect of foreign objects in the melt

The crystallization environment of our experimental set up is defined by a finite reservoir of silicate melt containing a single olivine seed and a large vapor bubble, and limited by plagioclase walls that grow inward upon cooling. The fact that the crystals remained immobile for the majority of their growth suggests that the growth rates were not significantly influenced by hydrodynamics in the melt (Nývlt, 1984). The size of olivine crystals was nonetheless physically limited by the size of the melt inclusion, especially at moderate and high undercoolings where the crystals have the potential to reach larger dimensions. This constrained growth led to interruptions in the crystallization process and to incomplete crystal habits (Fig. 2). The vapor bubble acted as another obstacle in the melt (Fig. 2). Both of these physical limitations are pertinent to magma crystallization in nature. Growth rates may increase in proximity to crystallizing plagioclase, due to boundary layers enriched in rejected elements, which are also olivine components (Mg, Fe).

#### A4. Effect of chemical heterogeneities in the melt

By definition, the crystal growth of olivine depends on the liquidus and solidus curves, which are themselves set by the chemical composition of the melt. The melt inclusion in our experiments was not completely homogeneous, as the concentration of olivine components was higher both around the seeds (due to dissolution prior to cooling), and near the plagioclase walls (due to rejection of Mg and Fe during crystallization). At those two interfaces, the melt must have had a slightly higher olivine liquidus than in the far field melt, resulting in a locally higher supersaturation and higher growth rates over those short distances. This could explain the high growth rates measured (1) during cooling, despite low undercoolings, and (2) when the crystals approached the border of the melt inclusion. The growth of olivine was probably not limited by its access to SiO<sub>2</sub> since it is a major component for both olivine and plagioclase and it is also the main constituent of the melt (~49 wt%; Clocchiatti and Massare, 1985; Jambon et al., 1992, *Appendix A5*). There is also no competition with other phases since the other two major components of olivine, MgO and FeO, are incompatible with the feldspar structure. However, the crystallization of olivine was apparently enhanced in the Series [B] experiment at 38 °C of undercooling, as the olivine crystal showed asymmetrical growth, with the extremity [100]

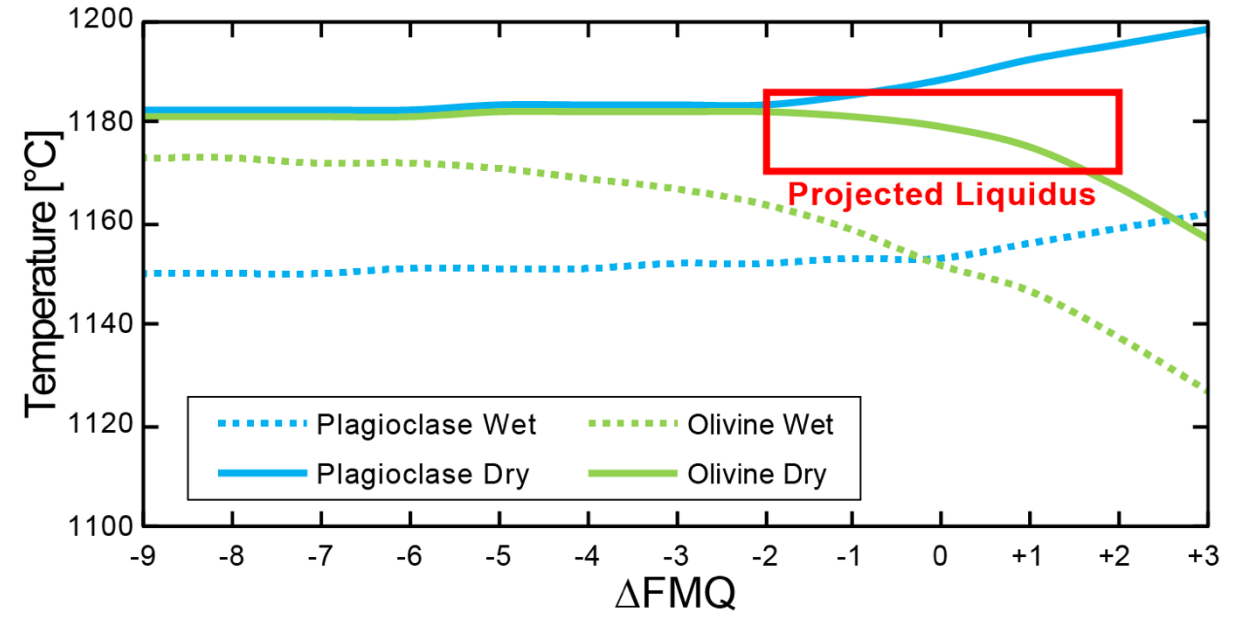
growing faster in the vicinity of the plagioclase wall (Fig. 2). In contrast with other experiments, these higher growth rates do not seem to be attributable to any optical or experimental artifacts, and may be a result of late crystal growth in a Mg-rich melt. Similarly, the Series [A] experiment at 96 °C of undercooling shows that the development of secondary branches happened earlier in proximity to the plagioclase walls (Fig. 2).

#### A5. Effect of diffusive relaxation

Here we assume that the initial chemical composition of the PC32 melt inclusion is similar to that measured in unheated, non-re-homogenized melt inclusions from the same host plagioclase crystal (Table A), with projected phase relationships as given in Figure A.

	SiO <sub>2</sub>	TiO <sub>2</sub>	Al <sub>2</sub> O <sub>3</sub>	FeOt	MnO	MgO	CaO	Na <sub>2</sub> O	K <sub>2</sub> O	P <sub>2</sub> O <sub>5</sub>	Cr <sub>2</sub> O <sub>3</sub>	NiO	H <sub>2</sub> O	CO <sub>2</sub>	CI	F	S	Total
	wt%	wt%	wt%	wt%	wt%	wt%	wt%	wt%	wt%	wt%	wt%	wt%	wt%	ppm	ppm	ppm	ppm	wt%
PL1	49.40	1.74	13.70	10.54	0.18	7.84	12.41	2.75	0.30	0.15	b.d.	b.d.	0.54	749	116	358	1161	99.8
1σ	0.23	0.04	0.07	0.17	0.02	0.04	0.08	0.10	0.02	0.03	_	_	0.01	21	4	5	16	
d.l.	0.03	0.07	0.02	0.12	0.12	0.05	0.04	0.07	0.03	0.03	0.04	0.19	0.01	43	0.7	1.9	0.7	

<u>Table A:</u> Representative chemical composition of 1978 Ardoukoba plagioclase-hosted melt inclusions as determined from three unheated, non-re-homogenized melt inclusions PL1, PL4, and PL5. Microprobe spots analyses (n=9) were taken  $\geq 20 \mu m$  from the walls of the melt inclusions to avoid boundary layer effects. The composition of glasses in major, minor and trace elements was measured using the CAMECA SX-100 electron microprobe of Brown University with a 15 kV accelerating voltage, 10 nA beam current, and a defocused 20 µm beam with 30 s peak counting time and 15 s for the background for each element; Na was measured first using the time zero intercept method. Natural and synthetic standards used for the calibration included AGV2 andesite (Si), RUTL2 rutile (Ti), BIR-1 basalt (Ca, Al), FAYA fayalite (Fe), RHOD rodonite (Mn), Fo97B forsterite (Mg), AM ALB2 albite (Na), OR-1 orthoclase (K), BERL berlinite (P), MgCr<sub>2</sub>O<sub>4</sub> spinel (Cr), and nickel metal (Ni). Analytical uncertainties (1  $\sigma$ ) were calculated using spot analyses of BCR-2G standard as unknowns. Volatiles (H<sub>2</sub>O, CO<sub>2</sub>, S, F and Cl) were measured (n=4) with the CAMECA 1280 ion mass spectrometer of WHOI (Woods Hole Oceanographic Institution – NENIMF, MA, USA) on Au-coated samples using a 20 µm raster size Cs<sup>+</sup> primary beam of 1 nA intensity and 10 or 12.5 kV acceleration voltage, with secondary ions accelerated at 10 kV. Standards for measurements of backgrounds included MORB glass 579/4/1 and suprasil SiO2 glass. Note that our measurements of major, minor and trace elements overlap with those reported in Clocchiatti and Massare (1985), and our S and Cl contents match within the uncertainty the values reported in Métrich and Clocchiatti (1996).



<u>Figure A:</u> Liquidus temperature of plagioclase and olivine in 1978 Ardoukoba melt inclusions simulated with the rhyolite-MELTS 1.2.0 software (Duan and Zhang, 2006; Ghiorso and Gualda, 2015; Ghiorso and Sack, 1995;

Gualda et al., 2012) for the constrained crystallization of Ol+Pl using starting composition PL1 ("wet" in dashed lines as PL1 given in Table A, and "dry" in solid lines as PL1 but completely deprived of H, C, S, F and Cl) for an isobaric cooling at 1 atm from 1300 to 1000 °C with a 1 °C increment at oxygen fugacity ranging from FMQ-9 to FMQ+3.

Significant chemical variations can occur inside melt inclusions while they are maintained at high temperatures over a protracted period of time (Bucholz et al., 2013; Chen et al., 2011; Danyushevsky et al., 2002; Gaetani et al., 2012; Kornprobst et al., 1979; Portnyagin et al., 2008; Roedder, 1979; Sobolev et al., 1983). For instance, plagioclase-hosted melt inclusions can lose most of their hydrogen through diffusive relaxation on the scale of 30 min to 4 days (Drignon et al., 2019). Based on these observations and the low water of Ardoukoba 1978 eruption melt inclusions (Table A), and given that our sample was maintained at high temperature for over 48 h prior to this set of experiments, it is likely that our melt inclusion also lost all of its hydrogen. But because the same sample was used for all of the experiments, the conditions were nearly identical from one run to another and hence ideal for the comparison of growth rates at various undercoolings. We emphasize however that this loss of hydrogen also implies that the residual melt was oxidized beyond FMQ-2 at the time of our experiments (Fig. A). Additionally, this might have led to a lower liquidus temperature for olivine in the melt. Note that our results are still directly comparable to those given in Jambon et al. (1992) since their samples were also held at high temperature overnight prior to cooling and crystallization of olivine.

#### A6. Effect of the thermal gradient

One possibility is that the elongation of crystals in the direction < 100 > or < 101 > (Fig. 2) results from constrained growth along a thermal gradient in the melt (Faure et al., 2006). Our measurements suggest that the temperature difference from one wall of the melt inclusion to its opposite is 0.3 - 0.5 °C in the horizontal plane, and 5 °C in the vertical axis (§ Experimental Methods). This indicates that the thermal gradient is actually weaker in the horizontal plane, i.e. where most of the crystals show the longest dimensions (Fig. 2, - $\Delta$ T = 19, 38, 57, 77 and 96 °C). Hence, the thermal gradient cannot be the cause of the elongation of crystals in that plane. Our crystals have habits and aspect ratios consistent with those formed in melts devoid of significant thermal and compositional gradients (Donaldson, 1976; Faure et al., 2003a). This also suggests that, in these experiments, the thermal gradient is neither responsible for the difference in velocities between the directions < 100 > and < 001 > in tabular olivine, nor for the difference in velocities between the directions < 101 > and < 001 > in skeletal and dendritic olivine.

#### APPENDIX B: REVIEW OF PREVIOUS DATASETS

The following sections cover many of the existing studies that publish estimates of olivine growth rates. The first sentence(s) of each section states the growth rates obtained and methods used in the given study. After follows an analysis and in many cases an effort to adjust the reported growth rates to more accurate values, based on methodological difficulties or general growth rate considerations. These calculations are provided in *Supplementary Material B*, and the adjusted growth rate values are plotted as part of Figure 11. In general, we approximated the maximum growth velocity achieved in each of these studies by measuring the single biggest crystal available in the data / images within a given population of crystals (e.g. macrocrysts, mesocrysts, or microcrysts; Welsch et al., 2009; Zellmer, 2021). Measuring the largest crystals is here necessary when calculating growth rates from total durations because they presumably result from an early nucleation and/or late physicochemical impediments.

**B1.** Donaldson (1975) estimated olivine growth rates in the range of  $2.2 - 6 \times 10^{-9}$  m/s by modeling the concentration and the diffusion of compatible elements in the boundary layer of large skeletal crystals in a basaltic melt at 1170 °C. Being the first ones published, these growth rates appear to have guided the interpretations in several following studies. However, these estimations are subject to several limitations. First, the author emphasized that the boundary layers are not a product of the primary growth of skeletal phenocrysts, but of overgrowths developed during the quench. This is supported by the fact that these phenocrysts have a matured morphology (closed hopper or matured dendrites) that suggests that they have lost their initial boundary layers (Colin et al., 2012; Faure and Schiano, 2004; Welsch et al., 2009, 2013). The final cooling event is marked with the development of dendritic overgrowths on the smaller olivine grains (top crystal in their figure 1b). One consequence for these observations is that the inferred growth rates are not related to primary skeletal growth or to an undercooling of 10 – 30 °C, but to undercoolings that extended beyond that range all the way up to the undercooling value of the glass transition. The true growth rates should have varied as a function of both the cooling rate and the rapidly-changing undercooling. Second, the accuracy of calculated growth rates depends both on the accuracy of the magma temperature at the time of the olivine overgrowths, and on the accuracy of the diffusion rate of elements in the melt at said temperature. Given the extent of cooling, the temperature of crystallization should be lower than that used for the calculations, and possibly less than 1110 °C considering the dendritic shape of microlites ( $-\Delta T > 60$  °C of undercooling in a simple system; Faure et al., 2003a). The diffusion rate should be also at a lower value, due to this lower temperature. Third, the estimations are based on concentration gradients in the melt  $(8-10 \mu m \text{ thick})$  perpendicular to unspecified flat interfaces, and those are most likely to be slow growing forms (typically {010}, {021} or {110} for a ripened skeletal unit of olivine, Welsch et al., 2013). Given that crystal growth is more extensive at the edges and vertices of crystals (Figs 1-3, and 5), the growth rates at these locations were faster. These estimates were extended to  $10^{-9} - 10^{-5}$  m/s in Donaldson (1979) based on additional experiments in Donaldson (1976). But because the available information on the crystal lengths and experiments durations is partial, it is not possible to reconstruct these growth rates properly.

**B2.** Kirkpatrick et al. (1981) estimated average growth rates for forsterite at  $10^{-7}$  to  $10^{-6}$  m/s by cooling a molten synthetic diopside glass at continuous cooling rates of 10 - 300 °C/h before quenching at apparent undercoolings of 140 - 239 °C. Their figures 2 and 3 suggest that the maximum lengths given in their table 2 are crystal diameters and not half-crystal lengths, which is pertinent to the calculation of growth rates (e.g. their figure 3a shows a crystal with a long radius of 1.4 mm while their table 2 reports a 2.8 mm crystal for experiment 57A at a cooling of 10 °C/h and a quench at 1201 °C). By halving the maximum lengths to account for

symmetrical growth, the data given in their table 2 allows us to calculate growth rates at  $6 \times 10^{-9}$  to  $2.6 \times 10^{-7}$  m/s (see *Supplementary Materials B2*). However, the authors specified that there was not enough information to calculate properly the growth rates, and that those values were only minimum averages (hence their higher estimations in the text). In fact, growth rates up to  $2.7 \times 10^{-6}$  m/s can be calculated if considering that olivine nucleation occurred between ~1300 and 1210 °C after ~3 to 147 min of cooling (their figure 1).

- **B3.** Fowler et al. (1989) estimated olivine growth rates at 3.4 x 10<sup>-9</sup> m/s through numerical modeling of dendritic growth by diffusion-limited aggregation to approach rapid olivine growth in komatiites. Further insight into these results is difficult given the unique approach. Nonetheless, the authors specified that their growth rates were necessarily a very low estimate given that they used very rough assumptions, and their results match those of Donaldson (1975), which are themselves low estimates of rapid olivine growth rates. In both cases, the necessary undercooling would be relatively high in order to produce dendritic, spinifex crystals (Donaldson, 1976; Faure et al., 2003a).
- **B4.** Armienti et al. (1991) also found a growth rate at 3 x 10<sup>-9</sup> m/s from the crystal size distribution (CSD) of Lanzarote basalt olivine at a projected undercooling of 30 °C. There are however several problems with these estimations. A first limitation is that the CSD was obtained from measurements of phenocrysts and microphenocrysts in thin sections, which suggests that a majority of those are underestimates of the true crystal dimensions. This issue is actually discussed in a later article by the first author (Armienti, 2008). A second issue concerns the relationship between the calculated growth rate and the inferred conditions of crystallization, which are not consistent with the results of Donaldson (1975, 1976). The values found in Armienti et al. (1991) are related to near-equilibrium crystallization at low growth rates (i.e. with no boundary layer), while the results of Donaldson (1975) correspond to low estimates for rapid crystal growth (i.e. with boundary layers).
- **B5.** See Discussion § Comparisons with a previous dataset, Figure 10, and Supplementary Material B5 for an analysis of Jambon et al. (1992)'s results.
- **B6.** Armienti et al. (1994) estimated a growth rate of 2.4 x  $10^{-11}$  m/s for crystals (Range A) at ~1 °C of undercooling in deep storage (their "range A" data), based on the olivine CSD of the 1991 1993 Mt. Etna hawaiites. This growth rate was estimated from the increase in grain size of phenocrysts over the course of the eruption (approximately +330 µm over the course of ~160 days) such that  $G = 330 \times 10^{-6}/(160 \times 24 \times 3600) = 2.4 \times 10^{-11}$  m/s. We note that the authors used the largest crystals in thin section as they presumably represent the crystals the least affected by cut effects (Armienti, 2008), hence with the highest possible mean growth rates. The increase in grain size appears constant for the biggest crystals, which supports the assumption of linear growth at depth. However, the results and their figure 8a indicate that crystal diameters were used instead of half-lengths, which suggests that symmetrical growth was not considered. Assuming symmetrical growth, the calculated growth rates should be at  $1.2 \times 10^{-11}$  m/s, for unspecified {hkl} interfaces.
- **B7.** Nakamura (1995) estimated growth rates at  $1.6 \times 10^{-12} 1.6 \times 10^{-11}$  m/s for Yatsugatake andesite olivine through growth and diffusion modeling in the system Mg Fe Ni. The authors however emphasized that the calculations assumed equilibrium growth, which necessarily implies extremely small undercoolings (0.1 °C was assumed for the plot in Fig. 11).

**B8.** Park and Hanson (1999) observed an increase in the average radius of forsterite crystals from 3.5 to 14 µm in 10 days after submersion in a basaltic melt at the liquidus temperature. This would correspond to a total growth rate of 1.2 x  $10^{-11}$  m/s through Ostwald ripening (symmetrical growth already accounted for). Their figure 5 shows however that the radius increases rapidly between 180 min and 1.9 day before reaching a constant speed for 7.9 more days. Our reconstruction of this figure (see *Supplementary Materials B8*) indicates that this second period has a linear growth rate at ~4.2 x  $10^{-12}$  m/s (correlation coefficient  $R^2 = 0.95$ ). This rate may be more representative of the true values of crystal growth by Ostwald ripening, although crystal settling may be also a limiting factor in averaging this kinetics (Cabane et al., 2005).

**B9.** Cabane et al. (2005) also studied the crystal growth of forsterite crystals in a basaltic melt through Ostwald ripening at undercoolings approaching 0 °C, although limited by inherent furnace temperature fluctuations of  $\pm$  0.3 °C. Their observations point towards the slowest values of growth rates determined so far in the literature, in the range 4.8 x  $10^{-16} - 1.1$  x  $10^{-12}$  m/s considering symmetrical and linear growth.

**B10.** Zieg and Lofgren (2006) estimated growth rates at 6 x  $10^{-10}$  to 2 x  $10^{-9}$  m/s for polyhedral grains and 2 x  $10^{-8}$  m/s for skeletal crystals based on the olivine CSD of crystallization experiments at undercoolings of 30 to 369 °C for a cooling rate of 92 °C/h. The starting material is a synthetic glass analogous to a porphyritic chondrule (Lofgren, 1989), containing olivine seeds. Protracted crystallization of the samples led to overgrowths on the seeds and the formation of new skeletal crystals in the melt. Although the bulk starting material liquidus was determined at 1550 °C, the true undercooling should be calculated from 1545 °C since the assemblage re-equilibrated at this temperature before the cooling ramp. The authors observed polyhedral crystals in all their experimental charges, which suggest that the reported polyhedral crystal growth rates refer to the whole range of undercoolings. On the other hand, they only observed skeletal crystals at 62 °C of undercooling and beyond, which suggests that the higher, skeletal crystal growth rate at 2 x  $10^{-8}$  m/s is only applicable to those undercoolings. These authors mentioned however that crystal growth was necessarily limited due to crystal impingement (Hersum and Marsh, 2006) and that the estimated growth rates are apparent (and thus not equivalent to  $G_{true}$ ).

**B11.** Schiano et al. (2006) measured growth rates in the range of  $0.3 - 3.2 \times 10^{-9}$  m/s for the (001) interface through the migration of olivine-hosted melt inclusions within a thermal gradient of a heating stage microscope. The study shows evidence that the migration was constant, which eliminates uncertainties due to periods of slower or non-growth. Although these growth rates are still subject to some dimension foreshortening, the error on the growth rates is relatively small. The growth is observed at low undercoolings, which we calculate as  $-\Delta T = 0.45 - 3.35$  °C, corresponding to half the temperature difference between the cold and the hot ends of the melt inclusion ( $\Delta T = \theta L/2$  with L the melt inclusion length and  $\theta$  the thermal gradient).

**B12.** Faure et al. (2007) estimated growth rates of 6.1 x  $10^{-8} - 8.8 \times 10^{-7}$  m/s for the dendrite tips {101} at nominal undercoolings of 70 to 236 °C using the quenching furnace method in the system CaO-MgO-Al<sub>2</sub>O<sub>3</sub>-SiO<sub>2</sub>  $\pm$  Na<sub>2</sub>O. Growth rates are determined both for the overgrowths developed on polyhedral crystals and for the dendritic crystals formed spontaneously from the melt. However, the authors stressed that these growth rates correspond to low estimates as the measurements were performed in samples with a high crystal density, i.e. in an environment where individual crystal growth is prone to impediment. The undercoolings attached to those

growth rates correspond to the ones calculated for the second cooling ramp, and those undercoolings can be considered as slight overestimations of the true undercoolings given that the equilibrium between the polyhedral crystals and the melt has not been reached at the start of the second cooling ramp. The lower growth rates observed at low temperatures are the consequence of crystallization from a MgO-depleted melt, with large surfaces of olivine crystals available.

**B13.** Ni et al. (2014) measured growth rates in the range  $2 - 7 \times 10^{-9}$  m/s in the direction < 100 > for tephroitic, skeletal olivine at large nominal undercoolings (> 100 °C) and moderate cooling rate (100 °C/h) in a Fe-free, Mn-rich melt using a moissanite cell. These values may appear relatively low for skeletal growth at high undercoolings (up to 200 °C), which could be attributed to the particular chemical composition and possibly high viscosity of the melt. The growth rates were necessarily capped by the cooling rates as they could not reach their maximum potential at high undercoolings without competing first for nutrients and space with adjacent crystals. In their figure 3, the crystal A changed its habit from tabular to skeletal after 24.5 min of cooling, which is consistent with skeletal growth appearing at moderate degrees of undercooling ( $-\Delta T = 24.5 \times 100/60 = 41 \,^{\circ}C$ ; Donaldson, 1976; Faure et al., 2003a). It is important to note that the heterogeneous distribution of the temperature inherent to the design of the mossainite cell dictated the crystallization of olivine at the local level, with separate nucleation events, variations in the grain size and crystal shape, and intercrystalline variations in the growth rates. In their figure 3, the crystals B and C have the closed hopper habit with multiple melt inclusions due to growth cycles between skeletal and tabular growth as they were transported back and forth between cold zones and warm zones in the melt (Colin et al., 2012; Faure and Schiano, 2004; Welsch et al., 2009). Ultimately, the high nominal undercoolings did not lead to dendritic crystal growth because most of the momentum of crystallization was already absorbed through the large density of crystals.

**B14.** Sossi and O'Neill (2016) estimated growth rates in the range 9 x  $10^{-9} - 2.9$  x  $10^{-6}$  m/s through crystallization experiments on a komatiitic melt hang on Re loops at cooling rates of 0.5 - 16 °C/min (30 – 960 °C/h) and undercoolings of 0.5 - 100 °C, after superheating for 1 – 19 h at 50 °C above the liquidus temperature. The measurements were performed on quenched crystals observed in polished sections. The crystal dimensions are reported for the c-axis in their table 5, but it is unclear how the dimension  $L^{\{001\}}$  of the dendritic crystals was measured based on their figure 4d, since dendritic olivine grows essentially in the dimension  $L^{\{101\}}$ . The authors give an uncertainty of  $\pm$  50  $\mu$ m, but it is not specified how this uncertainty was determined. Due to truncations and misalignments with the plane of observation, it is likely that the longest crystal dimensions are here underestimated (see Discussion § Effect of the crystal orientation). We note that the size of crystals shown in their figure 4a and 4c is inconsistent with their measurements as given in their table 5. For this paper, we assume that the scale is erroneous in their figure 4a and 4c and that the measurements are correct in their table 5. However, by comparing the size of other crystals shown in their figure 4 with the measurements given in their table 5, it appears that symmetrical growth was not considered. We suggest that the growth rates should be divided by two for the crystals that formed spontaneously from the melt and develop a full symmetrical shape, but not for some of the dendritic crystals that grew up against the walls (e.g. their figure 4d). Another concern is the uncertainty on the timing of crystal growth. From their data (their figure 3a), it is possible to project undercoolings of nucleation at 14.5 – 47.3 °C for melt fractions approaching ~100 % vol., and calculate incubation periods at 3-29 min using the cooling rate and the estimated liquidus temperature. However, these reconstructions suggest that their growth rates calculations considered the total time spent under the liquidus, including the incubation period (Fig. 7). Assuming linear growth, their growth rates could be corrected for the related incubation period and symmetrical growth at  $5.7 \times 10^{-8} - 4.3 \times 10^{-5}$  m/s (see *Supplementary Material B14*). We emphasize however that, in spite of these adjustments, the two highest values at  $6.9 \times 10^{-6}$  and  $4.3 \times 10^{-5}$  m/s remain problematic given that they correspond to the experiments with the second fastest cooling rate  $(6.5 \, ^{\circ}\text{C/min})$  and no textural information was provided for them. One possibility for these extreme values could be another problem with the scale and magnification of crystals since this seems to be the case in their figure 4a and 4c. If so, these values would represent overestimations of the true maximum growth rates.

**B15.** Bouvet de Maisonneuve et al. (2016) estimated growth rates in the range 7 x 10<sup>-8</sup> – 7 x 10<sup>-7</sup> m/s by modeling the kinetic disequilibrium partitioning of phosphorus between basaltic andesite olivine from Volcán Llaima and its melt with the equations of excessive incorporation after Albarède and Bottinga (1972). It is however important to note that these values of growth rates are only valid within the uncertainty on the different parameters used for the modeling, including the concentration and diffusivity of phosphorus in olivine and in the melt. Such modeling does not constraint the undercooling, but compared with our results and Jambon et al. (1992)'s and the textures associated with strong P incorporation in olivine (Faure et al., 2003a; Welsch et al., 2013), it is possible that their growth rates could apply to undercoolings in the range 20 – 150 °C.

**B16.** Mourey and Shea (2019) estimated growth rates in the range of 8 x 10<sup>-8</sup> to 1.2 x 10<sup>-7</sup> m/s for olivine phenocrysts grown in bulk from a Mg-rich basalt at OFM-1, undercoolings of 10. 25, 40 and 60 °C, and fast cooling rates (240 °C/h) using time constrained 3D scans of X-ray microtomography. They also estimated growth rates from (2D) thin sections and the composition of the residual glasses by mass-balance calculations. Raw data are given in their supplementary materials, for the chemical compositions of the residual melt, and for the 3D measurements of crystals formed at 40 and 60 °C of undercooling. Each sample began with a single large seed, but growth rates were not provided for the overgrowths formed onto them. Graphic reading of their figure 6 indicates maximum 2D-values at ~2 x 10<sup>-10</sup> m/s for 10 °C of undercooling,  $\sim 5 \times 10^{-9}$  m/s for 25 °C,  $\sim 6 \times 10^{-8}$  m/s for 40 °C, and  $\sim 1.2 \times 10^{-7}$  m/s for 60 °C. The growth rates estimated with the mass-balance calculations are at  $\sim 1.8 \times 10^{-9}$  m/s for 10 °C of undercooling,  $\sim 4.5 \times 10^{-8}$  m/s for 25 °C,  $\sim 8.5 \times 10^{-8}$  m/s for 40 °C, and  $\sim 5.0 \times 10^{-7}$  m/s for 60 °C. These growth rate calculations use the entire time spent under the liquidus, including any incubation period or other periods of slower or non-growth. The calculations also consider the entire lengths of crystals and not their half-lengths, so rates are for the growth of two interfaces instead of one. Using entire crystal lengths may be however correct for some of the individuals that grew as half-crystals such as the smaller ones that nucleated against the walls of the sample (e.g. top crystal in their figure 4E). Unencumbered crystals should have their growth rates divided by two, to account for symmetrical growth. Finally, the growth rates were determined for the three primary crystallographic axes of olivine, although they do not necessarily correspond to primary growth directions (Fig. 1). In fact, the directions < 100 >, < 010 >, and < 001 > can correspond to re-entrant forms that result from a lack of growth. Moreover, the dimensions  $L^{\{101\}}$  formed by the protrusions  $\{101\}$  can be significantly longer than the dimensions  $L^{\{100\}}$  and  $L^{\{001\}}$  (up to 33 % in their crystals by calculating the dimensions  $L^{\{101\}}$  as a-c diagonals using Pythagorean theorem and assuming no branch curvatures; but readjusted to -33 to -50 % once symmetrical growth is considered; see Supplementary Materials B16). The underestimation of growth dimensions seems more pronounced for the dendritic crystals since the measurements were applied to single crystal units rather than the entire parallel groups, whereas the primary branches {101} extend throughout the parallel units and connect the units together (Welsch et al., 2013; 2014). This may explain in part why their dendritic growth at  $-\Delta T = 60$  °C appears slower than their skeletal growth at  $-\Delta T = 40$ °C using the 3D scans (6.2 x 10<sup>-8</sup> m/s or less versus 1.2 x 10<sup>-7</sup> m/s or less, respectively). Their 2D-values do not seem to have this issue to the same extent, possibly because the measurements included several parallel units that appeared continuous in thin section. Their figure 4 also shows measurements of randomly oriented crystals in 3D, which suggests that misalignment with the projection plane were not accounted for. Depending on whether depth dimensions were integrated by the software for these measurements, this might have led to additional underestimations in the growth rates (Discussion § Effect of the crystal orientation). All their growth rates can be adjusted, at least partially, if the incubation period, symmetrical growth, and true directions of primary crystal growth are considered altogether. Based on the available data, we use an incubation period of 6 to 60 min (Donaldson, 1979) for the experiments at 10 and 25 °C of undercooling, and 6 – 19 min for the experiments at 40 and 60 °C of undercooling. We used here the shortest run durations (at 24h, 3h, 90 min, and 90 min, respectively) and the longest crystal dimension for each experiment to limit deviations from linear growth due to bulk crystallization and crystal settling. These approximate corrections of 2D-data indicate that the interfaces {10l} may have grown as rapidly as  $\sim$ 1 x 10<sup>-9</sup> m/s for 10 °C of undercooling, and  $2.6-3.7 \times 10^{-9}$  m/s for 25 °C (see Supplementary Materials B16). The vertices {101} of skeletal crystals at 40 °C of undercooling would have formed at  $3.2 - 3.4 \times 10^{-8}$  m/s according to the 2D data, and at  $6.7 - 7.9 \times 10^{-8}$  m/s with the 3D-data. The dendritic crystals formed at  $60 \,^{\circ}$ C of undercooling indicates low growth rates at  $6.4 - 7.6 \times 10^{-8}$  m/s with the 2D-data, or  $3.6 - 4.3 \times 10^{-8}$  m/s with the 2D-data, or  $3.6 - 4.3 \times 10^{-8}$ 10<sup>-8</sup> m/s with the 3D data. As a result, the adjusted growth rates would be lower than previously estimated. However, it is likely that the deceleration stage had already begun at the shortest run times for which crystal measurements were made available, meaning the rates include this period of slower growth; the true maximum growth rate would thus be higher than our adjusted estimate. The growth rates determined by mass-balance calculations appear to be one order of magnitude above the values of the 2D- and 3D-growth rates for the fast interfaces. This is unusual given that such approach usually finds growth rates that are lower than those obtained with crystal measurements (Jambon et al., 1992; Lang et al., 2021). This may indicate either that the 2D/3D estimations are significantly lower than the true maximum growth rates (due to averaging the period of linear maximum growth with periods of slower or non-growth), or that the MgO content of the starting melt was lower than predicted (due to analytical problems and/or dissolution/recrystallization over the seed pre-cooling). Their calculations also consider that the volume is constant, although there should be a reduction from liquid to solid due to the density difference between olivine and the parental melt. Using a reasonable olivine density of 3.3 x 10<sup>3</sup> kg/m<sup>3</sup> and a melt density of 2.85 x 10<sup>3</sup> kg/m<sup>3</sup>, a better estimation of the volume of olivine would be  $\sim 14$  % smaller than what is reported, and the projected isotropic growth rate would be  $\sim$ 5 % slower.

**B17.** Laumonier et al. (2019) estimated rates in the ranges of  $0.5 - 1.2 \times 10^{-9}$  m/s for cellular growth and  $0.2 - 5.3 \times 10^{-9}$  m/s for polyhedral growth through dissolution and recrystallization of olivine cylinders in a thermally zoned melt of basaltic composition. The calculated undercoolings are in the range 3.3 - 13.4 °C using  $\Delta T = \theta L/2$  with L being the third of the length of the charge ( $\sim 1 - 1.7$  mm), based on experiment geometry. The calculated growth rates consider the unilateral migration of the olivine interfaces in a thermal gradient (thickness of overgrowths) and the symmetrical growth of newly formed crystals in the melt (radius for the ones shown in their figures 3b and 6c - d). Based on the data provided in their table 3 and table 4, our recalculations match their ranges of growth rates (see *Supplementary Material B17*), expect for their high value reported at  $5.3 \times 10^{-9}$  m/s in their table 4 for a newly formed crystal in their experiment B7. We found instead a value of  $3.3 \times 10^{-10}$  m/s. This must be an erratum in

their table 4 given that both the text and their figure 10 give a more consistent range of growth rates at  $2.1 - 7.2 \times 10^{-10}$  m/s for the newly formed crystals.

**B18.** Salas et al. (2021) estimated rates in the range  $5 - 7 \times 10^{-8}$  m/s based on Ni and Mg-Fe diffusion modeling in Los Hornitos olivine using the growth entrapment model of Watson and Müller (2009). This approach has the same limitations than the one developed in Bouvet de Maisonneuve et al. (2016), plus uncertainty on the true width of the areas depleted in NiO. By their nature, measurements of natural samples cannot include a known undercooling at which these growth rates would occur, but compared with our own measurements, those given in Jambon et al. (1992), and the associated skeletal textures (Faure et al., 2003a; Welsch et al., 2013), these rates could be consistent with the advance speed of the fastest interfaces of skeletal crystals during maximum, linear growth at 20 - 60 °C of undercooling.

**B19.** Lang et al. (2021) estimated maximum growth rates in the range  $1.4 \times 10^{-9} - 4.7 \times 10^{-8}$ m/s from thin sections (2D) and 6.2 x  $10^{-10} - 3.5$  x  $10^{-8}$  m/s with mass-balance calculations using the same starting material as Mourey and Shea (2019) at cooling rates of 4, 20 and 60 °C/h and undercoolings of 35 and 85 °C. However, their starting material is enriched in FeO to compensate loss to the Pt wire, no olivine seed was added, the oxygen buffer was set at a more reducing level (QFM-2), and the whole system was superheated at  $+\Delta T = 40$  °C for an hour prior to cooling. Comparatively, their growth rates appear significantly lower, although with a smaller dispersion between the 2D estimations and the mass-balance calculations. The crystal dimensions that were measured are not specified, and we found several issues with the calculations of growth rates. The crystal dimensions given in the text do not clearly correspond to what can be measured in their figure 2; for example, a "maximum crystal length" of  $\leq 5 \mu m$ is inconsistent with the  $\sim$ 28  $\mu$ m crystal in the experiment at a cooling rate of 60 °C/h and 35 °C of undercooling (see Supplementary Materials B17). Crystal lengths given are full crystal lengths. Symmetrical growth was impeded in some cases, such as the experiment at a cooling rate of 60 °C/h and 85 °C of undercooling in which the dendritic crystal is asymmetric due to its growth against the wall of the sample. Overall, this suggests that their calculations did not use the longest dimensions and fastest directions of growth (such as  $L^{\{101\}}$ ), implying that their growth rates are most comparable to values at slower interfaces. This is consistent with the equation apparently used to calculate 2D growth rates (their table 1). In the figure footnotes of their table 1, the equations referenced for 2D and mass balance growth rate calculations, respectively, are swapped (i.e., footnote (2) should be (3) and vice versa). Moreover, the mass balance equation is erroneously listed in both cases, although the main text plus explanation of equation variables makes us confident that the equation used to calculate 2D growth rates is the one given in Hammer and Rutherford (2002):  $Y = (LW)^{0.5}/(2t)$  with Y the growth rate, L the crystal length, W the crystal width, and t the experiment duration. The crystal length and width measurements used are not reported, but using available numbers from the main text and visual estimates from their figure 2, along with growth rates in their table 1, this equation returns approximately the correct subliquidus experimental durations. The growth rate equation used does account for symmetrical growth. However, as pointed out by Hammer and Rutherford (2002), this equation comes with the caveat that it represents a time-averaged value that includes the duration of any nucleation lag. In addition, the use of crystal length and width is another type of averaging, which indicates that the reported 2D growth rates cannot be ascribed to a particular crystallographic face (hkl) or direction [uvw]. Finally, although their table 1 specifies time  $t_{exp}$  as "experimental duration," we presume this implies "subliquidus experimental duration." If we adjust the 2D growth rates by using only the longest dimension of the largest crystal for each experiment shown in their figure 2, and by subtracting an estimated incubation period of 6 min (Donaldson, 1979) for the experiments at a cooling rate of 60 °C/h and 60 min for the experiments at a cooling rate of 4 or 20 °C/h, we obtain new estimates of 2 x 10<sup>-9</sup> – 1.1 x 10<sup>-7</sup> m/s (*Supplementary Materials B17*). These adjusted values are still mean values (i.e. not maximum growth rates, Discussion § *Effect of a period of slower or non-growth*, Fig. 8). The growth rates estimated from mass-balance calculations have the same limits as in previous studies: it is an indirect estimation, and it is hence difficult to assess to what directions of growth they can be compared to and how close they are to the true maximum growth velocities. And because the authors used the same equations as Mourey and Shea (2019), the mass-balance-derived growth rates represent a slight overestimation, given that volume reduction during crystallization was not considered.

#### **REFERENCES**

- Albarède, F., and Bottinga, Y. (1972) Kinetic disequilibrium in trace element partitioning between phenocrysts and host lava. Geochimica et Cosmochimica Acta, 36, 141–156.
- Armienti, P. (2008) Decryption of igneous rock textures: Crystal size distribution tools. Reviews in Mineralogy and Geochemistry, 69(1), 623–649.
- Armienti, P., Innocenti, F., Pareschi, M.T., Pompilio, M., and Rocchi, S. (1991) Crystal population density in not stationary volcanic systems: Estimate of olivine growth rate in basalts of Lanzarote (Canary Islands). Mineralogy and Petrology, 44(3–4), 181–196.
- Armienti, P., Pareschi, M.T., Innocenti, F., and Pompilio, M. (1994) Effects of magma storage and ascent on the kinetics of crystal growth. Contributions to Mineralogy and Petrology, 115(4), 402–414.
- Bouvet de Maisonneuve, C., Costa, F., Huber, C., Vonlanthen, P., Bachmann, O., and Dungan, M.A. (2016) How do olivines record magmatic events? Insights from major and trace element zoning. Contributions to Mineralogy and Petrology, 171(6), 1–20.
- Bucholz, C.E., Gaetani, G.A., Behn, M.D., and Shimizu, N. (2013) Post-entrapment modification of volatiles and oxygen fugacity in olivine-hosted melt inclusions. Earth and Planetary Science Letters, 374, 145–155.
- Cabane, H., Laporte, D., and Provost, A. (2005) An experimental study of Ostwald ripening of olivine and plagioclase in silicate melts: implications for the growth and size of crystals in magmas. Contributions to Mineralogy and Petrology, 150(1), 37–53.
- Chen, Y., Provost, A., Schiano, P., and Cluzel, N. (2011) The rate of water loss from olivine-hosted melt inclusions. Contributions to Mineralogy and Petrology, 162(3), 625–636.
- Clocchiatti, R., and Massare, D. (1985) Experimental crystal growth in glass inclusions: The possibilities and limits of the method. Contributions to Mineralogy and Petrology, 89(2–3), 193–204.
- Colin, A., Faure, F., and Burnard, P. (2012) Timescales of convection in magma chambers below the Mid-Atlantic ridge from melt inclusions investigations. Contributions to Mineralogy and Petrology, 164(4), 677–691.
- Danyushevsky, L.V., McNeill, A.W., and Sobolev, A.V. (2002) Experimental and petrological studies of melt inclusions in phenocrysts from mantle-derived magmas: An overview of techniques, advantages and complications. Chemical Geology, 183(1), 5–24.
- Donaldson, C.H. (1975) Calculated diffusion coefficients and the growth rate of olivine in a basalt magma. Lithos, 8(2), 163–174.
- Donaldson, C.H. (1976) An experimental investigation of olivine morphology. Contributions to Mineralogy and Petrology, 57(2), 187–213.
- Donaldson, C.H. (1979) An experimental investigation of the delay in nucleation of olivine in mafic magmas. Contributions to Mineralogy and Petrology, 69(1), 21–32.
- Drignon, M.J., Nielsen, R.L., Tepley Iii, F.J., and Bodnar, R.J. (2019) Reequilibration processes occurring in plagioclase-hosted melt Inclusions from plagioclase ultraphyric basalts. Geochemistry, Geophysics, Geosystems, 20(1), 109–119.
- Duan, Z., and Zhang, Z. (2006) Equation of state of the H2O, CO2, and H2O–CO2 systems up to 10 GPa and 2573.15K: Molecular dynamics simulations with ab initio potential surface. Geochimica et Cosmochimica Acta, 70(9), 2311–2324.
- Faure, F. (2020) Early silica crust formation in planetesimals by metastable silica-rich liquid immiscibility or cristobalite crystallisation: the possible origin of silica-rich chondrules. Scientific Reports, 10(1), 4765.
- Faure, F., Arndt, N., and Libourel, G. (2006) Formation of spinifex texture in komatiites: An experimental study. Journal of Petrology, 47(8), 1591–1610.
- Faure, F., and Schiano, P. (2004) Crystal morphologies in pillow basalts: Implications for midocean ridge processes. Earth and Planetary Science Letters, 220(3-4), 331–344.

- Faure, F., Schiano, P., Trolliard, G., Nicollet, C., and Soulestin, B. (2007) Textural evolution of polyhedral olivine experiencing rapid cooling rates. Contributions to Mineralogy and Petrology, 153(4), 405–416.
- Faure, F., and Tissandier, L. (2014) Contrasted liquid lines of descent revealed by olivine-hosted melt inclusions and the external magma. Journal of Petrology, 55(9), 1779–1798.
- Faure, F., Trolliard, G., Nicollet, C., and Montel, J.-M. (2003a) A developmental model of olivine morphology as a function of the cooling rate and the degree of undercooling. Contributions to Mineralogy and Petrology, 145(2), 251–263.
- First, E.C., Leonhardi, T.C., and Hammer, J.E. (2020) Effects of superheating magnitude on olivine growth. Contributions to Mineralogy and Petrology, 175(2), 13.
- Fowler, A.D., Stanley, H.E., and Daccord, G. (1989) Disequilibrium silicate mineral textures: Fractal and non-fractal features. Nature, 341(6238), 134–138.
- Gaetani, G.A., O'Leary, J.A., Shimizu, N., Bucholz, C.E., and Newville, M. (2012) Rapid reequilibration of H<sub>2</sub>O and oxygen fugacity in olivine-hosted melt inclusions. Geology, 40(10), 915–918.
- Ghiorso, M.S., and Gualda, G.A.R. (2015) An H<sub>2</sub>O–CO<sub>2</sub> mixed fluid saturation model compatible with rhyolite-MELTS. Contributions to Mineralogy and Petrology, 53(169), 1–30.
- Ghiorso, M.S., and Sack, R.O. (1995) Chemical mass transfer in magmatic processes IV. A revised and internally consistent thermodynamic model for the interpolation and extrapolation of liquid-solid equilibria in magmatic systems at elevated temperatures and pressures. Contributions to Mineralogy and Petrology, 119(2), 197–212.
- Gualda, G.A.R., Ghiorso, M.S., Lemons, R.V., and Carley, T.L. (2012) Rhyolite-MELTS: a modified calibration of MELTS optimized for silica-rich, fluid-bearing magmatic systems. Journal of Petrology, 53(5), 875–890.
- Hammer, J.E., and Rutherford, M.J. (2002) An experimental study of the kinetics of decompression-induced crystallization in silicic melt. Journal of Geophysical Research, 107(B1), ECV 8-1-ECV 8-24.
- Hersum, T.G., and Marsh, B.D. (2006) Igneous microstructures from kinetic models of crystallization. Journal of Volcanology and Geothermal Research, 154(1), 34–47.
- Jambon, A., Lussiez, P., and Clocchiatti, R. (1992) Olivine growth rates in a tholeiitic basalt: An experimental study of melt inclusions in plagioclase. Chemical Geology, 96, 277–287.
- Kirkpatrick, R.J., Kuo, L.-C., and Melchior, J. (1981) Crystal growth in incongruently-melting compositions: Programmed cooling experiments with diopside. American Mineralogist, 60, 223–241.
- Kornprobst, J., Boivin, P., and Bachèlery, P. (1979) L'alimentation des éruptions récentes du Piton de la Fournaise (Ile de la Réunion, Océan Indien): Degré d'évolution et niveau de ségrégation des laves émises. Comptes rendus de l'Académie des Sciences, 288D(29), 1691–1694.
- Lang, S., Mollo, S., France, L., Misiti, V., and Nazzari, M. (2021) Kinetic partitioning of majorminor cations between olivine and Hawaiian tholeiitic basalt under variable undercooling and cooling rate conditions. Chemical Geology, 584, 120485.
- Laumonier, M., Laporte, D., Faure, F., Provost, A., Schiano, P., and Ito, K. (2019) An experimental study of dissolution and precipitation of forsterite in a thermal gradient: Implications for cellular growth of olivine phenocrysts in basalt and melt inclusion formation. Contributions to Mineralogy and Petrology, 174(11), 94.
- Lofgren, G. (1989) Dynamic cyrstallization of chondrule melts of porphyritic olivine composition: Textures experimental and natural. Geochimica et Cosmochimica Acta, 53(2), 461–470.

- Métrich, N., and Clocchiatti, R. (1996) Sulfur abundance and its speciation in oxidized alkaline melts. Geochimica et Cosmochimica Acta, 60(21), 4151–4160.
- Mourey, A.J., and Shea, T. (2019) Forming olivine phenocrysts in Basalt: A 3D characterization of growth rates in laboratory experiments. Frontiers in Earth Science, 7, 1–16.
- Nakamura, M. (1995) Residence time and crystallization history of nickeliferous olivine phenocrysts from the northern Yatsugatake volcanoes, Central Japan: Application of a growth and diffusion model in the system Mg-Fe-Ni. Journal of Volcanology and Geothermal Research, 66(1), 81–100.
- Ni, H., Keppler, H., Walte, N., Schiavi, F., Chen, Y., Masotta, M., and Li, Z. (2014) In situ observation of crystal growth in a basalt melt and the development of crystal size distribution in igneous rocks. Contributions to Mineralogy and Petrology, 167(5), 1–13.
- Nývlt, J. (1984) Nucleation and growth rate in mass crystallization. Progress in Crystal Growth and Characterization of Materials, 9(3), 335–370.
- Park, Y., and Hanson, B. (1999) Experimental investigation of Ostwald-ripening rates of forsterite in the haplobasaltic system. Journal of Volcanology and Geothermal Research, 90(1), 103–113.
- Portnyagin, M., Almeev, R., Matveev, S., and Holtz, F. (2008) Experimental evidence for rapid water exchange between melt inclusions in olivine and host magma. Earth and Planetary Science Letters, 272(3–4), 541–552.
- Roedder, E. (1979) Origin and significance of magmatic inclusions. Bulletin de Minéralogie, 102, 487–510.
- Salas, P., Ruprecht, P., Hernández, L., and Rabbia, O. (2021) Out-of-sequence skeletal growth causing oscillatory zoning in arc olivines. Nature Communications, 12(1), 4069.
- Schiano, P., Provost, A., Clocchiatti, R., and Faure, F. (2006) Transcrystalline melt migration and Earth's mantle. Science, 314(5801), 970–974.
- Sobolev, A., Clocchiatti, R., and Dhamelincourt, P. (1983) Les variations de la température, de la composition du magma et l'estimation de la pression partielle d'eau pendant la cristallisation de l'olivine dans les océanites du Piton de la Fournaise (Réunion, éruption de 1966). Comptes rendus de l'Académie des Sciences, II(296), 275–280.
- Sossi, P.A., and O'Neill, H.S.C. (2016) Liquidus temperatures of komatiites and the effect of cooling rate on element partitioning between olivine and komatiitic melt. Contributions to Mineralogy and Petrology, 171(5), 49.
- Watson, E.B., and Müller, T. (2009) Non-equilibrium isotopic and elemental fractionation during diffusion-controlled crystal growth under static and dynamic conditions. Chemical Geology, 267(3–4), 111–124.
- Welsch, B., Faure, F., Bachèlery, P., and Famin, V. (2009) Microcrysts record transient convection at Piton de la Fournaise volcano (La Reunion hotspot). Journal of Petrology, 50(12), 2287–2305.
- Welsch, B., Faure, F., Famin, V., Baronnet, A., and Bachèlery, P. (2013) Dendritic crystallization: A single process for all the textures of olivine in basalts? Journal of Petrology, 54(3), 539–574.
- Welsch, B., Hammer, J.E., and Hellebrand, E. (2014) Phosphorus reveals dendritic architecture of olivine. Geology, 42(10), 867–870.
- Zellmer, G.F. (2021) Gaining acuity on crystal terminology in volcanic rocks. Bulletin of Volcanology, 83(11), 78.
- Zieg, M.J., and Lofgren, G.E. (2006) An experimental investigation of texture evolution during continuous cooling. Journal of Volcanology and Geothermal Research, 154(1–2), 74–88.